UNIVERSITÀ
POLITECNICA
DELLE MARCHE

Università Politecnica delle Marche
Scuola di Dottorato di Ricerca in Scienze dell'Ingegneria
Corso di Dottorato in Ingegneria Industriale

3D Printed PEI Cellular Materials: Mechanics, Performances and Piezoresistive Properties

Ph.D. Candidate:
Mattia Utzeri

Supervisor:
Prof. Marco Sasso

Coadvisor:
Prof. Shanmugam Kumar

Ph.D. Course Coordinator:
Prof. Giovanni Di Nicola

Edition: XXXV - new series

UNIVERSITÀ
POLITECNICA
DELLE MARCHE

Università Politecnica delle Marche
Scuola di Dottorato di Ricerca in Scienze dell'Ingegneria
Corso di Dottorato in Ingegneria Industriale

3D Printed PEI Cellular Materials: Mechanics, Performances and Piezoresistive Properties

Ph.D. Candidate:
Mattia Utzeri

Supervisor:
Prof. Marco Sasso

Coadvisor:
Prof. Shanmugam Kumar

Ph.D. Course Coordinator:
Prof. Giovanni Di Nicola

Edition: XXXV - new series

Università Politecnica delle Marche
Scuola di Dottorato di Ricerca in Scienze dell'Ingegneria
Corso di Dottorato in Ingegneria Industriale
Via Brecce Bianche – 60131 Ancona (AN), Italy

A Miriam

A chi gli chiedeva perché lo avesse fatto, rispondeva semplicemente: "...ma lei, avendo la possibilità di fare qualcosa, cosa avrebbe fatto al mio posto?"

Giorgio Perlasca - "Giusto tra le nazioni"

Acknowledgments

Il dottorato si è dimostrato un percorso di tre anni della mia vita di estrema importanza, tortuso ma ricco di esperienze. Ho compreso che il dottorato non è mera ricera accademica ma la conclusione del percorso di formazione personale che l'istruzione italiana può fornire, il cui obiettivo è far sviluppare un pensiero critico e libero in ambito accademico e sociale.

Non posso che ringraziare la mia famiglia per avermi permesso di raggiungere questo ambizioso traguardo, e rimarcare, ancora una volta, quanto il ruolo della famiglia sia essenziale nelle scelte e negli stimoli per la persona. Un immenso "grazie" va a mio fratello Samuele, forse un pò lontano geograficamente ma sempre presente nella mia vita. Un ringraziamento speciale va alla persona mia più cara Miriam, la mia certezza. In questi anni ci siamo fatti forza l'un l'altro nelle nostre scelte, da Glasgow a Genova, Forlì, Roma, Bologna, Verona, Padova, trovando sempre il tempo per stare insieme. Le devo molto. Con lei il futuro non mi spaventa, *nec spe nec metu*.

La ricerca accademica non è mai stata la mia prerogativa prima del dottorato, però la mia passione per l'ingegneria meccanica e la mia curiosità sono state fortemente soddisfatte in questi tre anni, chiarendomi tutti i dubbi pregressi riguardo a cosa volessi fare nel mio futuro da neolaureato. Ringrazio il professor Sasso e il gruppo di costruzione di macchine dell'Università di Ancona perchè mi hanno permesso di approfondire gli studi di tutto ciò che avevo in mente con libertà e fiducia mettendomi a disposizione strumenti, conoscenze e tempo.

I would like to deeply express my gratitude to Professor Kumar. He hosted me in his laboratory in Glasgow without knowing me before. He gave me the opportunity to do research under his supervision. It was a pleasure and an honor spending time with him. My time in Glasgow grew me up from an academic point of view to an international one.

Negli anni si prende coscenza della società attuale, degli attori del passato e delle situazioni susseguite alle loro scelte. Necessariamente, ora più che mai, mi nasce un pensiero critico verso la società attuale. I problemi credo siano molteplici, dalla crisi dell'identità dell'individuo, all'antimoralismo fino alla banalizzazione dell'istruzione. Pertanto un ringraziamento particolare lo vorrei fare a persone del passato, che tramite le loro gesta, mi hanno confermato che si deve lottare per un ideale. Credo che Perlasca sia il primo da dover ricordare, anzi da non dimenticare mai. La sua storia mostra l'essenza di battersi per qualcosa che sia umanamente giusto. Risulta impossibile anche non elogiare il coraggio e la professionalità dei magistrati Falcone

e Borsellino. Passando ai politici Moro, Berlinguer e Craxi che sfidarono l'america in nome della sovranità italiana in Italia. Fino a personalità dello spettacolo come Benigni o Gaetano. Riporto solo esempi più o meno noti nella storia italiana, l'elenco è sicuramente più lungo.

Spero che le loro eredità, unite al mio pensiero e alle mie competenze mi diano la possibilità di continuare la carriera nel mondo accademico in questo paese di immensa belleza.

Ancona, Novembre, 2022

Mattia Utzeri

Abstract

The research activity aims to evaluate and simulate the mechanical and multi-physics properties of cellular materials made of polyetherimide enabled via additive manufacturing. A literature review on polyetherimide and its composites drives research on this polymer, demonstrating the undertaken study's relevance.

Firstly, cellular materials are introduced from functional designing to mechanics. Three relative densities of cellular materials with four different planar structures were designed and printed through fused filament fabrication technology. The cellular materials made of polyetherimide were tested under compression loading to investigate their mechanical performances and energy absorption peculiarities.

Secondly, the mechanics of glassy thermoplastic polymers are introduced to figure out the physics behind constitutive models of polymers. Finite element analyses are carried out to predict the mechanical response of 3D-printed polyetherimide cellular materials. In the beginning, the polymer properties are defined through a traditional characterization strategy. However, the numerical results turn out to be inconsistent with experimental findings. The constitutive model evolves introducing an inverse method to extrapolate the mechanical properties of additively manufactured polyetherimide. The updated constitutive model is based on physics and mechanics observations that suppose the printed polyetherimide has higher crazing sensitivity due to the additive manufacturing process. The numerical model evolves again introducing interlayer failure modes according to the deposition strategy into the previous model.

In the end, metamaterials are introduced. The piezoresistivity phenomenon is discussed from linear to nonlinear analytical theory. Finite element analysis based on thermal/electrical analogy is carried out to predict the electrics-mechanics properties. The electrical properties of four different planar unit cells are investigated. The planar structures exhibit anisotropic electrical properties and nonlinear piezoresistivity. The gauge factors turn out to be inconsistent with the analytical theory. The homogeneous conductor hypothesis fails, thus the homogenized electrical properties were defined introducing geometrical nonlinearities in the electrical resistivity matrix. The self-sensing properties of each unit-cells are discussed through numerical and theoretical observations.

Self-sensing CNT/PEI honeycombs with four different unit-cell were printed through fused filament fabrication technology. The cellular materials were tested under compression loading to investigate their mechanical performances and self-sensing properties. The nonlinear electrical resistivity of bulk CNT/PEI was determined and

then implemented into the constitutive model. The mechanical response along with the piezoresistive behaviour of CNT/PEI honeycombs under compression was simulated through the nonlinear piezoresistive numerical model.

Contents

List of Figures

List of Tables

Chapter 1

PEI Overview

1.1 Introduction

The research on ideal polyimide with high engineering performances led to the discovery of PEI in the 1970s by Soviet researchers[20]. PEI is an amber-to-transparent thermoplastic polymer. The majority of synthesised PEIs are amorphous and their glass transition temperature range from 200°C to 280°C. PEI became famous under the trade name Ultem™(General Electric Company or Sabic Innovative Plastics); the first developed material based on PEI. Ultem™is a glassy thermoplastic material constituted by regular repeat units of ether and imide linkages with the following chemical structure: The aromatic imide units provide high-performance properties

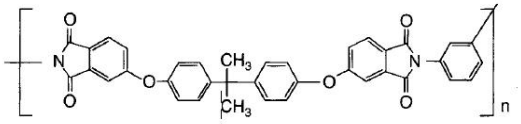

Figure 1.1: Ultem™chemical structure.

such as stiffness and high heat resistance while the flexible ether linkages allow for good melt flow characteristics and easy processability [21].

Ultem™is characterized by high mechanical strength, thermal properties, chemical resistance, dielectric properties, and resistance to thermo-oxidation processes.

However, Ultem™became famous for its flame retardant behaviour and low smoke emissions under combustion. Essentially, this polymer is a char former, with the char effectively retarding further flame propagation. The limiting oxygen index of 47 is the highest of any usually used engineering thermoplastics [22], flame retardancy, low toxicity, and low smoke emssion[21]. The great versatility of PEI is confirmed by annual production that ranges around $1.2x10^4$ t.

In addition, PEI is miscible with PET, PAI, PBT, and PEEK thus providing an attractive route for obtaining new polymeric materials with a desirable combination of engineering properties. These miscible properties enable PEI as a strong matrix for composite materials in which short fibres, long fibres, fillers, and nanotubes are dispersed[23, 24, 25, 26].

Additive Manufacturing (AM) has revolutionized the manufacturing world in the last decade. The additive manufacturing process enables overtaking the design limits of traditional technology. The free-shape design coupled with high-performance materials allows the achieving cutting-edge applications unthinkable before. The additive manufacturing process creates three-dimensional parts adding materials layer-by-layer according to a computer-aided design model. The polymers' peculiarities suites excellently all AM requirements needed. Indeed, the first 3D printers were focused on polymer production as figure1.2 illustrates. Therefore, polymer manufacturing has been strongly influenced by additive manufacturing[27].

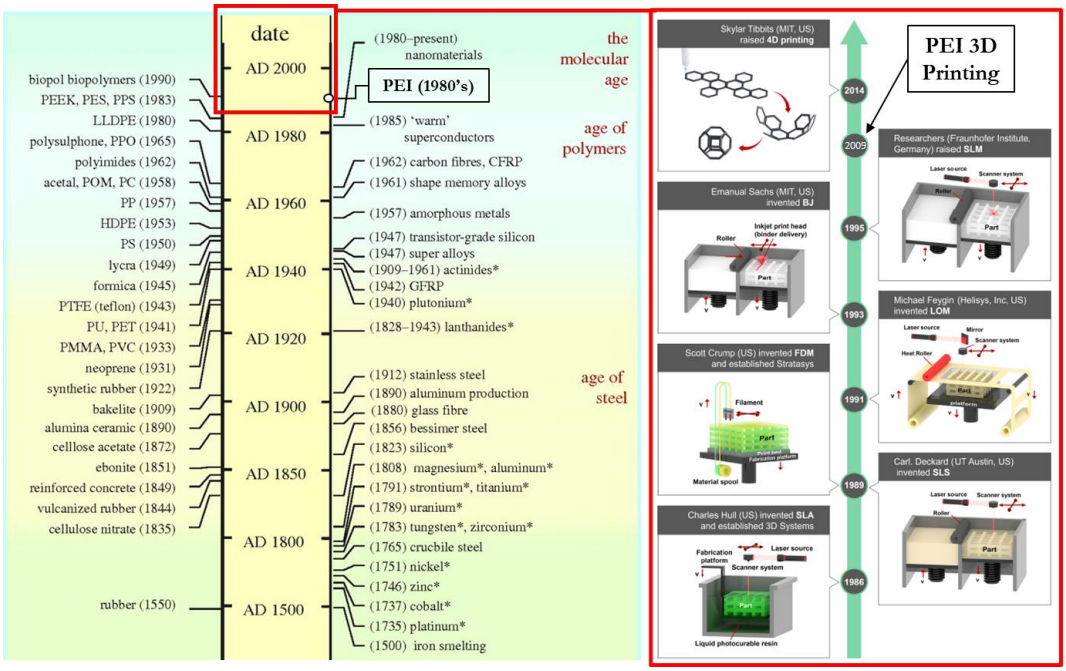

Figure 1.2: Additive manufacturing technology road map.

Ultem™'s excellent properties have allowed it to be a high-potential polymer in the AM world. Ultem™has demonstrated over time that its amorphous nature and its great adhesive properties allow achieving 3D-printed components with high thermal, structural, chemical, electrical and above all fireproof performance. It is interesting to introduce the PhD thesis by carrying out a brief historical overview of the academic and industrial activities carried out on 3D-printed Ultem™.

1.1.1 PEI in the Literature

A literature survey evaluated the published articles on the Scopus database. The trend of published articles on AM-enabled PEI is illustrated in figure1.3. Researchers have worked on PEI since the 1970s but the first articles on 3D-printed PEI were published in 2010. The first additive manufacturing technology which enables PEI 3D printing was Fused Filament Fabrication. Sabic IP produced the first PEI filament, commercially called Ultem 9085. Researchers have worked on PEI from 1970s

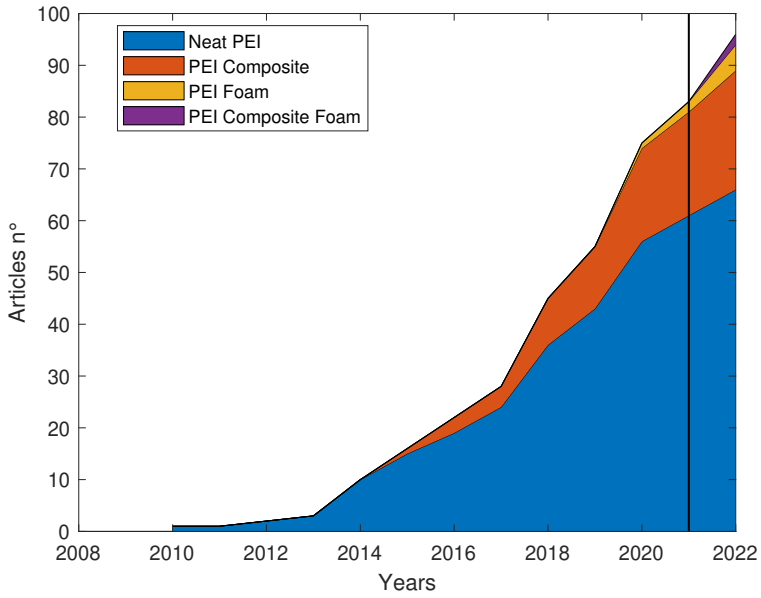

Figure 1.3: Trend of published articles on AM-enabled PEI.

but the first articles on 3D-printed PEI were published in 2010. The first additive manufacturing technology that enables PEI 3D printing was Fused Filament Fabrication. Sabic IP produced the first PEI filament, commercially called Ultem 9085.

From 2010 to 2016 the research activities were focused on FFF-Ultem mechanical properties under tensile and compression loading[28, 29, 30, 31]. The infill percentage and strategy deposition effects on mechanical performances were investigated. However, all these studies were driven by the industrial application of FFF parts such as orthosis, construction, tools, vessels and so on[32, 33, 34, 35]. In fact, these articles show only the potentiality of FFF parts made of Ultem at international conferences.

From 2017 length papers have been affirmed and mechanical properties are the key topics yet. In detail, the relationships between printing parameters and mechanical properties are deeply studied[36, 37, 38]. Anisotropy related to 3D printing and even uniaxial fatigue is discussed[39]. The aims remained the same: find the best printing parameter for high-strength parts in industrial applications.

This is also demonstrated by from the birth of the first research on residual stresses after printing. Thermal simulations were added to predict the heating and cooling rate during the filament deposition[40, 41]. As well as the applicability of coatings and surface treatments on FFF-printed parts[42]. In addition, dimensional accuracy studies on PEI printed parts were addressed[43].

In 2019 the first 3D-printed cellular materials have appeared. Auricchio investigates the linear elastic properties of tetrarchical and bi-tetrarchical honeycombs[44]. In 2022, Fores-Garriga evaluated how the topology of unit-cell influences Young's

modulus of PEI honeycombs. However, both of them evaluated only the linear elastic properties of PEI honeycombs through numerical, experimental, and analytical observations. The mechanics of FFF-Ultem was not addressed yet as well as the plasticity and energy absorption properties of PEI honeycombs.

In 2021 Cebeci introduced the first PEI composite filament. The neat PEI thermal and mechanical properties were enhanced and the CNT/PEI become conductive[25, 23]. Cebeci opens the metamaterial route at self-sensing PEI bulk and cellular materials. None PEI composite honeycombs are additively manufactured yet.

Relevant works were addressed by Zhai et al. in 2020. Zhai investigated the mechanical performances of hierarchical porous polyetherimide assisted by an in-situ CO_2 foaming technology [45, 46]. Zhai 3D-printed the first foamed filament shaping a honeycomb cellular material. He opened to a new idea of FFF-printing cellular materials.

Thanks to this brief historical introduction, the PhD thesis takes relevance. The PEI and PEI composite cellular materials are getting to spread so this study would put one of the first stones in PEI and PEI composite cellular materials history.

1.1.2 PEI in the World

In the literature survey, Ultem filament is not exalted or presented as an extraordinary material, it is studied like billions of other printable materials. The true value of the filament is hidden from the literature; looking for the filament or FFF printed parts made of Ultem in the industrial world the true potential is revealed.

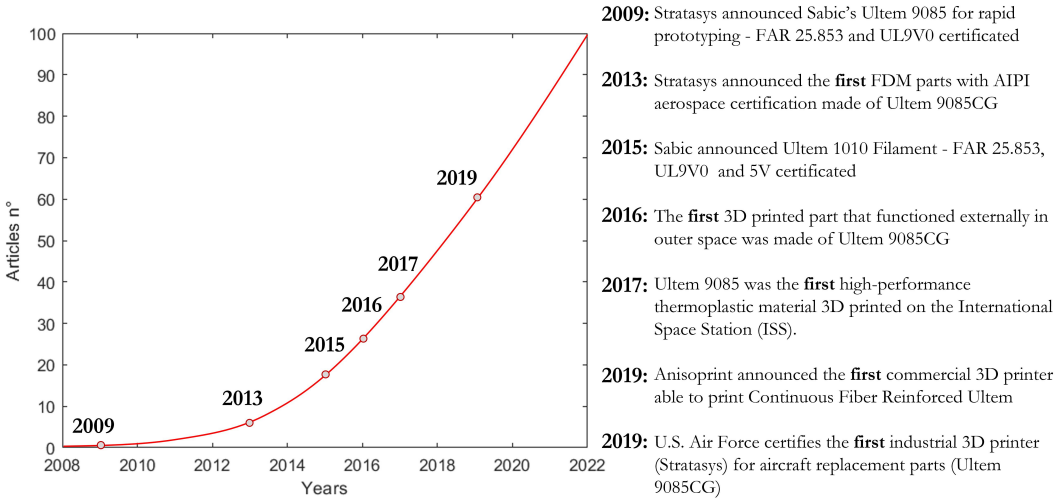

Figure 1.4: Milestones in the FFF-enabled PEI history

Figure1.4 illustrated the milestones reached by the Ultem™filament superposed on the trend of the published articles. The milestones shown in this figure are pointed out according to how the PhD candidate evaluates crucial in the history of additive manufacturing.

Stratasys was the first printer company to believe in Ultem™manufactured through Fused Deposition Modelling or FFF technology. Stratasys collaborated with Sabic IP to develop the high qualities FFF printed parts. It chose Ultem™as a key material because of its high thermal, mechanical, chemical and fireproof properties. Stratasys officially announced Sabic's Ultem™9085 for rapid prototyping in 2009. The printed parts achieved high fireproofing properties and also they can be certified FAR25.853 and UL9V0.

Stratasys kept investing in Ultem™9085. Stratasys understood the issues due to the additive manufacturing process. Especially Stratasys worked on quality, defects and inclusions on FFF Ultem™printed parts. It developed a strong connection with Sabics IP in order to have the best control on parts: from the production chain to additive manufacturing. Thanks to this accurate control of the entire manufacturing process, Stratasys announced the first aerospace certification of FFF parts in additive manufacturing FFF history in 2013. The AIPI aerospace certification was attributed to Ultem™9085CG.

Ultem 9085CG destroyed all records on FFF materials, additive manufacturing, and polymer histories. In 2016, FDM parts made of Ultem™9085CG were the first functional components in outer space. The high printability of Ultem™9085 gives to International Space Station (ISS) the chance to print the first polymer in outer space in the history of the polymer.

The last milestone was in 2019. U.S. Air Force certified the first industrial printer (Stratasys) for aircraft replacement parts made of FFF-Ultem™9085CG.

All these records increase the value of research on PEI and its blends.

1.2 Neat PEI Properties

In the FFF world, the Ultem performances can be achieved also by other filaments such as PPSU (Radel Solvay), PEEK (Victrex), and PEKK (Arkema). Therefore, the mechanical and thermal properties result interesting to compare.

Table 1.1: Mechanical properties of high-performance thermoplastic filaments

Filament material	Young's modulus [MPa]	Strength [MPa]	ε_{max} [%]	Notched Izod impact $[\frac{J}{m^2}]$	ν [-]
Ultem™ 1010 (Sabic)	2800	80	4	31	0.39
Ultem™ 9085 (Sabic)	2300	72	5	107	0.39
PPSU (Radel Solvay)	2000	62	21	480	0.43
PEEK (Victrex)	3250	110	25	214	0.37
PEKK (Arkema)	2850	92	8	45	0.41

The mechanical properties of these high-performance thermoplastic materials are listed in table1.1 and compared graphically in figure1.6. Ultem™as well as PEKK

show brittleness properties that result in low impact strength and failure strain. PEEK and PPSU exhibit high ductility. PEEK reveals to be the best filament and overtakes Ultem™far.

The thermal and physical properties of these high-performance thermoplastic materials are listed in table1.2. The high glass transition temperatures (T_g) show the excellent performances of these filaments. Ultem and PPSU are amorphous polymers with higher T_g than other semicrystalline polymers, i.e. PEEK and PEKK. However, the thermal resistance properties are measured also with $T_{10\%}$, i.e. temperature at which mass 10% is lost during the combustion. Indeed, in semicrystalline polymers, the $T_{10\%}$ is higher than others. That means PEKK and PEEK keep to withstand loading after the T_g even if they overtake the glassy phase.

Table 1.2: Physical properties of high-performance thermoplastic filaments

Filament material	Density $[\frac{g}{cc}]$	T_g [°C]	$T_{10\%}$ [°C]	HRC $[\frac{J}{gK}]$	Char yield [%]	T. conductivity $[\frac{W}{mK}]$
Ultem™ 1010 (Sabic)	1.27	216	550	233	52	0.24
Ultem™ 9085 (Sabic)	1.27	180	518	408	43	0.24
PPSU (Radel Solvay)	1.29	220	556	228	42	0.3
PEEK (Victrex)	1.32	143	612	435	50	0.29
PEKK (Arkema)	1.29	165	600	580	64	0.26

The fireproofing properties are measured by Heat Release Capacity (HRC) and char yield. HRC is related to the combustion material properties and it defines the energy to ignite the materials. The higher the HRC and higher is material flame resistance. Char yield means the remaining mass after completely degrading the substance including residual carbon. Although Ultem has the lowest mechanical properties it exhibits a high value of HRC and the lowest char yield value.

In the industrial world, the economy drives design so material pricing is crucial. Thus, the prices of all filaments needs to be compared. Tabled1.3 shows them.

Table 1.3: Cost of high-performance thermoplastic filaments.

Ultem™ 1010 (Sabic)	Ultem™ 9085 (Sabic)	PPSU (Radel Solvay)	PEEK (Victrex)	PEKK (Arkema)
280 $[\frac{Eur}{Kg}]$	300 $[\frac{Eur}{Kg}]$	500 $[\frac{Eur}{Kg}]$	920 $[\frac{Eur}{Kg}]$	880 $[\frac{Eur}{Kg}]$

One of the main advantages of 3D printing PEI instead of other filaments is the price. Ultem is very cheaper compared to other high-performance thermoplastic materials. Ultem price is even 3 times lower than PEEK. Therefore, in industrial applications in which the requirements are comparable from all filaments, the Ultem has got great potential. The figure1.5 explains better the economic affordability of Ultem.

In the end, PEI is a great choice in terms of mechanical, thermal, chemical, flame resistance, and dielectric performances and it also cheaper than materials with comparable properties. PEI has got excellent properties for candidates as the best FFF-printed polymer.

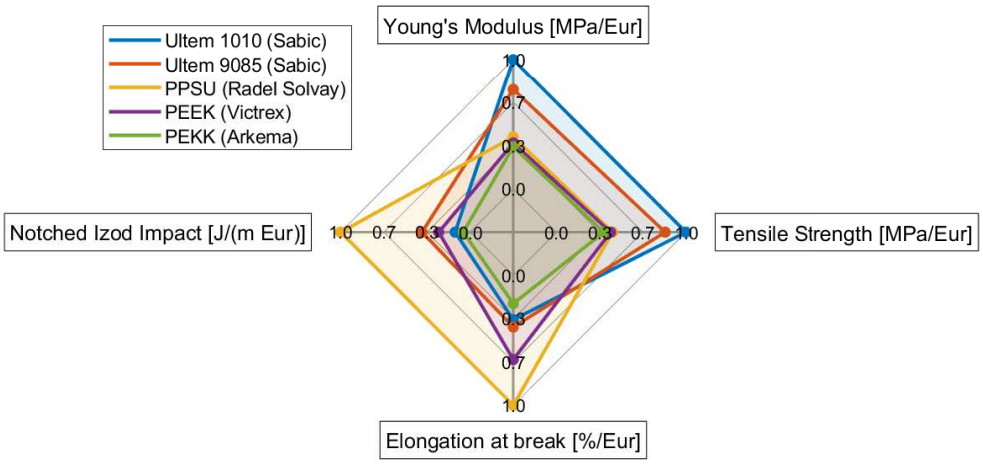

(a) Mechanical properties per material price

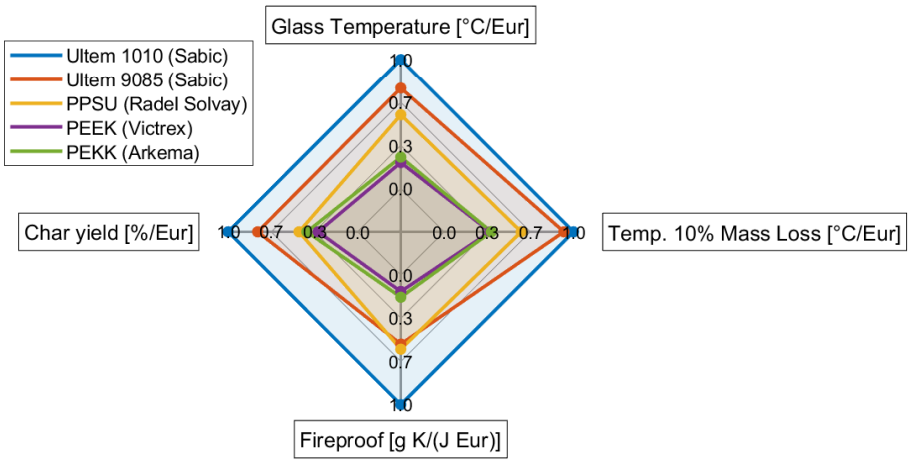

(b) Thermal properties per material price

Figure 1.5: Economic affordability

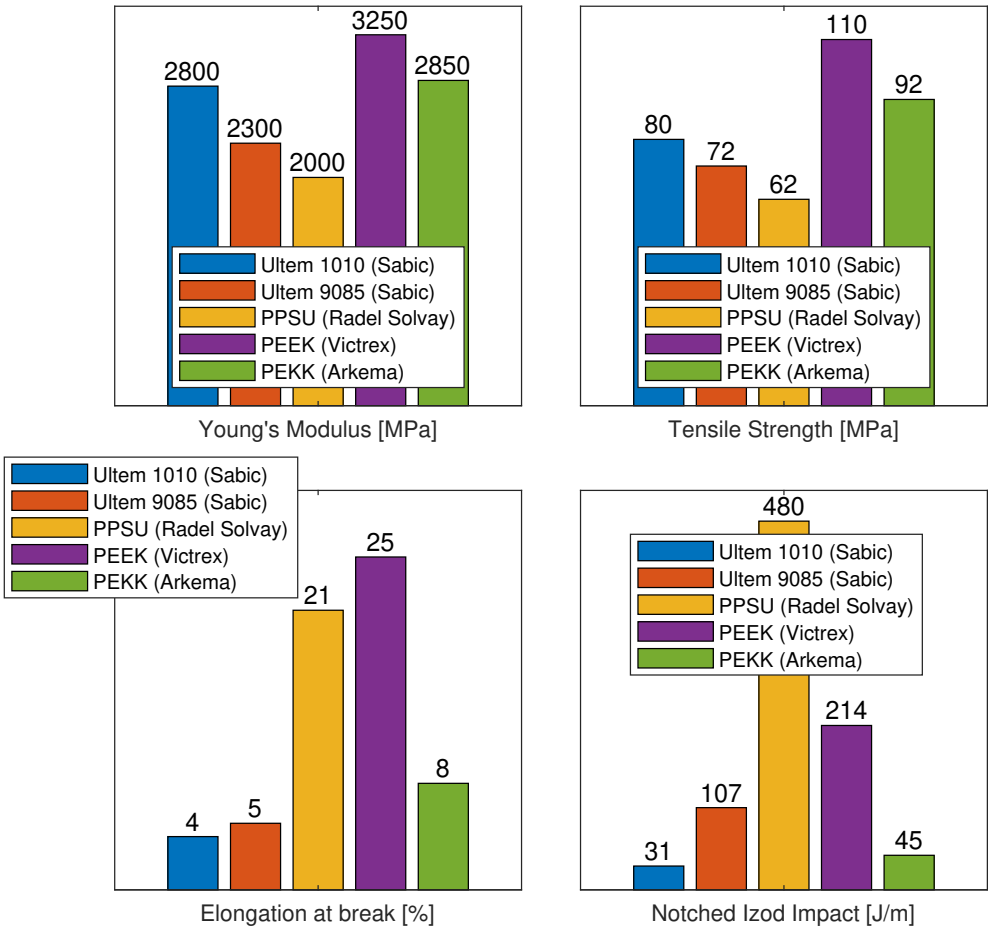

Figure 1.6: Mechanical properties of high-performance thermoplastic filaments

Chapter 2

Mechanical Performances of PEI Cellular Materials

2.1 Introduction

History teaches human is always and constantly looking for innovation, driven by the needs around them or by pure personal interest. Humans have brought clear improvements in the mechanical engineering field by studying the properties of new materials and their possible benefits in future industrial applications. For instance, the studies on composites in the 1980s made it possible to have lightweight shuttles and aircraft.

The main objective behind the development of materials remains the same over the years; the desire to obtain ever-better mechanical performance by covering increasingly difficult engineering needs. The materials development is well documented by Fleck et al.[1]. That review allows us to understand the history of the materials: from the Roman era to synthetic polymers.

An interesting strategy to understand what could be the materials of the future is a critical evaluation of the material properties diagrams, such as strength-density, stiffness-density, etc. Some parts of the charts are empty or not completely covered, these zones must be filled by research activities. Other parts will be inaccessible, but no one knows how long.

The first needs in antiquity were aimed at finding materials with ever-better mechanical strengths because they gave important advantages to the durability, and effectiveness of tools and weapons. In more recent times, the scientific community has been seeking materials with high strength at low weight; the leftmost part of the material properties diagrams with abscissa density. Materials with these characteristics tend to be lightweight, transportable, and efficient. Therefore, if they achieved high mechanical properties they would reach perfection. Mainly all industrial sectors are attracted to these materials. Among them, the aerospace, biomedical, automotive, naval and defence sectors are pushing on these materials. Figure 2.1 shows how the existing materials are distributed within the graph.

The charts reveal unfilled zones on the left side, above the foams. The scientific community are going to fill these zone with architected cellular materials. Therefore,

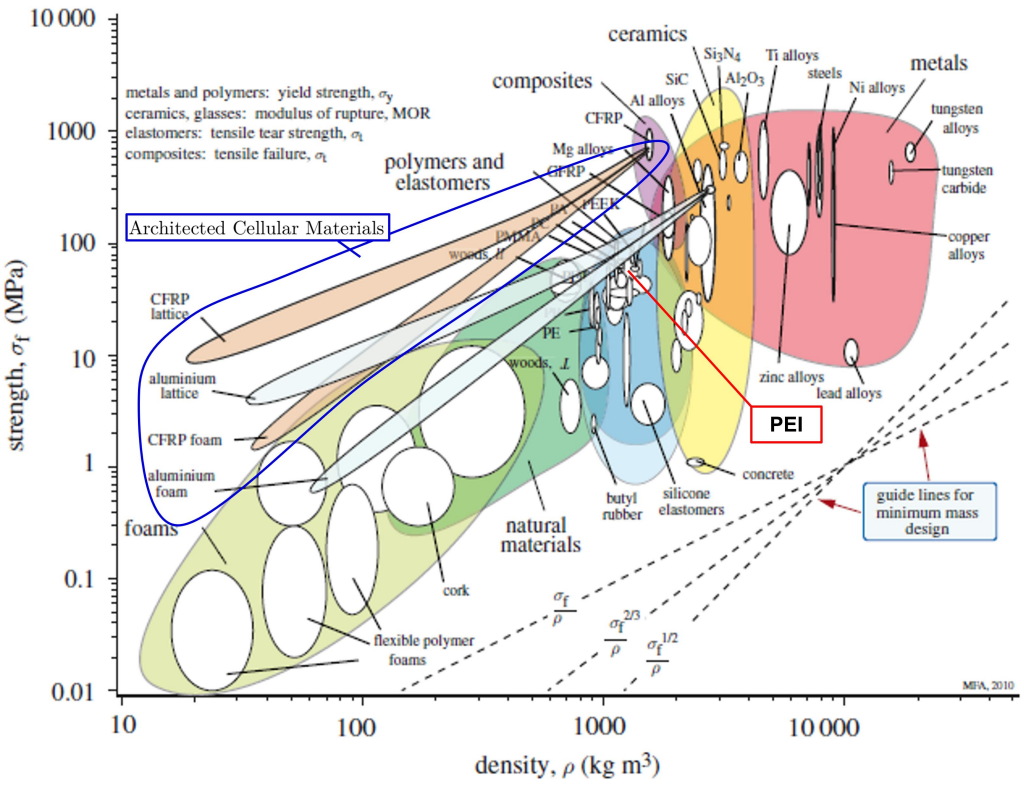

Figure 2.1: Material property charts of strength versus density for engineering materials. Predictions for cellular materials: foams and architected cellular materials. Architected cellular materials include honeycombs, cellular structures, and lattice structures. PMMA, polymethyl methacrylate; PA, polyamide; PEEK, poly ether ether ketone; PS, polystyrene; PP, polypropylene; PET, polyethylene terephthalate; PE, polyethylene; PC, polycarbonate; PTFE, polytetrafluoroethylene; CFRP, carbon fibre reinforced polymer; EVA, ethylene vinyl acetate; PEI polyetherimide [1].

this study aims to enrich the literature with achievable mechanical properties of PEI cellular materials.

The definition of cellular materials or cellular solids derives from a more elegant Latin word *cellarium*, i.e. cluster of cells in an enclosed space. There are several materials in nature which are shaped as an assembly of cells with solid edges, faces or structs such as wood, sponge, coral and cork [4]. These materials are usually confined inside the foams family on the materials properties diagrams in figure 2.1. That means the foams are a subfamily of cellular materials. Therefore, the scientific community has defined cellular materials or cellular solid as one made up of porous structure that is comprised of solid and void networks.

The cellular materials family is typically divided into two subfamilies: foams and architected cellular materials. Foams are cellular materials in which the distribution of the pores is stochastic or random. Architected cellular materials are cellular materials in which the solid part follows a specific shape, i.e. unit-cell or elementary

cell, and it is strictly periodically distributed inside the material space. Both foams and architected cellular materials are divided into open-cellular or closed-cellular materials according to the internal pores interconnectivity as shown the figure 2.2. Actually, some studies have distinguished foams and sponges based on pore interconnectivity (i.e. sponges for open cells, foams for closed cells) [2, 47].

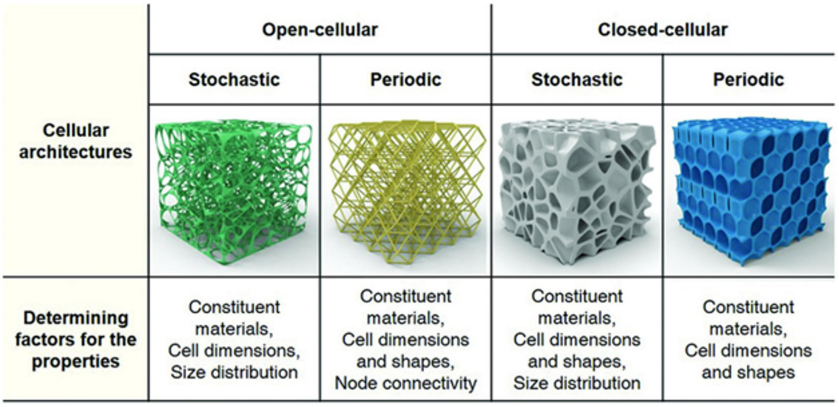

Figure 2.2: General classification of lightweight cellular materials according to the structural interconnectivity and randomness of the internal pores [2].

The architected cellular materials are subdivided into mainly two families based on the periodic unit-cell shape. If the unit-cell is designed or sketched in 2D dimension these materials are called honeycombs. Nature has inspired humans with the first honeycombs, that is the honeycombs manufactured by bees [27, 48]. Otherwise, if the unit-cell is developed in 3D dimension these materials are called lattice structures. Lattice structures are further divided based on the 3D shape nature. Especially, the strut-based lattice structures are characterized by a 3D shape where the solid part is made up of struts and nodes, such as cubes, octahedrons, spirals, BCC, CCC, cross-cube and other billions of structures based on connecting nodes in the unit-cell space with struts [2, 49]. The strut-based lattice structures evolved in recent years due to the higher specific strength achievable once the nodes are connected by plates instead of struts. These kinds of lattice structures are called plate-based lattice structures or briefly plate lattice structures [49, 17].

Obviously, the unit-cell shape was affected by the manufacturing process. Realizing extreme shapes were unthinkable 20 years ago[50]. Now, additive manufacturing technology enables the production of extremely complex shapes with quite all existing materials, from metals to composite materials [51]. That means the idea of connecting nodes with a solid part inside a unit-cell was overtaken thanks to Additive Manufacturing (AM). The solid part inside the unit-cell can be distributed freely so the unit-cell could have all kinds of shapes. Consequently, surface-based lattice structures were born. They are characterized by a 3D shape where the solid part is made up of continuous thin surfaces [49]. Some well-known examples are the Gyroid, Diamond or Schwarz lattice structure. The surfaces inside these structures

are based on the Triplic Periodic Minimal Surface (TPMS) theory. NASA researcher group was the first to figure out the strong potential of coupling TPMS structure with AM, indeed they discovered and printed the first TPMS lattice structures, i.e. Gyroid [52].

The most important feature of cellular materials is the relative density $\bar{\rho}$. It determines the ratio of cellular material density to the base material. From this parameter, the percentage of voids and solids can be determined and it enables the comparison of different cellular materials' performance. Thus, it becomes the key parameter to evaluate when the need to design components occurs. However, not all materials composed of voids and solids can be defined as cellular materials. Gibson and Asbhy defined a threshold, over 30% of relative density the cellular material becomes a solid containing isolated pores [4]. Actually, the literature accepts this threshold for foams but it is sceptical for architected cellular material.

As introduced before, additive manufacturing enables the manufacturing of quite all base materials without shape limits. These shapes are inspired by the nature as the bee honeycombs or defined by a retroactive design strategy based on the needs of the topology optimized shapes [27, 48]. That means the cellular materials have a strong possibility to fill the leftmost side of materials properties charts with abscissa density.

2.2 Designing and 3D printing of PEI Honeycombs

As aforementioned in the Introduction section, PEI is a high performance thermoplastic material. It has extreme potential in applications where the structural, thermal and toxicity properties are the must-have properties. The PEI amorphous microstructure gives it excellent 3D printability and restrained mechanical properties changing after the AM process. All these advantages bring PEI to be a highly valuable base polymer for cellular materials. The literature review shows a only few papers have investigated PEI cellular materials. This study aims to investigate PEI honeycomb's mechanical performances in order to evaluate the achievable properties of PEI cellular materials.

In recent years, several honeycomb shapes have been developed following a rational design able to reach a specific feature[53, 54]. Among them, the 2D auxetic honeycombs have become more and more relevant due to their flexibility and crashworthiness. The shape is defined as auxetic when the Poisson's ratio is lower than 0. That means the cross-section of the cellular materials becomes smaller when it is compressed and larger when it is stretched. This specific behaviour guarantees an increase of solid materials under the compressed zone enhancing the in-plane indentation resistance. Moreover, auxetic structures usually increase the fracture toughness and dynamic properties as impact energy absorption and wave attenuation performances [55]. Just imagine a complex structure as a sandwich panel under three-point bending, if the core was auxetic the structure would move under the

indenter and it theoretically increases the penetration properties and the absorption energy of the sandwich panel[56].

The auxeticity on 2D structures is obtained by means of geometrical considerations following kinematics rules, so the shapes behaves as a complex flexible joint [53]. This strategy is able to provide cellular materials with a lower Poisson's ratio than natural ones. The 2D auxetic structure are classified according to the auxeticity mechanism occurs during the deformation. Four main categories of auxetic structure are usually defined: re-entrant, chiral, elastic instability and rotating rigid structures [54, 56]. The re-entrant structures have hexagonal units with two negative angles. The principles behind this shape allows to reduce the cross-section pushing the re-entrant edge toward the center of the unit-cell. Chiral structures are based on the concept of chirality proposed by Kelvin [57, 55]. The auxeticity behaviour is given by the relative rotation of the unit-cell. Chiral structures are classified in chiral, anti-chiral or meta-chiral according to how the unit-cell is repeated to fill the volume [54, 56]. The rigid rotating structures are composed by geometries connected by hinges and corners. There are innovative shapes based on chirality principle able to rotate also out-of-plane during a compressive loading, this phenomena is called twisting [58, 55]. On the contrary, the elastic instability structures have an auxetic behaviour connected with local instabilities instead of rotational properties of hinges or ligaments [59, 60, 57].

The most common additive manufacturing technology able to manufacture PEI parts is Fused Filament Fabrication (FFF) or also named commercially by Stratasys Fused Deposition Modelling (FDM). This technology enables the production of polymer parts through the extrusion of melted polymer indeed it is part of the Material Extrusion (ME) additive manufacturing family. The FFF printer needs the polymer in the form of filament so it is rolled up in a spool with a diameter of 1.75 mm. The printer feeder pushes the filament across a high-temperature nozzle. Here, the filament is melted and it is ready to be deposited on the building plate. The printer moves the nozzle on the x-y plane following the instruction generated by a G-Code. The printer moves along the z axis direction once the layer is completed. These operations are repeated layer-by-layer up until the parts are completely manufactured. In this study, Apium FFF printer was used and Ultem 9085 product by Apium was chosen

The performances of PEI (Ultem 9085) honeycombs 3D printed through FFF are investigated only by Fores-Garriga et al. and Auricchio et. al.[61, 44, 62, 63]. Fores-Garriga evaluated how the topology of unit-cell influences Young's modulus of PEI honeycombs. He defined the analytical equation able to predict the analytical honeycomb stiffness based on linear elastic numerical results. Auricchio investigates the linear elastic properties of tetrarchical and bi-tetrarchical honeycombs. Both of them compare the linear elastic properties of PEI honeycombs with numerical and analytical results. This study aims to investigate the elastic, plastic, and energy absorption properties of PEI honeycombs. So overall mechanical performances are

evaluated, focusing the study on the entire stress-strain honeycombs curves.

Among these high numbers of 2D auxetic structures, three different unit-cells were chosen: the well-known Re-Entrant shape, S-shape and I-shape. The latter unit-cells belong to a chiral auxetic family and they are fashioned following the anti-chiral strategy, as the figure2.3 shows. In addition, the traditional hexagonal structure was also analyzed in order to have a comparison of mechanical properties with a deeply studied honeycomb. The honeycombs CAD models were designed by

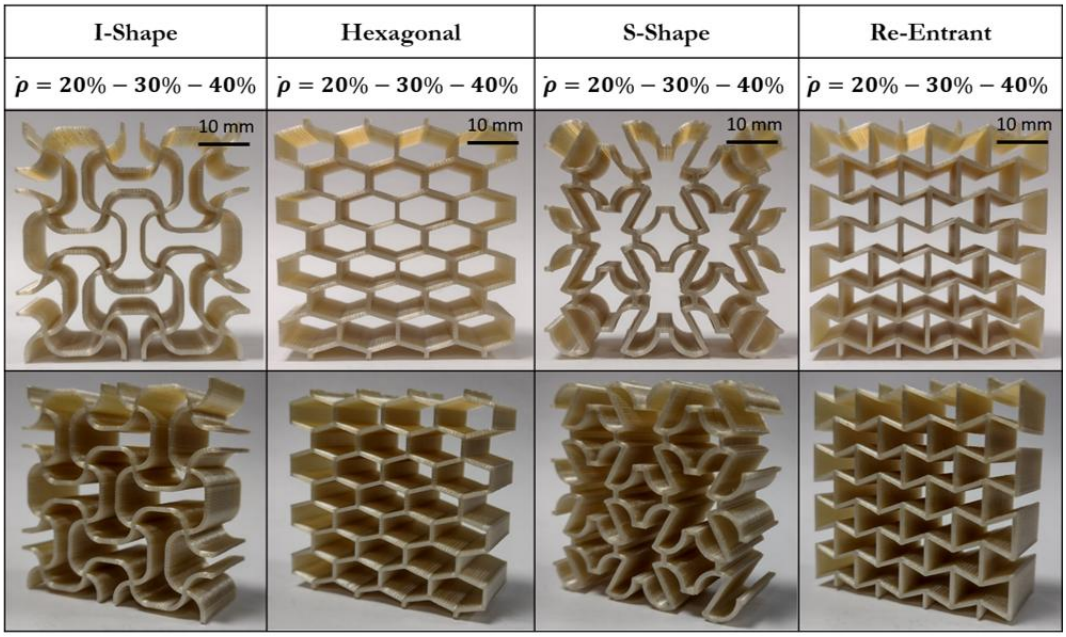

Figure 2.3: Additively manufactured PEI cellular materials: Hexagonal, Re-Entrant, I-Shape, and S-Shape honeycombs.

means of nTopology©software. Thanks to nTopology the STL were exported and subsequently imported on slicing software Simplify 3D©to create the G-Code and set all printing parameters.

Three different relative density was chosen; 20%, 30%, and 40% as shown in figure 2.4. The honeycombs' sizes are 48x48 mm and the width is 24mm. A fashion of 4x4 unit-cells ensures an acceptable correspondence of overall honeycombs' mechanical properties with the predicted one by means of Representative Volume Element theory [64, 49]. Thus, the mechanical properties should not be affected by the boundary condition, e.g. friction between the upper and lower faces with the compressive plates. The mechanical properties can be evaluated following the well-known relationship between engineering stresses and strains. Otherwise, the mechanical properties shuold have been evaluated only in terms of force displacement [65, 66, 49].

The overall sizes were defined accurately in order to have a higher correspondence between CAD models and printed parts. The unit-cell of 12x12mm guarantees the lower thickness of the re-entrant ligament could be printed with the Apium printer

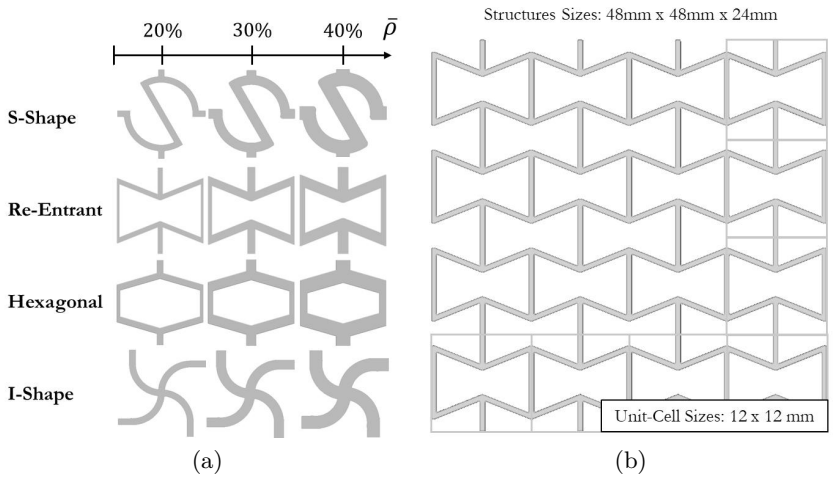

Figure 2.4: Geometric models of the 2D lattices. (a) Unit-cell topologies in funtion of relative density. (b) 3D printed honeycombs configuration and sizes.

with a nozzle of 0.4 mm. The lowest printed ligament thickness is 0.8 mm due to several factors that disable geometric features smaller than that value [67, 68]. In order to avoid out-of-plane failure and layers delamination, the layer height is 0.1 mm achieving high bonding strength between the stacked layers. Obviously, the mechanical properties are affected by the manufacturing process so the same printing parameters were used for all kinds of structures. Table 2.1 shows all print settings and they are based on our extensive testing in the laboratory. They ensure the best choice in strength, printability, and size accuracy. Due to the increase of

Table 2.1: FFF printing parameters for Apium PEI (Ultem 9085).

Layer height $[mm]$	Nozzle diameter $[mm]$	Printing speed $[mm/min]$	Extruder temperature $[^{\circ}C]$	Bed temperature $[^{\circ}C]$	Infill percentage $[\%]$	G-code software
0.1	0.4	2000	370	120	100	Simplify 3D

honeycombs' relative density, the ligament thickness increases as well. If two parallel filaments were printed too far, the bonding strength between the deposited in-plane filaments will be lower [69, 70]. That brings high quantities of porosity between the filament and, also, the measured relative density will no longer be compatible with the predicted one. Therefore, the unit-cell of 12x12mm ensures that all honeycomb ligaments were filled correctly ensuring the same bonding condition between the deposited in-plane filaments as the cell-wall thickness increases. To confirm the quality of the printed honeycomb the measured relative density was compared to the predicted one computed through CAD models, as shown in table 2.2. The ρ_{CAD} is the density predicted by nTopology©software imposing the PEI density of 1270 kg/m^3 (PEI filament density produced by Apium). The ρ_M is the measured honeycomb density. n_f is the number of extruded filaments inside the ligaments.

The thickness of ligaments in the CAD models, i.e. t_{CAD}, are perfectly consistent with the measured ones, i.e. t_M. Therefore, the slightly lower relative density measured is only connected to the porosity between the extruded filament inside the ligaments.

Table 2.2: Measured and predicted PEI honeycombs features and sizes.

Unit-cell Topology	$\bar{\rho}_M$ [%]	ρ_M $[kg/m^3]$	$\bar{\rho}_{CAD}$ [%]	ρ_{CAD} $[kg/m^3]$	t_M $[mm]$	t_{CAD} $[mm]$	n_f -
Re-Entrant	20.02	254.25	20	254	0.81	0.80	2
Re-Entrant	29.83	378.84	30	381	1.11	1.10	2
Re-Entrant	39.74	504.69	40	508	1.41	1.40	3
Hexagonal	19.91	252.85	20	254	0.90	0.90	2
Hexagonal	29.87	379.34	30	381	1.41	1.40	3
Hexagonal	39.68	503.93	40	508	1.90	1.90	4
S-Shape	19.93	253.11	20	254	0.91	0.90	2
S-Shape	29.88	379.47	30	381	1.34	1.33	3
S-Shape	39.71	504.31	40	508	1.79	1.79	4
I-Shape	19.94	253.23	20	254	0.90	0.90	2
I-Shape	29.89	379.60	30	381	1.37	1.37	3
I-Shape	39.70	504.19	40	508	1.82	1.81	4

2.3 Mechanics of cellular materials

The mechanics of cellular materials is strictly dependent on the unit-cell topology and on solid material properties. The shapes of unit-cell could be read as kinematism where joints and struts make up continuous material. Therefore, the unit-cell behaviour under loading is ruled by the nodal connectivity as well as for a kinematism [1]. Typically, the mechanical behaviour of cellular materials is divided into two distinct species: stretching-dominated and bending-dominated behaviour. This mechanical response is illustrated by characteristic stress-strain curves, as depicted in figure2.5. The difference between a bending-dominated structure and a stretching-dominated structure is strictly linked to the collapse mechanism close to the pin-jointed structure. Stretch-dominated structures present a high nodal connectivity level that locks material rotation around hinges[1]. Ligament sections carry tensile or compression stress state giving high stiffness and strength to the overall cellular materials such as hexagonal, re-entrant, iso-grid, Kelvin, and so on unit-cells. The stress-strain curve usually has got high peak stress before plastic deformation, usually called collapse stress or initial collapse stress. The stress drops off instantly followed by fluctuations or breaking. The collapse mechanism is governed by pure stretch, buckling or fracture-stretch phenomena[47].

The bending-dominated structures present lower initial collapse stress because of lower nodal connectivity. The unit-cell turns out to be flexible because the ligaments

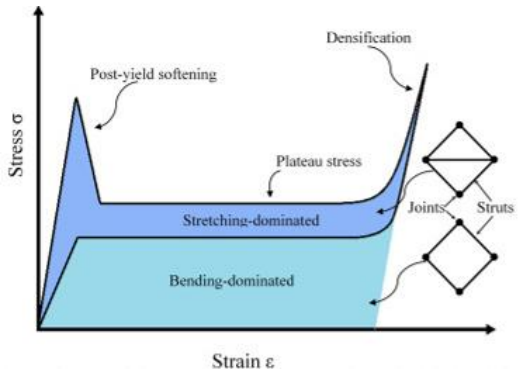

Figure 2.5: General compressive mechanical behaviour for bending- and stretching-dominated cellular materials with same relative density [3].

or solids withstand a bending load instead of a compression-tension one. Obviously, slender ligaments are much stiffer when stretched than when bent. Once the collapse stress is reached, the stress-strain curve appears linear, i.e. plateau region, and the collapse mechanism is governed by pure stretch, buckling or fracture-stretch phenomena. This stress-strain curve peculiarity provides the cellular materials with high absorption energy performance [49].

After the first peak and plastic or plateau regimes, the stress-strain curves have the last stage, i.e. densification regime. The densification stage represents the beginning of cells walls interactions. Once the cellular material is completely compressed, the voids are getting more and more closed. Therefore the cellular solid is defined as compacted when it reaches a critical strain, i.e. densification strain ε_d. The densification strain is the critical strain where the cell walls jam together and beyond this strain, the slope of the stress-strain curve tends to be close to the base material ones. It is a crucial parameter to evaluate the real effectiveness to absorb energy for cellular materials[71].

However, the energy absorption capacity should be evaluated up to the onset strain of densification, i.e. ε_{cd}. In any application involving energy absorption and protection, both the onset strain of densification and the densification strain play important roles. The onset of densification strain is not always easy to be determined as in the figure2.5. The real structures exhibit a smooth transition between the plastic and densification stages. Several failures can occur during the plastic phase that creates peaks and drops in the curve. In literature, there are many examples of the confusion between the densification strain and the onset strain of densification[71]. To unify the onset densification strain determination Li et al. identified four methods:

- Method-I: The onset strain of densification is defined by the intersection of the tangents to the stress plateau regime and the densification regime.
- Method-II: The onset strain of densification is defined as the strain at the last local minimum before the stress rises steeply.

- Method-III: The onset strain of densification is defined as the strain at which the slope of the tangent is equal to that of the elastic regime.
- Method-IV: The onset strain of densification is defined as the strain at which the maximum energy absorption efficiency occurs.

In this study, Method-III was used.

Once the densification strain was obtained, the absorption energy properties of PEI honeycombs can correctly be compared. The Specific Absorption Energy (SEA) is the key value to calculate and it is expressed as follows

$$SEA = \frac{1}{\rho} \int_0^{\varepsilon_{cd}} \sigma(\varepsilon)\, d\varepsilon \tag{2.1}$$

It is an indicator able to quantify how the cellular material is predisposed to absorb energy during a compression loading or an impact [72]. A high SEA value corresponds to a high location of the cellular material on materials properties charts as it is explained in the Introduction section.

In summary, the results that will be obtained and discussed from the experimental test are Young's modulus, Poisson's ratio, initial collapse stress, onset densification strain and specific absorption energy.

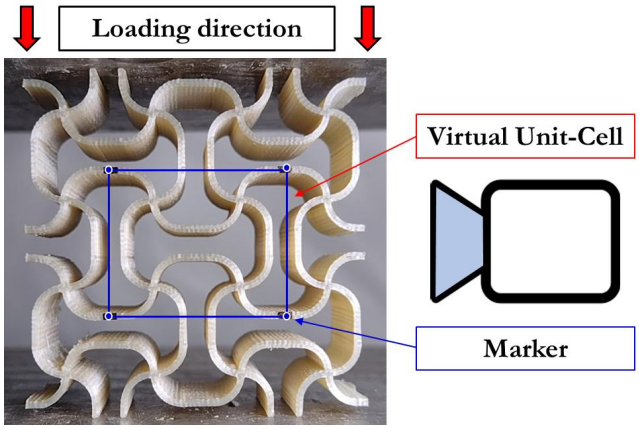

Figure 2.6: Experimental test set up.

In this study, the PEI honeycombs were compressed under quasi-static loading to evaluate the effective stiffness, strength, Poisson's ratio and energy absorption characteristics. A universal tensile machine Zwick/Roell©Z050 equipped with a 50kN load cell was used to perform the quasi-static compression tests. The load was applied at 2 mm/s to enforce the quasi-static condition, i.e. strain rate less than 0.001 1/s [73]. To measure the Poisson's ratio and to monitor the plastic deformation a professional camera recorded the entire compression test. The camera was located perfectly perpendicular to the in-plane section and 4 markers were drawn on the honeycombs' faces, as shown in figure 2.6. The markers were tracked during the compression test through an image analysis technique and a virtual unit-cell was

defined [74]. Thanks to Digital Image Correlation (DIC) based on grid methods the strains on vertical and horizontal directions were measured[75]. The ratio between them coincides with Poisson's ratio. Those values were compared with the numerical ones obtained through Representative Volume Theory (RVE).

2.4 Experimental Results

The in-plane compression behaviour of PEI honeycombs was analyzed in terms of stress-strain curves and deformation maps captured at different relevant stages of loading. The stress-strain curves of PEI honeycombs with $\bar{\rho} = 20\%$ are shown in figure2.7a. The stress-strain curves exhibit three well-known regimes: an initial linear elastic phase, a plastic phase where the honeycombs can have a stable plateau or unstable stress fluctuations, and the densification phase where the stress increases up to reaching a slope similar to Young's modulus of the base material. As figure 2.7a shows, the collapse response is dependent on the unit-cell topology. The A stages in figure 2.7a determine the strain in which the first failure occurs. The A point coincides with the initial collapse of the honeycombs except for the I-shape as its stress-strain curves keep increasing. The B stages in figure 2.7a determine the collapse maps after the initial collapse stress except for the I-Shape where the B stage is associated with the initial collapse stress.

The re-entrant honeycomb shows a stretching-dominated behaviour due to its high stiffness and sudden drop in stress. The collapse mechanism is governed by the buckling phenomenon of the unit-cell walls as the figure2.7b shows. The buckling phenomenon creates an unstable response but its occurs layer-by-layer up to the honeycombs being compacted[76]. The re-entrant honeycombs don't show fractures or breaks but only extensive plastic deformation.

The hexagonal honeycomb shows a stretching-dominated behaviour as well as the re-entrant one. The collapse mechanism is governed by failure inducted by the onset of snap-through buckling of the upper and lower unit-cell arches[77]. The PEI ligaments inside the hexagonal unit-cell are not able to reach the second equilibrium state thus the ligaments break, as the figure2.7b shows. The collapse mechanism occurs layer-by-layer up to the honeycomb being compacted.

The I-shape and S-shape honeycombs show a bending-dominated behaviour due to the unit-cells topologies. Both unit-cells don't show an extended linear elastic stage as the re-entrant and hexagonal cells do. The first stress-strain stage became a nonlinear elastic stage due to the change in the slope of the stress-strain curve. The stage is defined as elastic because once the load is removed the honeycombs go back to the undeformed shapes. This behaviour is generated by the local rotation of the ligaments, resulting in contacts increasing between adjacent cell walls and the formation of additional load transfer paths, as the figure2.7b shows. Although the S-shape shows failures in the "S" conjunctions, both unit-cells are progressively compressed up to the honeycombs that are compacted.

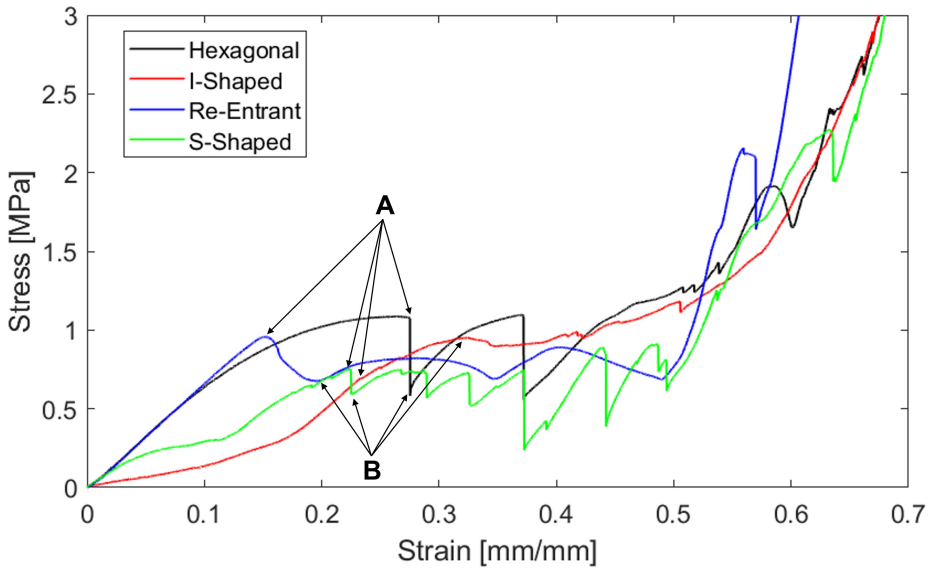

(a)

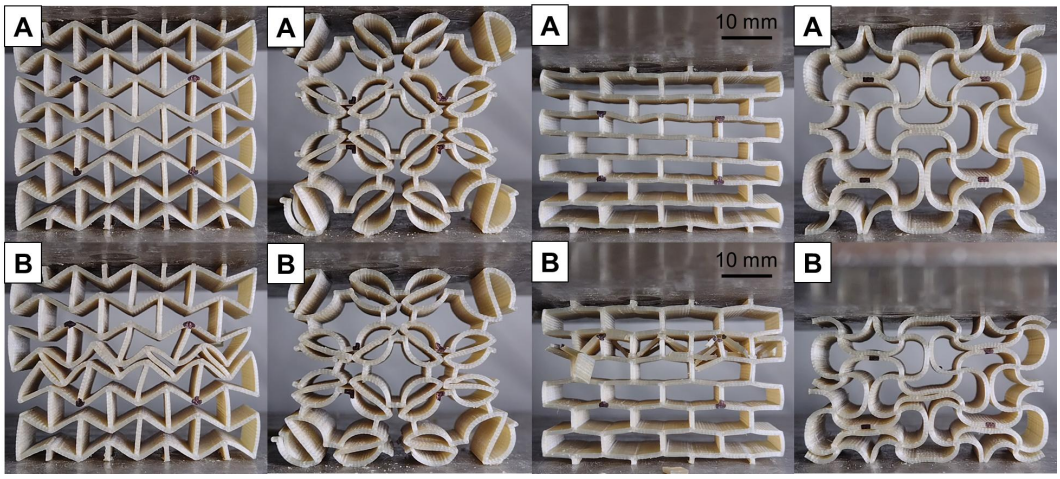

(b)

Figure 2.7: In-plane quasi-static compression behaviour of PEI honeycombs with $\bar{\rho} = 20\%$. (a) Characteristic stress–strain curves. (b) Deformation maps at various stages.

The mechanical response of PEI honeycombs changes as their relative density increase. The stress-strain curves of PEI honeycombs with $\bar{\rho} = 30\%$ are shown in figure2.8a. The collapse mechanism for each kind of structure remains unchanged as well as their stretching or bending-based behaviour. The A stages in figure 2.8a determine the collapse maps after the initial collapse stress.

The stress-strain curves rise obviously toward higher stress values but the fluctuations in the plastic regime became greater. These fluctuations are generated by a further failure mode of 3D-printed PEI. The honeycombs' solid part is composed of multiple deposited PEI extrusions since the part are manufactured through

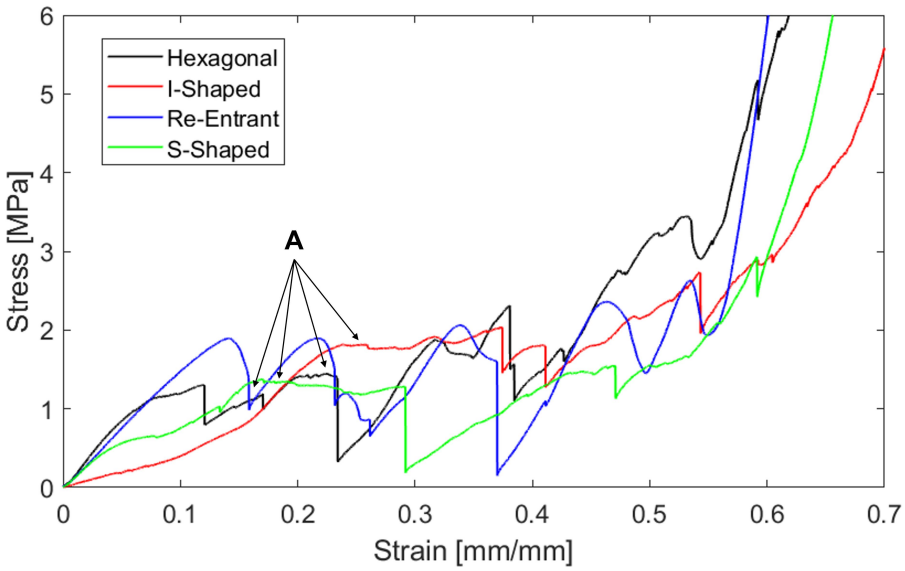

(a)

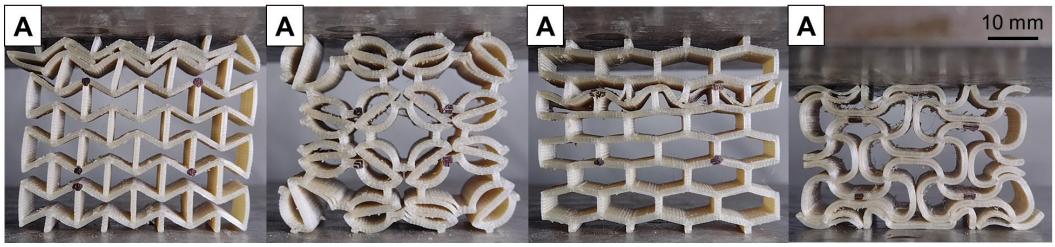

(b)

Figure 2.8: In-plane quasi-static compression behaviour of PEI honeycombs with $\bar{\rho} = 30\%$. (a) Characteristic stress–strain curves. (b) Deformation maps at various stages.

fused filament fabrication. That means the honeycombs' solid part can be affected by traditional failure for crack propagation in solids and meanwhile by debonding PEI extruded filaments along their interfaces. A similar failure mode is called delamination and it is common in laminated composite materials, e.g. Carbon Fibre Reinforced Materials (CFRP), concretes and coated structures where the crack has a preferential path to propagate due to the manufacturing process, i.e. the material fracture in layers [78].

In 3D printed parts the delamination can occur along the stacked layers (parallel building plate) or along the interfaces of deposited filaments (inter-layer delamination). In these PEI honeycombs, the stacked layers' delamination was prevented by printing parameters, for example, the height of the layer was reduced to 0.1 mm. However, the deposited filaments debonding keep going to be there when the number n_f is greater than 2, as the figure 2.8b shows. The S-shape, I-shape and hexagonal honeycombs show a delamination failure instead of a brittle break as

in honeycombs with $\bar{\rho} = 20\%$ occur. The delaminations are quite noticeable in figure2.8b, inside the honeycombs ligaments are creating voids along the filaments interfaces. The debonded filaments start to deform independently reducing the integrity of the unit-cells. The re-entrant is the only one that continues to fail as in the lower density, indeed its n_f is 2.

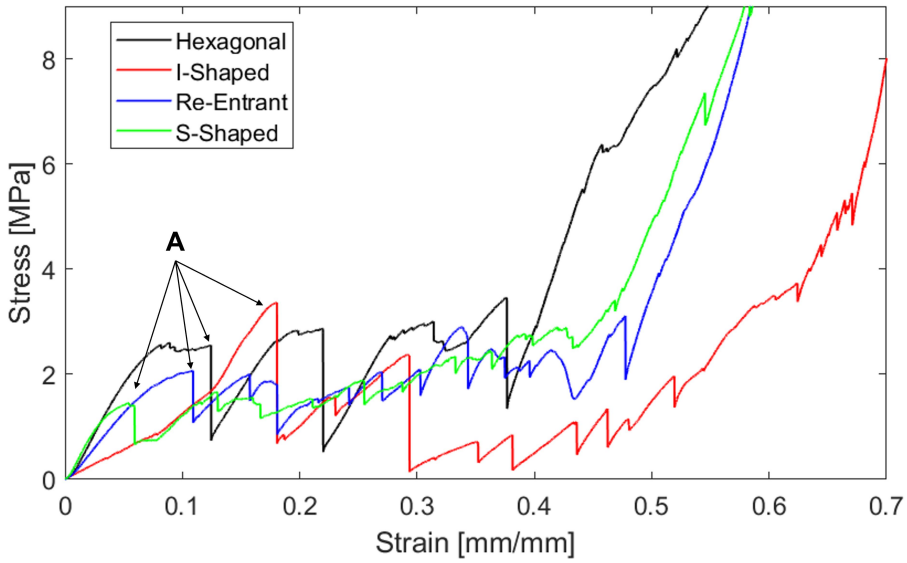

(a)

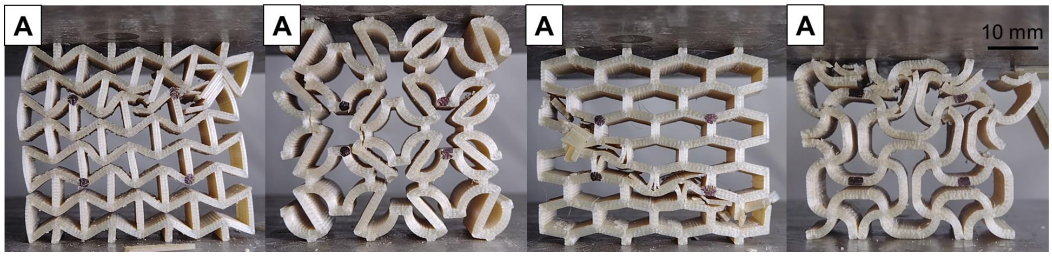

(b)

Figure 2.9: In-plane quasi-static compression behaviour of PEI honeycombs with $\bar{\rho} = 40\%$. (a) Characteristic stress–strain curves. (b) Deformation maps at various stages.

The stress-strain curves of PEI honeycombs with $\bar{\rho} = 40\%$ are shown in figure2.9a. The A stages in figure 2.9a determine the collapse maps after the initial collapse stress. The stress-strain curves do not rise toward higher stress values as aspected. The fluctuations in the plastic regime became higher and higher.

Also in this case the failure modes are governed by delamination failure and brittle breaking. However, the collapse mechanism of some honeycombs changed. The hexagonal and S-shape honeycombs exhibit a shear band formation. The density increase gives a high stiffness to the unit-cells so the instability phenomena can no longer be generated. All honeycombs reduced their elastic deformation before

reaching the initial collapse stress.

The linear elastic properties, i.e. Young's modulus and Poisson's ratio, of PEI honeycombs under in-plane quasi-static compression are compared in figure 2.10. Both values are calculated up to $\varepsilon = 0.02$ because of the nonlinear response of the I-shape and S-Shape unit-cells. The Young's modulus of re-entrant and hexagonal honeycombs with $\bar{\rho} = 20\%$ are similar in magnitude and the values are the highest. The collapse mechanism nature bears out the experimental result: a stretching-dominated structure is stiffer than a bending-dominated one. Since S-shape has got two vertical lattice members connected quite vertically by the "S" angled line, this honeycomb shows great stiffness even if it is defined as bending-dominated. Obviously, Young's modulus of the I-shape honeycomb turns out to be the lowest. The honeycombs' Young's modulus increases as their relative density increases.

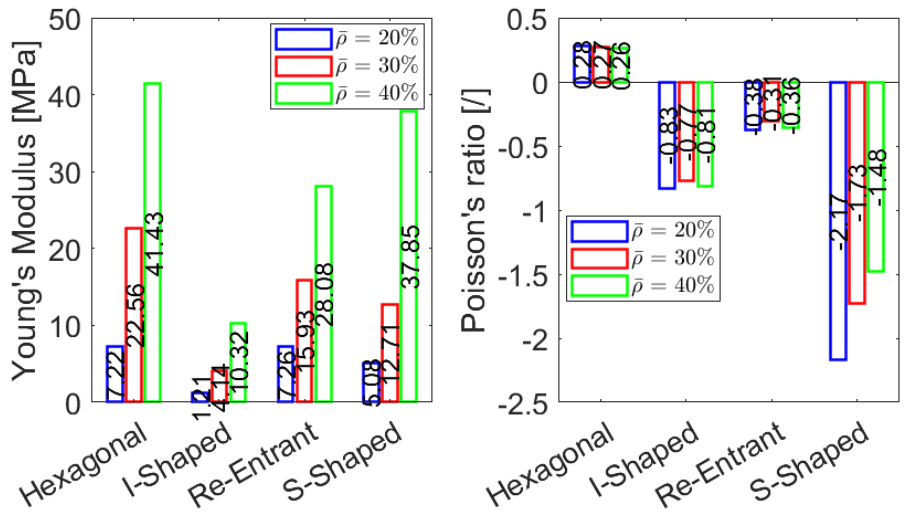

Figure 2.10: In-plane performance of PEI honeycombs under quasi-static compression loading: Young's modulus and Poisson's ratio.

The Poisson's ratio was calculated in the same strain range that Young's modulus was. The S-shape honeycombs have the lowest Poisson's ratio. It can be quickly confirmed by the deformed shape in figure 2.8b. The S-shaped topology allows you to reduce to the cross section by folding the "S" shape and converging the unit cells around it to the centre. However, the vertical direction has a great stiffness as it is confirmed by Young's modulus. That means the ratio between the horizontal and vertical strain is extremely high. As the density increase, the Poisson's ratio tends to be similar except for the S-shape honeycomb. The thickness of cell walls increases reducing the folding movement of the "S". Furthermore, the results show auxeticity based on the re-entrant principle is lower than the auxeticity based on the chiral one.

The capacity to absorb energy by plastic deformation of PEI honeycombs is evaluated by comparing the initial collapse stress, densification strain, and specific energy

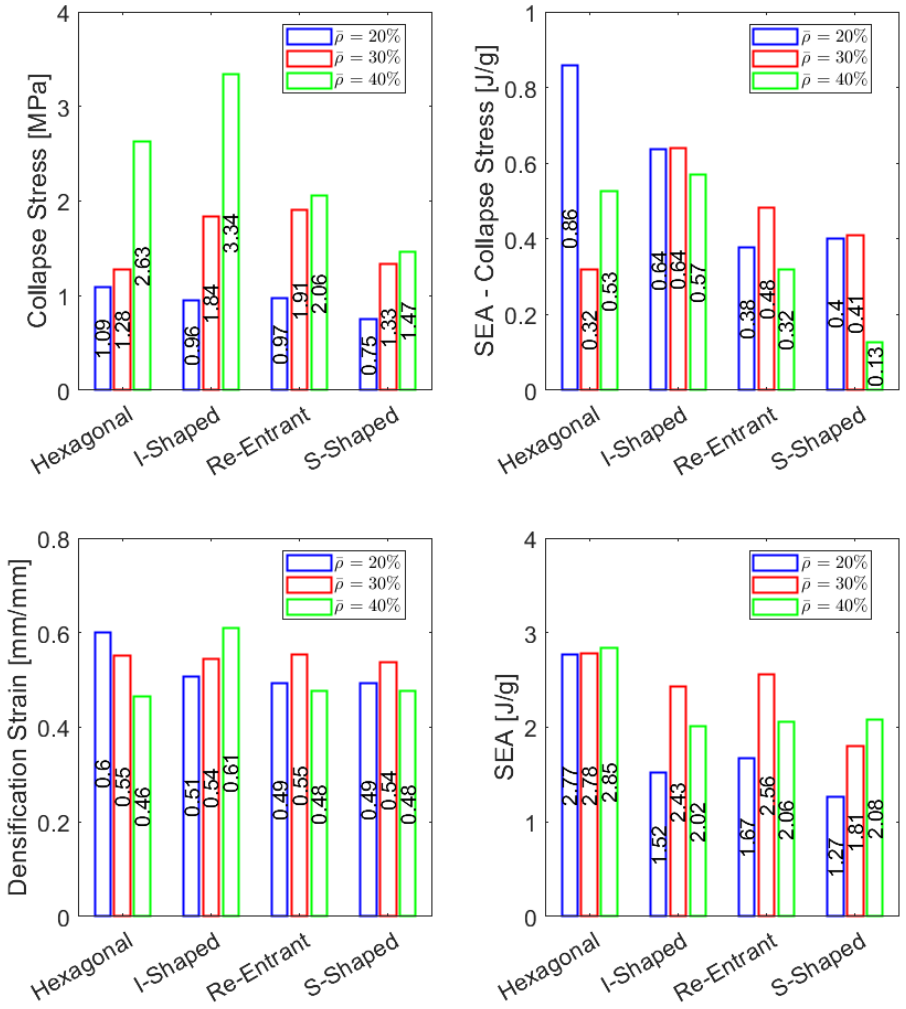

Figure 2.11: In-plane crashworthiness of PEI honeycombs under quasi-static compression loading: Initial collapse stress, specific energy absorbed up to the initial collapse stress, densification strain, and specific energy absorbed up to densification strain.

absorption. The stretching-dominated unit-cells should have had the highest initial collapse stress. However, the I-shape and S-shape exhibit collapse stress similar to the other ones. The S-shape and I-shape topology evolves during the compression loading, creating new wall interactions and increasing the overall stiffness structure, as the figure2.8a have shown yet.

The SEA was also calculated up to the initial collapse stress, i.e. SEA_{CS}, to evaluate the storable energy by the honeycombs before the collapse. The hexagonal structure with $\bar{\rho} = 20\%$ exhibits the highest SEA_{CS}. That means the density increasing does not allow to reach higher mechanical performances. The SEA_{CS} for all kinds of structure decreases when the delamination failure mode appears on

the structure. This thesis is confirmed by the re-entrant honeycombs SEA_{CS}. The SEA_{CS} increases when the $\bar{\rho} = 30\%$ (no delamination, figure 2.9a) and then decrease at $\bar{\rho} = 40\%$.

The highest SEA was achieved by the hexagonal honeycombs with $\bar{\rho} = 40\%$. However, the SEA of the hexagonal structure with $\bar{\rho} = 20\%$ is similar. That means an increase in density does not allow a SEA increase. The delaminations that occur on hexagonal honeycombs limit a possible increase in stress. The delamination failure mode is filtering the mechanical performances. This filtering is lower in bending-dominated structures due to the SEA keeps increasing even if it is not increasing as aspected.

In literature, it is well-known the cellular materials SEA increases when the relative density increase, as well as the SEA_{CS} [4, 65, 66]. The main assumption behind this statement is the integrity of the structure. However, if the solid part of cellular materials had different failure modes and the unit-cell integrity was lost, the theory could be invalidated. Several papers show a SEA decreasing for 3D printed cellular materials as the density increase [17, 18]. Therefore, the cellular materials printed by FFF should have high-strength bonding interfaces between the in-plane deposited filaments to achieve greater mechanical performances, i.e. no defects.

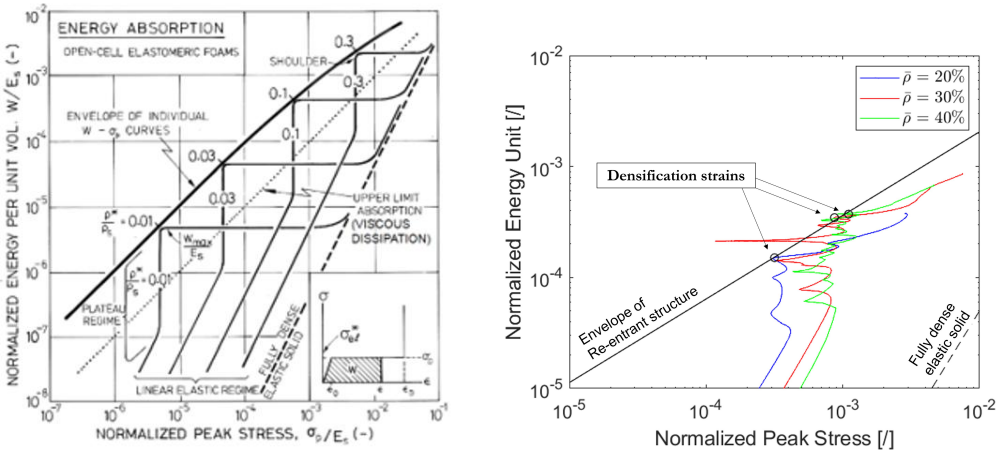

(a) (b)

Figure 2.12: The construction of energy absorption diagram. (a) Considerations obtainable from the graph [4]. (b) The construction of PEI Re-Entrant honeycomb envelope.

The hexagonal honeycombs show the best mechanical performances. However, the capacity to absorb the energy of cellular materials can not be only determined by evaluating the SEA, initial collapse stress and densification strain. In impact dynamics, a good impact attenuator or protection must generate a low peak force on the protected item and absorb the highest energy amount. The absorption energy is governed by the plateau regime while the peak force magnitude is a function of initial collapse stress. The best combination should be low collapse stress and a long

plastic regime. For this reason, the cellular materials are usually tailored or graded to give the best combination[72, 79].

Gibson and Ashby suggested visualizing the energy absorption characteristics of cellular materials on energy-absorption diagrams [4, 5]. The diagram proposed by Gibson and Ashby is depicted in figure2.12a. In order to construct the diagram, two adimensional parameters need to be introduced: Normalized Peak Stress (NPS) and Normalized Energy Unit (NEU). These values are calculated from the experimental stress-strain curves as follows

$$\begin{aligned} NPS &= \frac{\sigma_p}{E_s} \\ NEU &= \frac{1}{E_s}\int_0^{\varepsilon} \sigma(\varepsilon)\, d\varepsilon \end{aligned} \tag{2.2}$$

where the E_s is the Young's modulus of the solid part. σ_p is the maximum permitted compressive stress.

The NPS and NEU associated with stress-strain curves of cellular materials at different relative densities are plotted on energy-absorption diagrams. There is a line that passes through all onset of densification strains where the curves shape a shoulder, as shown in figure2.12b. The heavy line divides the diagrams into two parts: the lower zone is the energy the cellular material can absorb and the upper zone is the energy the cellular material can not absorb, as shown in figure2.12a. Thus, the heavy line coincides with the optimum cellular material density to absorb specific energy. The higher the envelope, i.e. the heavy line, and greater will be the capacity to absorb the energy of cellular material.

Consequently, the energy-absorption diagrams of PEI honeycombs are obtained in figure2.13. To avoid a cumbersome chart, the NPS and NEU curves are substituted by coloured patches associated with the unit-cell type. The re-entrant honeycombs exhibit the highest envelope in the density tested range. That means the re-entrant structure is the best honeycomb to absorb energy in dynamic conditions. Cellular material with low collapse stress, high densification strain and high energy absorption is the best combination. The envelope could be extended beyond the tested density range. The hexagonal honeycombs foresee higher envelope at low-density regions. However, confirming this prediction needs more tests.

Once all mechanical performances of PEI honeycombs are evaluated, the obtained values are plotted in material properties charts. The Ashby chart of energy absorption was chosen because the honeycombs' applications are usually as impact attenuators, shock absorbers or cores in sandwich panels. The Ashby map needs the energy unit capacity (EAC) and its expressed by the equation

$$EAC = \int_0^{\varepsilon_{cd}} \sigma(\varepsilon)\, d\varepsilon \tag{2.3}$$

This value correspond to the points on envelope line in energy-absorption dia-

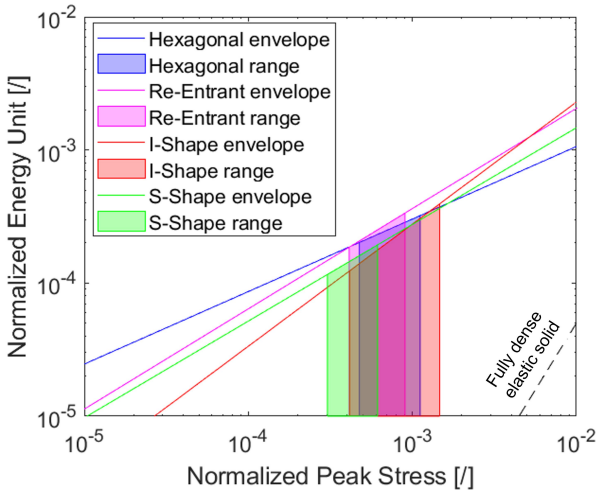

Figure 2.13: Energy absorption diagrams of PEI cellular materials.

grams. Figure 2.14 shows the Ashby map where foams and auxetic lattices are found togheter [5]. PEI honeycombs show a capacity to absorb energy similar to the alu-

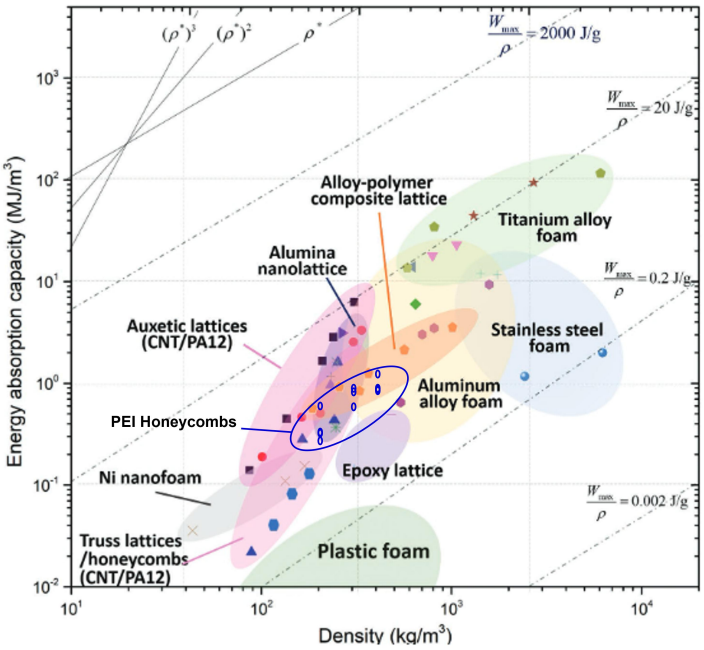

Figure 2.14: Ashby map of energy absorption per unit volume versus density [5]. The PEI cellular materials properties are depicted by blue circles.

minium alloy foams and slightly lower than alloy-polymer composite lattices. The honeycomb SEA is similar to aluminium alloy and stainless steel foams. As compared with the auxetic lattices, the EAC is lower due to the unit-cell topology. In fact, the energy absorption capacity of the auxetic structure also outperforms tradi-

tional cellular materials such as honeycomb and foam. This is because the topology of auxetic lattices is developed in 3D. Thus, the entire structure works to withstand the load. Honeycombs have solid material normal to the in-plane direction, extruding the unit-cell topology. That means out-plane material is not optimal distributed inside the overall volume. However, PEI honeycombs are a good choice in industrial applications substituting metals or polymer foams.

2.5 Concluding remarks

Four different honeycombs were designed: three 2D auxetic unit-cell topologies and one 2D rubbery unit-cell topology , i.e. re-entrant shape, S-shape, I-shape, and hexagonal. The unit-cells were arranged 4x4 to create honeycombs in which the relative density runs from $\bar{\rho} = 20\%$ to $\bar{\rho} = 40\%$. Honeycombs made of high-performance glassy thermoplastic material PEI were 3D-printed through fused filament fabrication technology.

The mechanical performances and energy absorption properties were evaluated by testing honeycombs under quasi-static compression loadings. Young's modulus, Poisson's ratio, initial collapse stress, SEA, and energy absorption capacity were calculated for each test and then compared to each other. The experimental results reveal a mechanical performance dependency on the additive manufacturing process. The high densities honeycombs exhibit a premature failure along the extruded filament interfaces inside the cell walls, i.e. interlayer delamination, that avoids reaching higher mechanical properties than low-density honeycombs have.

The overall honeycombs' mechanical performances are depicted in figure 2.15 thanks to spider plots. According to quasi-static considerations, the non-auxetic hexagonal honeycombs enable the best balance in stiffness and absorbed energy properties that are normally antagonistic. In fact, the envelope associated with hexagonal unit-cells in spider plots results in the largest. Moreover, the I-shape unit-cells show a highly valuable performance up to the initial collapse stress. The lower stiffness followed by high initial collapse stress and a high SEA up to this point guarantees the best properties in the elastic regime.

According to dynamic considerations, the auxetic re-entrant honeycombs enable the best balance in absorbed energy properties and collapse stress. In fact, the re-entrant unit-cell is able to absorb high energy amounts without increasing the collapse stress in the plastic regime, as shown in figure 2.13. The hexagonal honeycombs might overtake the re-entrant honeycombs' properties but the interlayer delaminations inside them prevent that.

In conclusion, PEI honeycombs show great potential in mechanical and absorption properties similar to the aluminium alloy and steel foams and slightly lower than alloy-polymer composite lattices. Therefore, coupling the excellent physics PEI properties with additive manufacturing is able to realize high performance cellular materials. Unluckily the interlayer delaminations limit the overall mechanical

performance yet.

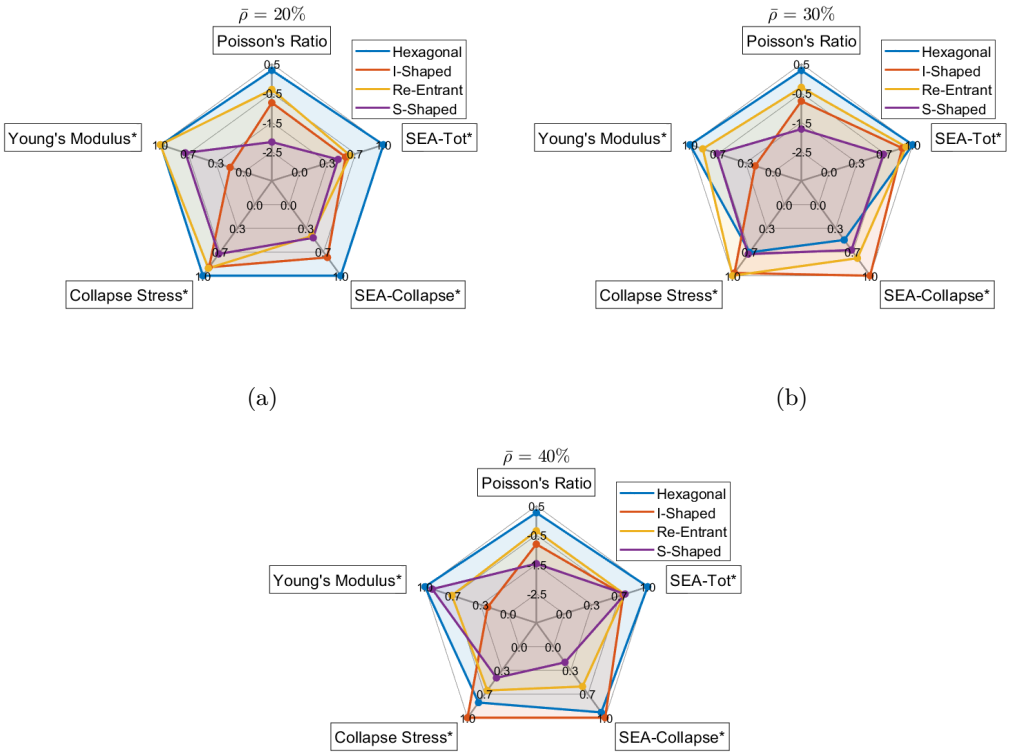

Figure 2.15: Spider-plots of PEI honeycombs overall performances. The mechanical properties are normalized to the higher values. The Poisson's ratio is not normalized. (a) PEI honeycombs with $\bar{\rho} = 20\%$. (b) PEI honeycombs with $\bar{\rho} = 30\%$. (c) PEI honeycombs with $\bar{\rho} = 40\%$.

Chapter 3

Finite Element Analysis

3.1 Introduction

In mechanics, it is necessary to take a real-life problem and put it in mathematical language. This process is known as modelling. Modelling enables a systematic understanding of the modelled system and gives a strategy for a problem solution. It also allows to control of the system and develop system improvements. In this study, the mechanical behaviour of PEI cellular materials is modelled by Finite Element (FE) analysis. The numerical simulations allow an understanding of how polymer mechanics, manufacturing process and geometries affect the mechanical response of PEI cellular materials. Once the numerical results will be consistent with the experimental finding, comments and theories will be afforded in order to improve the mechanical performances of the 3D printed structures.

Numerical simulation applied to 3D-printed parts is challenging. It has to take into account several variables such as the material mechanics, the material properties changing during the extrusion process, the deposition patterns, the geometries, defects, inclusions, and so on. Focussing on numerical models able to describe the mechanical behaviour of components printed by FFF, in literature, there are extensive studies based on the micro, meso, and macro scales [80]. However, all numerical models are always applied to specific cases. The most common study is the mechanical response investigation of a dogbone under uniaxial tensile loading in the function of raster direction [81, 82]. The printed part mechanics is quite similar to a fibre-reinforced material, it exhibits different strengths in tensile, shear and compression conditions. Moreover, the deposition strategy enables preferential failures along the raster directions, commonly called interlayer delaminations. The study of mechanical performances is addressed also on a micro-scale. The voids generated by the manufacturing process are detected by Computed Tomography (CT) analysis. Then, the effects of the void are taken into account by modelling the mesoscale removing solid part associated with the voids [83, 84].

The failure modes based on fibre composite materials criteria are usually defined in these studies, e.g. Tsai-Hill, Tsai-Wu, Puck, or Hashin. However, the solid part in cellular materials printed by FFF technology is thin and the number of filaments inside is low. That means the scale where the composite material failure criteria are

applied is not correct. Each failure postulate is based upon the symmetry properties having any macroscopically homogeneous material form [85]. For example in PEI hexagonal honeycomb with $\bar{\rho} = 40\%$ the cell walls are made up of 3 filaments; these ligaments have got material properties close to PEI solid materials but the failure can also happen along the interface between the extruded filaments. Otherwise, if the ligaments were made up of a high extruded path number, the solid part could be considered quite homogeneous and thus the composite failure criteria would result in suitable.

As it has been seen, the 3D printed structures exhibit different geometries, densities, and failure modes, i.e. inter-layer delamination, ductility and brittle failures. The unique common feature between the 12 honeycombs is the process parameters. Therefore, this study aims to propose a strategy able to predict the mechanical performances of cellular materials based on a multiscale material charaterization approach where the material has got the same manufacturing condition.

3.2 Mechanics and Mechanisms

The failure mechanism of 3D printed cellular material has to be looked for inside the nature of solid material. Polymer mechanics and fracture has been studied since the 1960's when the age of polymer began. The fracture mechanics of polymer is not completely clear as the metal one. The production of new polymers based on new artificial molecules is still in progress. However, the mechanics of the polymer are broadly established and it is associated with the polymer microstructure: amorphous, crystalline, semicrystalline thermoplastic polymer, thermosetting polymer or polymer fibre.

The PEI belongs to the glassy thermoplastic polymer family as well as the polymethylmethacrylate (PMMA), polystyrene (PS) and polycarbonate (PC). The mechanical response of a glassy polymer can be depicted by figure3.1. The characteristic stress-strain curve shows three regimes: an initial elastic stage, a nonlinear transition curve where a strain-softening behaviour appears and an ultimate strain-hardening stage[6]. In the elastic region, the material is stretched or compressed elastically or viscoelastically and the deformation is essentially recoverable. After the yielding point, the materials start to be deformed plastically but the deformation may not be permanent. Indeed, if a glassy polymer was heated to just above the glass transition, the deformation might be recovered. All glassy polymer exhibit the strain-softening stage but the softening slope and the minimum value before hardening is dependent on the polymer microstructure. This behaviour is due to a molecular chains slippage which starts to orient along the loading direction. Once all chains are oriented, the last strain-hardening phase begins. The polymer withstands loading up to a brittle failure or an extensive ductile deformation occurs.

As the characteristic stress-strain curve depicted, the deformation mechanism in the polymer is governed by a ductile deformation and a brittle failure. These two

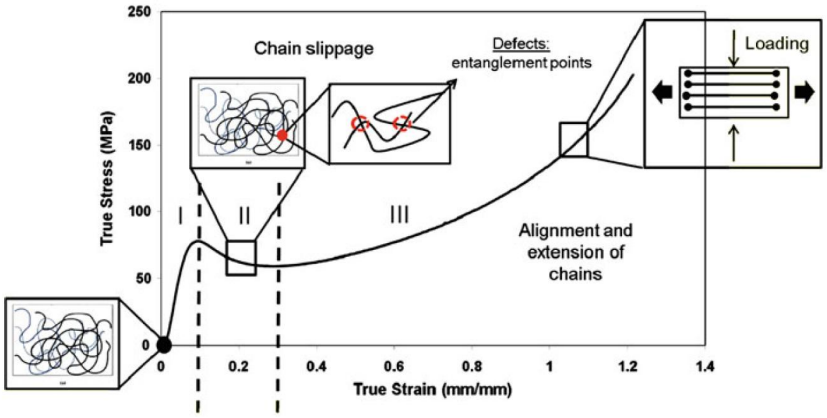

Figure 3.1: Response of an amorphous polymer under mechanical loading for temperatures below the glass transition temperature[6].

mechanisms can occur separately or complementary and they are called in literature shear yielding and crazing respectively. The former, responds primarily to pure shear stress as figure3.2a shown. It is a quasi-homogeneous distortional plasticity in which the polymers can undergo large permanent shape changes against an increasing deformation with negligible volume change. The latter, responding to a stress with a negative pressure component is a kind of planer dilatational localization, normal to the principal tensile stress, in zones of organized nano-scale fibrillation as figure3.2b shown. The crazing phenomena often terminates the distortional plastic response, resulting in brittle behavior[86].

In glassy thermoplastic materials, the chain orientation that governs the shear yielding phenomenon does not occur in a homogeneous manner; the plastic strain is localized in some local regions. That means a softening effect appears in these zones instantly. This inhomogeneous flow leads to a localisation of plastic strain and then the flow becomes unstable. In mechanics there are two reasons for this instability: the former arises from geometrical considerations such as the necking phenomenon. The latter is generated from the intrinsic material properties. Due to the inhomogeneous flow arising from a shear yielding deformation, the instability of the materials takes the form of shear bands[8].

Actually, the shear bands are not always comparable with the specimen scale. It should be noted that crazing and localised shear yielding are not mutually exclusive micromechanisms-in glassy polymers[8]. In literature, there is conclusive evidence that crazes and cracks can be initiated at the point of intersection of shear bands. Both may be observed simultaneously as the figure3.2c shown, and interactions occur between them. In the case of brittle fracture, crazing tends to be the predominant mechanism. Otherwise, the shear yielding may take place during crack propagation for both brittle and ductile fractures in glassy thermoplastics.

Once the physics behind the glassy polymer deformation has been explained, criteria to determine which phenomena occur phenomena are discussed. The first

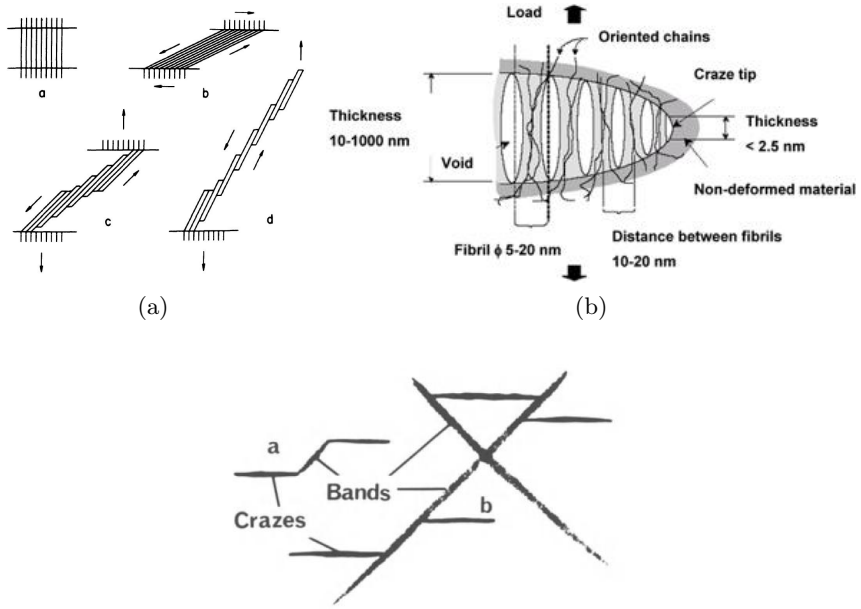

(a) (b)

(c)

Figure 3.2: Fracture mechanisms on glassy thermoplastic polymers. (a) Schematic drawing of the formation of fibrous sheets during tensile fracture of a coarse microshear band (after Chau and Li [7]). (b) Schematic drawing of the craze tip[8]. (c) Interactions of crazes and microshear bands in PMMA and polycarbonate as suggested by Jacoby and Cramer[9].

criterion is referred to as the crazing phenomenon. Crazing is usually initiated close to imperfections, defects, inclusions, and scratches. The craze formation is a dilational process so the hydrostatic pressure plays a fundamental role in craze initiation, propagation and breakdown. A positive hydrostatic pressure aids crazes propagation. Otherwise, the crazes are retard by hydrostatic compression. Therefore, Sternstein and Ongchin propose a phenomenological crazing criterion which takes into account the first invariant of spherical stress tensor [10].

$$\sigma_C = |\sigma_1 - \sigma_2| = A_1 + \frac{B_1}{\sigma_1 + \sigma_2 + \sigma_3} = A_1 + \frac{B_1}{I_1} \tag{3.1}$$

where A_1 and B_1 are temperature and strain rate dependent material parameters [10, 87].

However, the physical interpretation of this empirical relationship was not clear. Several researchers questioned and criticized that evaluation of σ_C for a general triaxial state of stress is difficult. Among them, Bowden and Oxborough found that the same relationship could be rewritten in terms of principal strains[88]. Thus, the critical values to obtain craze initiation in polymers were fitted following the equation:

$$\varepsilon_C = X_1 + \frac{Y_1}{I_1} = X_2 + \frac{Y_2}{\eta} \tag{3.2}$$

where X_1 and Y_1 are temperature and strain rate dependent material parameters[88, 87]. The equation can be further written in terms of triaxiality η.

A few years later, Bucknall demonstrated the crazes initiation criteria have origins in the plasticity theory. It was discovered simply by experimenting with von Mises' yield criterion for a ductile material under biaxial loading in which the yield is pressure dependent[89, 90].

The second criterion is referred to shear yielding phenomenon. Shear yielding obviously is dependent on maximum shear stress or maximum shear energy deformation inside the polymer. However, experimental findings showed true yield stress is invariably higher in uniaxial compression than in tension, and uniaxial-tensile tests conducted in a pressure chamber show that yield stresses of polymers increase significantly with hydrostatic pressure. So neither the Tresca nor the von Mises criterion adequately describes the shear yield behaviour of polymers. Firstly the Mohr-Coulomb yield criterion was used, subsequently, an octahedral stress criterion modified with hydrostatic component was used[89]:

$$\tau_{oct} = \tau^0_{oct} - \sqrt{\frac{2}{3}}\mu_m\sigma_m \tag{3.3}$$

A few years later, the Drucker-Prager yielding criterion was introduced. It is based on the assumption that the octahedral shear stress depends linearly on the octahedral normal stress through material constants [91, 92]. The Drucker-Prager criterion is generally expressed as follows

$$\sqrt{J_2} = A + BI_1 \tag{3.4}$$

In order to understand better the failure criteria in glassy polymers, it is considered a plane stress condition where competition between crazing and shear yielding occurs. The yielding initiation envelope is visualized on the principal stress plane in figure3.3. This visualization is able to confirm the crazing does not occur in a compression state. In addition, it confirms the possibility to have a co-existing deformation mechanism where the stress state provides the circumstances to generate first crazing or shear yielding, also in terms of yielding criteria.

The tensile deformation of many glassy polymers can be considered to be a competition between crazing and shear yielding. If crazing dominates the behaviour the polymer is brittle whereas if bulk shear yielding occurs preferentially the polymer is generally ductile. Hence the fracture behaviour of glassy polymers is controlled by a competition between crazing and bulk shear yielding. The principal parameter to predict how much a glassy thermoplastic material tends to be ductile or fragile is the entanglements. The polymer entanglements are a physics characteristic and it quantifies how the molecules are connected or entangled. The entanglements are lower when the polymer is melted and increase as it gets solid. The molar mass is also an indicator of entanglement grade, i.e. higher the molar mass and the higher

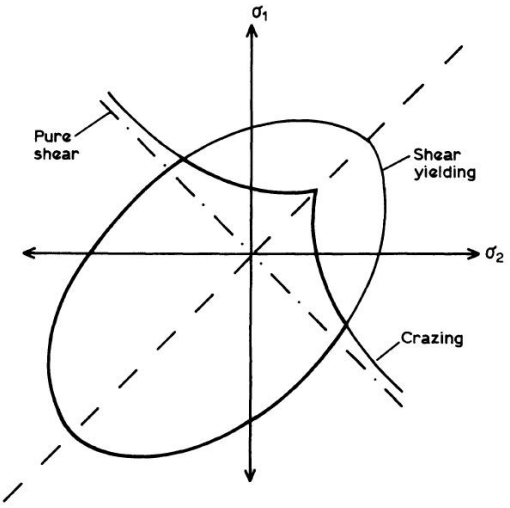

Figure 3.3: Comparison of envelopes for the initiation (Eq.3.1) of craze yielding and shear yielding (Eq.3.3) in glassy thermoplastic ploymers. Heavy continuous line indicates failure envelope(Stemstein and Ongchin) [10]).

the molecular entanglements. As polymer solutions become more concentrated (high molar mass) it is known that the molecules tend to become entangled rather than remain as isolated coils[8].

This parameter is extremely useful when a prediction for the ductile or brittle behaviour of a glassy polymer needs. For instance, from the entanglements evaluation, the preferential ductile behaviour of PC and PET is explained. Indeed, both of them undergo extensive shear yielding at ambient temperature. On the contrary, the PS and PMMA are generally brittle and more sensitive to crazing deformation[8].

PEI is a glassy thermoplastic material so the constitutive relationship to use in the numerical model must be coherent with polymer physics. The competition of shear yielding and crazing in PEI polymer is demonstrated by researchers such as Ikeda who investigates the triaxiality effects on yield stress and craze initiation[93].

3.3 PEI Constitutive Model

The PEI constitutive model was defined following the theory discussed in the previous section. The stress-strain curve should have got the characteristic shape as depicted in figure3.1, so the regimes are modelled as:

- The elastic stage is assumed to be described by isotropic linear elastic relationship; the main parameters are Young's modulus and Poisson's ratio.
- The yielding point is assumed to be affected by the hydrostatic stress state as physics dictated. In literature, Drucker-Prager yielding criteria are well established for soils, rocks, polymers and also composite materials. The model peculiarity is the possibility to model del yield surface in the meridional plane,

i.e. Von Mises - hydrostatic stress plane. The yield surface can have a different shape, Abaqus implements three shapes: linear, hyperbolic and general exponent forms.

- The plastic phase is assumed to have isotropic plastic behaviour with or without the utilization of an associated flow rule that overstates the extent and role of plastic dilatancy (Extended Drucker-Prager model in Abaqus takes into account dilatancy, more common in soil modelling). The stress-strain relationship exhibits a strain-softening behaviour and solvers like Abaqus accept only monotonically strain-hardening trends. In literature, the strain-softening behaviour is commonly modelled manually. For instance, in Abaqus, the strain-softening regime can be defined by manipulating directly the constitutive model through Abaqus user-defined material[94]. The customized material examples integrate the flow stress from empirical rules or couple the flow stress with strain rate or introduce a constitutive model from the principle of virtual power. [95, 96, 97, 6]. Therefore, several researchers implement these models as Abaqus subroutines or commonly called UMAT or VUMAT for the implicit or explicit solver, respectively[98]. However, the Abaques user-defined material is necessary only when the strain-softening behaviour is relevant because some glassy thermoplastic polymers exhibit a low softening stress stage. Indeed, an exponential form of strain-hardening relationship in terms of true stress and true strain exhibits a softening trend in engineering stress strain curve [11, 87].

- The damage model is a challenge. First of all, the damage can occur under extended ductile deformation (shear yielding) or under sudden brittle failure (crazing). Secondly, crazing is dependent on several environmental conditions, as illustrated in the previous section. However, both mechanisms are dominated by hydrostatic pressure and thus by triaxiality. Following the crazing criteria equation3.2 damage based on triaxiality and critical strain can be imposed under that form. In literature, damage based on triaxiality is well-established and it is called ductile damage relationship [99, 100, 101, 102]. This strategy is able to avoid failure under a compression stress state (crazing does not occur and shear yielding does not generate failure). A shear stress limit can be imposed following the shear yielding theory, as figure3.3 shows. In the end, crazing failure can be defined as a specific critical strain function of positive triaxiality. If the failure strain was comparable with the failure at pure shear, the shear yielding will be the dominating failure mode.

- The damage evolution could be defined as a function that runs from 1 (undamaged) to 0 (damaged) or as a function of releasing energy. The main problems to model damage evolution are connected with the crazing damage. The damage mechanism is complicated to be evaluated as Li et al. demonstrated [103].

However, the crazing failure evolves quite instantly (brittle failure). This damage evolution is evaluated in terms of energy released and it will be evaluated by experimental results

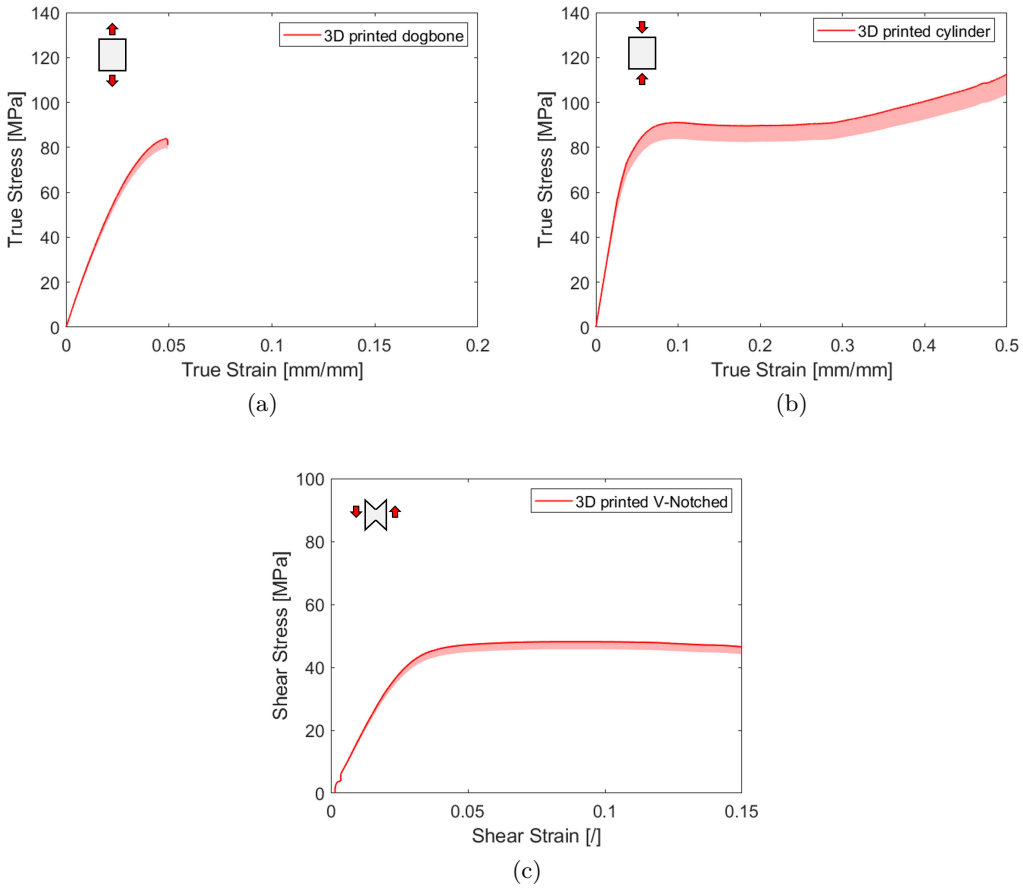

Figure 3.4: Charaterization of 3D printed PEI. Shadow areas describe repeatability range. The red lines are the highest curves obtained. (a) Results of tensile test on dogbone ASTM D638. (b) Results of compression tests on cylinderical specimens. (c) Results of shear tests on V-Notched specimens.

The constitutive model was defined by experimental observations. The scientific community does not give standard rules for testing 3D-printed FFF polymers so a traditional method based on standard rules for polymers was used. This study, was focused on the material properties of 3D printed PEI, thus only one printing direction was evaluated, i.e. load along to the printing direction. The first reason is connected to the solid distribution in cellular material. The additive manufacturing process follows the honeycomb shapes stacking the filament always in the same location. The material properties are dependent on the extrusion direction but it is not macroscopically constant because of the honeycomb shape. Thus, it is assumed the deposited PEI have isotropic properties. The second reason is connected with

the material properties looked for. Testing the 3D printed PEI component normal to the printing direction means evaluating the macroscopic transverse properties and not the deposited PEI because the failure occurs along the interfaces between the deposited filament.

Tensile, compression and shear test were performed and strains were measured through the DIC technique. The material characterization results are shown in figure3.4. The tensile tests were performed on 3 specimens with ASTM D638 shape. The raster direction is parallel to the tensile loading. The compression test was performed on 3 cylindrical specimens laid down on the building plate. Thus, the cylinder axis is parallel to the raster direction and also to the compression loading. The shear properties were evaluated through 3 shear tests on V-notched specimens. The printing direction is perpendicular to the shear force. In this way, the 3D-printed PEI shear properties are evaluated preventing inter-layer delamination failure. Red patches in figure3.4 depict the stress-strain curve range obtained with 3 reps. The thick red lines define the highest stress-strain curve obtained.

The 3D-printed PEI exhibits extensive ductile deformation under compression loading as well as shear deformation. The tensile test results show an extremely brittle fashion fail, i.e. the plastic strain to failure is about 3%. Evaluating these characterization results, PEI seems to exhibit a ductile behaviour (shear and compression loading) due to the shear yielding mechanism and a brittle failure (tensile loading) due to the crazing mechanism. This PEI behaviour is peculiar for glassy thermoplastic material and it is also confirmed by Ikeda studies [93]. Therefore, the PEI elastic properties were found. Young's modulus is 2246 MPa and Poisson's ratio is 0.3596. PEI polymer exhibits a yielding point sensitive to stress state, so the yielding point under tensile test is assumed to be around 64 MPa and under compression stress state around 72 MPa.

The Drucker-Prager yielding criterion was fitted exploiting the experimental results. The yield surface in the Drucker-Prager model is assumed to be linear and the material friction angle $\beta = 0.15$, i.e. the slope of the linear yield surface in the p–t stress plane. To control the dependence of the yield surface on the value of the intermediate principal stress the parameter K is introduced in Drucker-Prager, i.e. the ratio of the yield stress in triaxial tension to the yield stress in triaxial compression. It is assumed the $K = 1$ as the literature suggests. The ductile deformation is assumed to be connected with shear yielding, so the dilatancy phenomena are assumed ineffective. Thus, the dilation angle ψ is assumed to be equal to the friction angle. The ductile damage criterion is defined through experimental observations and polymer physics. The strain-hardening relationship is assumed to be consistent with compression behaviour and the stress-strain curve was imposed in the Drucker-Prager hardening section. The damage does not occur under shear and compression tests, so the fracture strain is assumed to function of only one variable, i.e. Y_2 in equation3.2. The fracture strain trend is shown in figure3.5. The fracture energy is calculated from the tensile test and it is assumed 0.001 due to the extremely brittle

failure. The 1st model of 3D printed PEI is denoted.

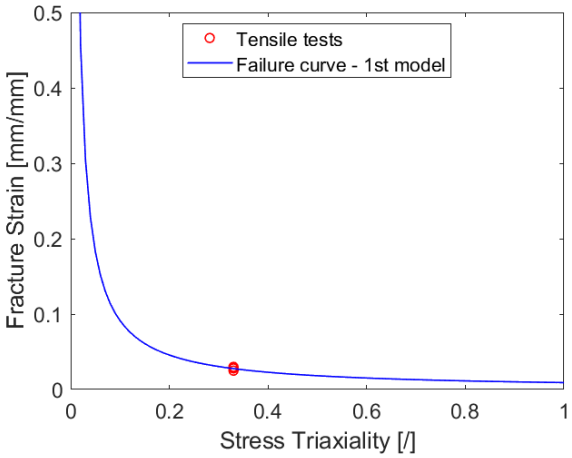

Figure 3.5: First definition of failure strain in function of triaxiality.

Before moving on to the numerical modelling of complex structures, the model was used to predict the mechanical performances of a 3D-printed PEI beam under a three-point flexure load. Verifying the model with Three-Point Bending (TPB) is not a random choice. The role of randomly distributed defects in TPB specimens is decisive, leading to a significant scattering in mechanical properties [104]. Indeed, the bent beam is stressed in tension (bottom side) and in compression (upper side) and the stress distribution inside the thickness provides fewer defects effects that affect mechanical properties. Moreover, geometric instabilities such as necking in the tensile test do not appear. The three-point bent beams were printed following the standard specimen rule ASTM D790 and the printing direction is parallel to the beam axis. The TPB test was modelled in the Abaqus environment. The TPB test is modelled imposing the plain strain on the beam cross-section. The beam width is about 12 times the thickness, these dimensions confirm the compatibility of plain-strain condition. The TPB test's numerical result is shown in figure3.6 and compared with the experimental ones.

Figure3.6 denotes the numerical and experimental results are not consistent. The first issue is connected with the strength reached by both TPB beams. The strength values are not comparable. It is well-known that 3D-printed specimens exhibit defects inside them because of the deposition process. However, the TPB test is lowlily affected by defects contribution for definition. That means the strain-hardening parameters are not valid to simulate bending behaviour. The second issue is connected with the failure to strain. The ultimate displacement is extremely lower in the numerical model than in the experimental one. That means the failure strain assumed is extremely low. Conversely, the linear elastic regime is consistent as well as the brittle damage evolution. In conclusion, the 3D-printed PEI properties should be higher and also the ductile behaviour should be more extended. In the literature,

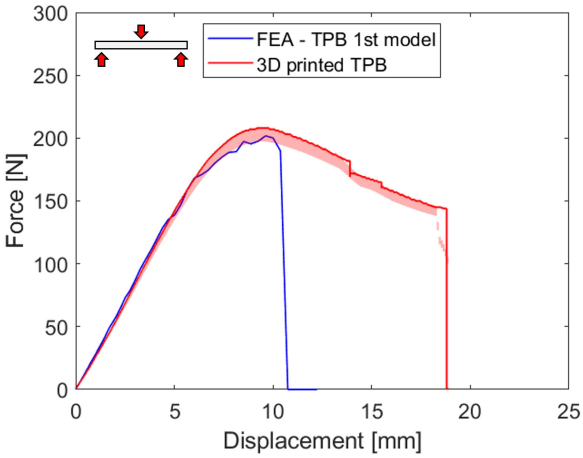

Figure 3.6: Comparison between the experimental test and numerical results of TPB specimens.

there is none that simulated the 3D-printed PEI. The numerical models proposed by Garriga and Auricchio predict only the linear elastic relationship [61, 44]. In addition, studies on FFF printed parts are usually focussed on quantifying the defects contribution or printing parameters on linear mechanical properties from micro to macro scale[105]. The plasticity of FFF parts is not commonly addressed. Rare papers in this field take advantage of material properties prediction based on DigiMat software[106]. This software is able to predict locally the change in properties due to the manufacturing process and then apply them to the numerical model. Therefore, in this study, an innovative strategy to evaluate the real mechanical properties of glassy thermoplastic materials is introduced.

This theory base the statement on the peculiarity of glassy thermoplastic materials. Unlike semicrystalline polymers, the mechanical properties of glassy thermoplastics are not strongly dependent upon fabrication conditions or variations between different batches and this makes it possible to correlate the results of different groups of workers[8]. Indeed, a crystalline polymer like PEEK is strongly dependent on an additive manufacturing process as Wang shows in his study[107]. Therefore, the material properties of 3D-printed PEI should be similar to the filament ones.

A piece of filament PEI was cut and tested under tensile loading. Figure 3.7 shows the stress-strain curves of PEI filaments. The blue line is the engineering stress-strain curve obtained from the tensile test on the filament. As expected, the material exhibits a strong strain-softening behaviour due to the predominant shear yielding deformation[108]. However, the softening behaviour is generated by a coexistence of geometric instability (necking) and constitutive instability (chain rearrangement). This is visible in figure3.8a (located in "a" in figure3.7), where the filament exhibits the necking shape without breaking. The specimen cross section decreases instantly once the yielding point is reached; necking instability. The necking instability locally generates the chain rearrangement because the stress-strain

polymer curve exhibits a strain-softening stage. Thus, the material properties close to the neck region required higher stresses to overtake the yielding point. This constitutive instability coupled with geometric instability (necking) generates a stable cross-section as the displacement increases[8]. The deformed shape propagates along the specimens axys[109]. A deeper discussion about this phenomenon is addressed by G'Sell [11].

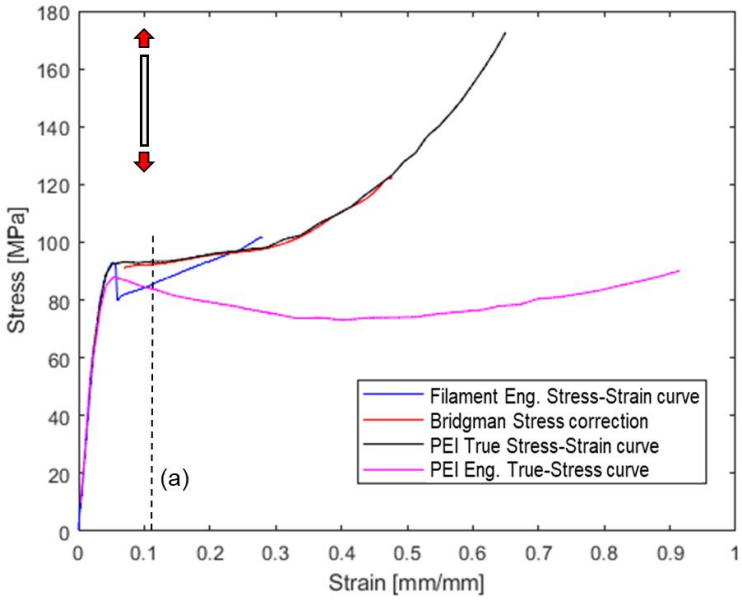

Figure 3.7: Results of tensile test on PEI filament.

The blue line in figure3.7 can not coincide with the PEI filament properties because a geometric instability occured. Bridgman explained deeply how obtain the effective stress from a neck shape[110]. In detail Bridgman defines a stress correction based on necking curvature as follows

$$\sigma_{eff} = \frac{1}{1+\frac{2R}{a}} \ln\left(1+\frac{a}{2R}\right)\sigma_x \tag{3.5}$$

where $\frac{1}{R} = \frac{\partial^2 a}{\partial x^2}$, R is the radius of curvature and a is the filament diameter. Both σ_x and σ_{eff} are tensile stress along the filament axis. σ_x is the tensile stress of a cylindrical profile and corresponds to the tensile stress of the monaxial stress state. σ_{eff} is the tensile stress of a concave or convex profile and corresponds to a multiaxial stress state. The figure3.8b explains better the stress state. In this study, the convex and concave filament profile is obtained through image analysis of the neck-shaped filament as figure3.8a shows. The evolution of filament diameter was calculated by the filament profile, red line in figure3.8a. Then, the σ_{eff} stress was obtained through the equation3.5 and it coincides with the true stress of PEI material.

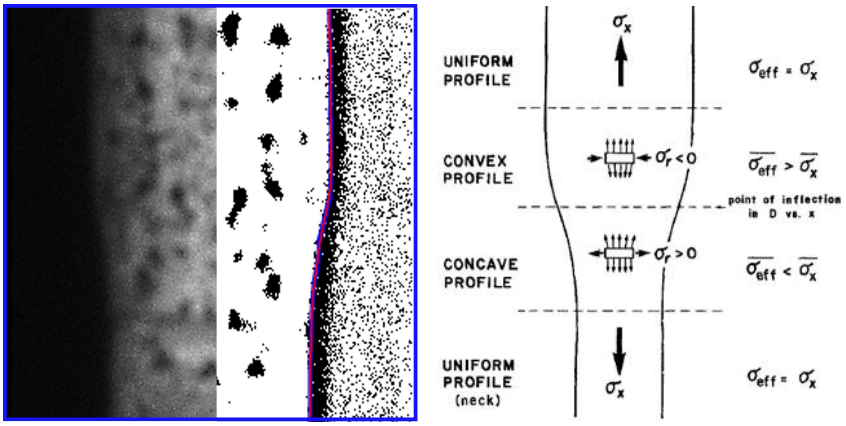

(a) (b)

Figure 3.8: Neck propagation during the tensile stretching of solid polymers. (a) Defining the filament profile through image analysis. (b) Schematic representation of the transverse stresses generated in a sample of varying cross-section. Note that $\sigma_{eff} < \sigma_x$ in regions of negative curvature[11].

The true strain is calculated following the ratio of cross section area:

$$\varepsilon = ln\left(\frac{A_0}{A}\right) \tag{3.6}$$

where A_0 is the initial cross-section area and A is the instantaneous cross-section area [111]. Applying both true stress and true strain correction, it is possible to obtain the true stress-strain curve of PEI material. For instance, the red line in figure3.7 corresponds to the true stress-strain curve of PEI obtained from the neck shape in figure3.8a. Applying these corrections in all test images can be populated the overall true stress-strain relationship, i.e. black line in figure3.7. In the end, the real engineering stress-strain curve is obtained, i.e. a magenta curve in figure3.7. As expected, the stress-strain relationship is composed of the traditional three stages: linear elastic, strain-softening and strain-hardening phases. Once the necking propagated along the entire filament, the specimen is unloaded and then reloaded on the stretched zone. The molecular chains were well oriented to the loading direction and the filament failure occurred extremely brittle at true strain $\varepsilon = 0.65$. Young's modulus of PEI filament is 2281 MPa.

The tensile test on filament demonstrates the tensile properties of PEI could be extremely relevant, it can reach up to 65% of deformation with a strength of about 175 MPa. However, the 3D-printed specimens do not exhibit so much higher failure strain. Although glassy thermoplastics are not strongly dependent upon fabrication conditions, changes in mechanics performances are mandatory.

Experimental tests exhibit an extremely brittle failure under tensile loadings. That means, the crazing phenomena could be the preferential failure mechanism in 3D printed PEI under tensile loading, e.g. the yielding surface could have a shape

similar to the one in figure3.3. This statement is firstly confirmed by the crazes initiation nature. Crazes are generally nucleated at imperfections in polymer specimens such as surface flaws, dust particles, defects, scratches, and so on. It is well-known that the additive manufacturing process generates imperfections, so the 3D-printed PEI could be more sensitive to brittle failure due to crazing.

This statement is secondly confirmed by physics. In detail, Turner demonstrated that there is a relationship between fracture strength and molar mass, and, thus, a relationship between fracture strength and polymer entanglements in turn [112]. The relation is inspired by the Flory equation and it takes the form as follows

$$\sigma_f = \sigma_{g\infty} - \frac{B_s}{M} \tag{3.7}$$

The parameters are the strength of a polymer with infinite molar mass, i.e. σ_f, and material constant, i.e. B_s. This relationship dictates that entanglements play a vital role in controlling the fracture behaviour of glassy thermoplastics through their effect upon crazing and shear yielding. Donald and Kramer demonstrated that crazing strength is extremely more sensible to molar mass or entanglements than shear yielding although both mechanisms follow the equation3.7 [113, 114]. The molar mass or the entanglements are dependent on the polymer glass transition in turn, as the Fox-Flory equation dictates

$$T_g = T_{g\infty} - \frac{A}{M} \tag{3.8}$$

Novikov et al. demonstrated the Fox-Flory relationship for glassy thermoplastic polymers[12]. Novikov changed the glass transition temperature of several polymers, as figure3.9 shows, thanks to predefined thermal cycles. He measured the resultant entanglements for several glassy thermoplastic materials and he found an empirical relationship: $T_g \propto M^{\frac{2}{3}}$.

It is well established the glassy polymer T_g is sensible to thermal cycles. Because FFF technology is basically a thermal cycle: heating, extruding and then cooling, the T_g could be affected by the additive manufacturing process. Therefore, the glass transition temperatures were analyzed before and after the additive manufacturing process. The glass transition temperatures were measured through Differential Scanning Calorimetry (DSC) analysis. The T_g were determined by the midpoint between extrapolated heat flow[115] as the figure3.10 depicts. T_g were analyzed in three different pieces: one belongs to the PEI filament (before printing), one belongs to the 3D printed dogbone(after printing), and one belongs to the re-entrant structures with $\bar{\rho} = 20\%$ (after printing).

The DSC analysis shows the T_g of PEI filament is about $181.2°C$ and this value is consistent with T_g of Ultem 9085. The T_g in 3D printed specimens could be considered similar, i.e. $177°C$. Therefore, the T_g after the printing decreased by about 3%. Following the previous equations, it could be supposed the molar mass

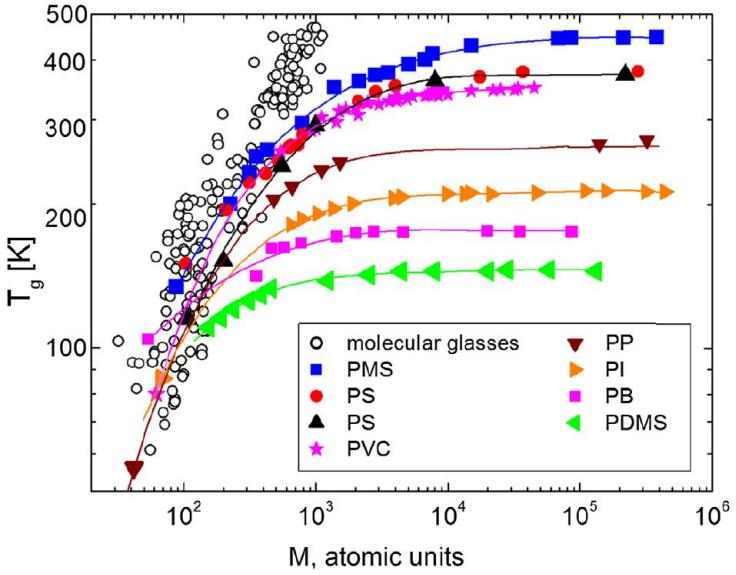

Figure 3.9: Comparison of glass transition temperature T_g vs molecular mass M of glassy thermoplastic polymers [12].

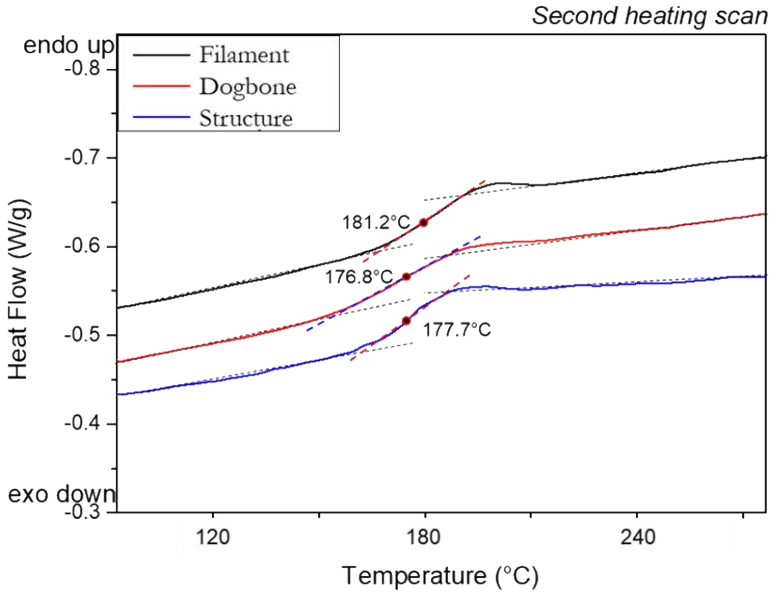

Figure 3.10: Results of Differential Scanning Calorimetry (DSC) analysis carried out on PEI filament, 3D printed PEI dogbone and 3D printed PEI re-entrant honeycomb.

or entanglements decreases after the additive manufacturing process. Consequently, also the fracture strength should be decreased.

Therefore, it might suppose the crazing mechanism sensibility is increased after the additive manufacturing process through two key factors: imperfections and

changes in microstructure. Imperfections are generated by the deposition strategy of FFF technology. Change in microstructure (T_g, molar mass, entanglements) is generated by the intrinsic extruding process of FFF technology, i.e. filament melting, extruding and cooling. A graphical representation of this statement is illustrated by the figure3.11. The crazing yielding criteria might move towards the chart's central part after the printing process.

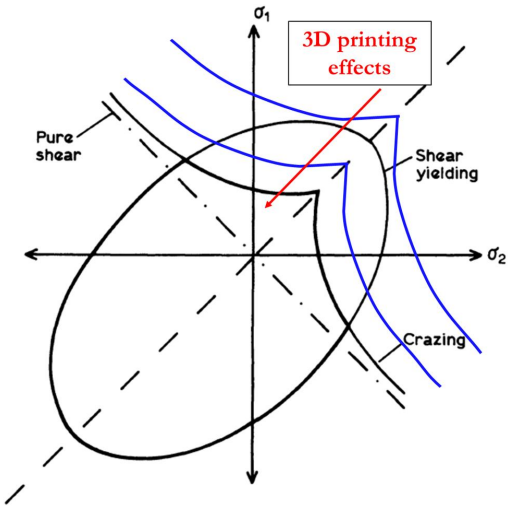

Figure 3.11: Conceptualization of additive manifacturing effect on crazing and shear yielding criteria envelopes.

A second constitutive model of 3D printeD PEI is proposed following the previous statement. Changes in fracture strength involve changes in failure strain. The resulting failure strain trends are governed by the equation3.2. In order to define this trend an optimization procedure was implemented. The procedure is depicted in figure3.12a. The X_2 and Y_2 parameters were determined by minimizing a function cost. This function is defined as the Normalized Root Mean Square Deviation (NRMSD) between the numerical and experimental ultimate strain in the tensile test and ultimate displacement in the TPB test. In Abaqus, models used the PEI true stress-strain curves resulting from the PEI filament characterisation. The minimization procedure was carried out through Matlab code in which the Abaqus simulation was run in batches. Figure3.12b illustrated the practical meaning of this procedure. The minimization procedure looked for the new failure strain along to the true stress-strain curve of the PEI filament.

The calibration results in terms of failure strain trend in the function of triaxiality were shown by the figure3.13. The blue line is the first model relationship whereas the red line is the second model relationship proposed, i.e. the calibrated failure strain. The coloured circles are associated with the experimental failure strain measured except for the blue circles. The predicted failure strains are higher than the measured ones. That involves an increase in the ductility behaviour of 3D-printed PEI. The red lines moved up to a monoaxial tensile failure strain about $\varepsilon = 0.24$

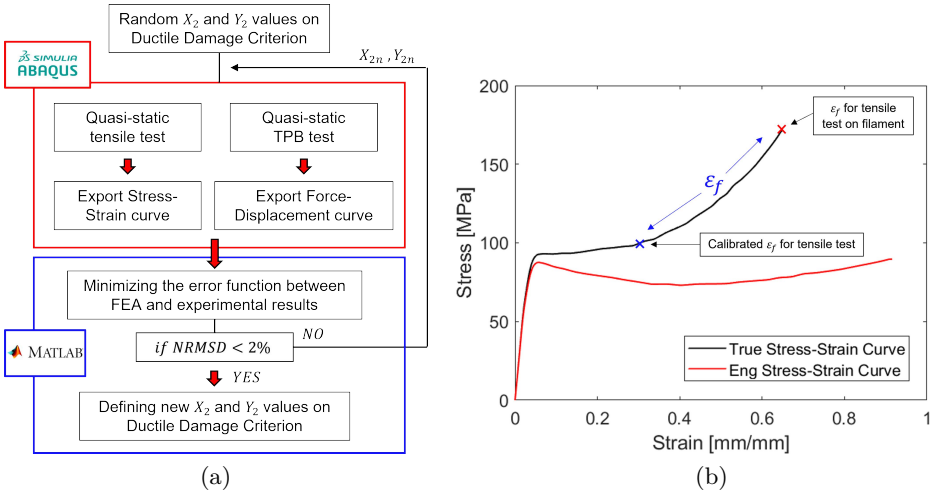

Figure 3.12: Strategy to define failure criteria X_2 and Y_2 parameters. (a) Conceptual maps behind the calibration of ductile damage criterion. (b) Visualization of failure strain decreases after the calibration procedure[13].

versus the measured $\varepsilon = 0.03$.

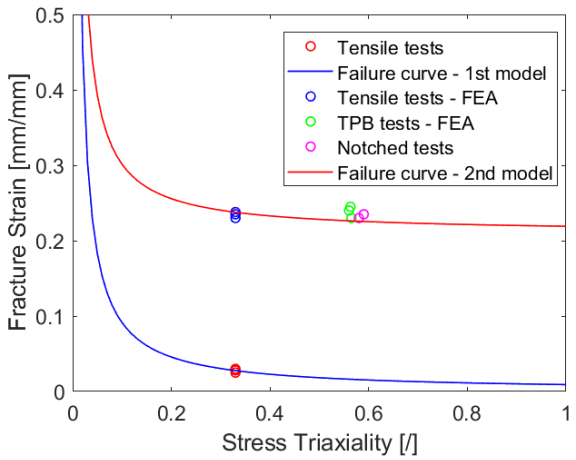

Figure 3.13: Updated ductile damage criterion after the parameters calibration.

The numerical results of the TPB test are shown in figure3.14. The FEA result fixed the previous issues on ultimate strength and ultimate displacement. The lower defects sensitivity of the TPB test confirms the new true stress-strain curve well suits the real behaviour of 3D-printed PEI. Consequently, this result confirms the mechanical properties of PEI filament are similar to the 3D printed one. After the maximum loads, the numerical models exhibit stiffer behaviour than the experimental ones. Defects interaction coupled with the plasticity mechanism occurs in this stage so the numerical curve can not completely describe the force trend.

However, the result on calibrated failure strain for monoaxial stress state seems unreal. In figure3.13, the red circles represent the failure strain in experimental

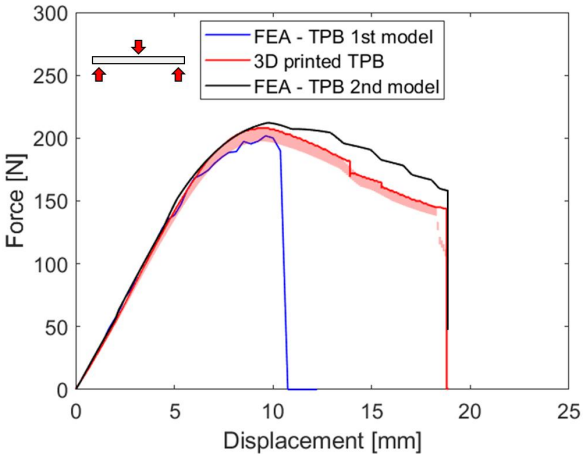

Figure 3.14: Comparison between the experimental test and the updated numerical results of TPB specimens.

tests whereas the blue circles are the predicted failure strain imposed in the constitutive model in Abaqus. The predicted failure strain is about 8 times the measured one. The explanation has to be looked for inside the FEA model. The monoaxial stress test was modelled to impose symmetry along the loading axis and impose plane stress conditions due to the thickness being extremely lower than the width. Once the yielding point is reached, the numerical model predicted the necking phenomena (geometric instability). However, the PEI stress-strain curve exhibits strain-softening behaviour (constitutive instability). The coexistence of these two phenomena creates shear bands as figure **??**a shows. The stable cross-section can not be reached because the localized failure strain overtakes the failure strain. If the failure strain was higher or similar to the PEI filament, the stable neck region should be extended along the specimen's axis as the PEI filament occurred. The localization of the shear band was compared with the specimen fracture as figure3.15b shows. The broken specimen exhibits failure compatible with the numerical prediction. The location of this failure under tensile test is also common in other studies on 3D printed thermoplastic materials [116, 117]. In the end, the shear band formation justifies the jump in failure strain. DIC should have measured this strain in the experimental test but the phenomenon occurred too instantly.

The results in terms of the stress-strain curve are also depicted in figure3.16b. The numerical result exhibits a lower strength than the PEI filament but it is dependent on the specimen shape; the filament is cylindrical whereas the dogbone is rectangular. Indeed only the plastic region was affected by the specimen shape[118]. At first sight, the experimental results do not suit the numerical ones. The ultimate strength in FEA is higher than the experimental test. However, the stress was calculated with the external cross-section of the dogbone; the effective area was lower due to the imperfections inside it. Figure3.16a shows the Computed Tomography (CT) analysis carried out on the strengthest 3D printed dogbone [119]. ZEISS Metrotom

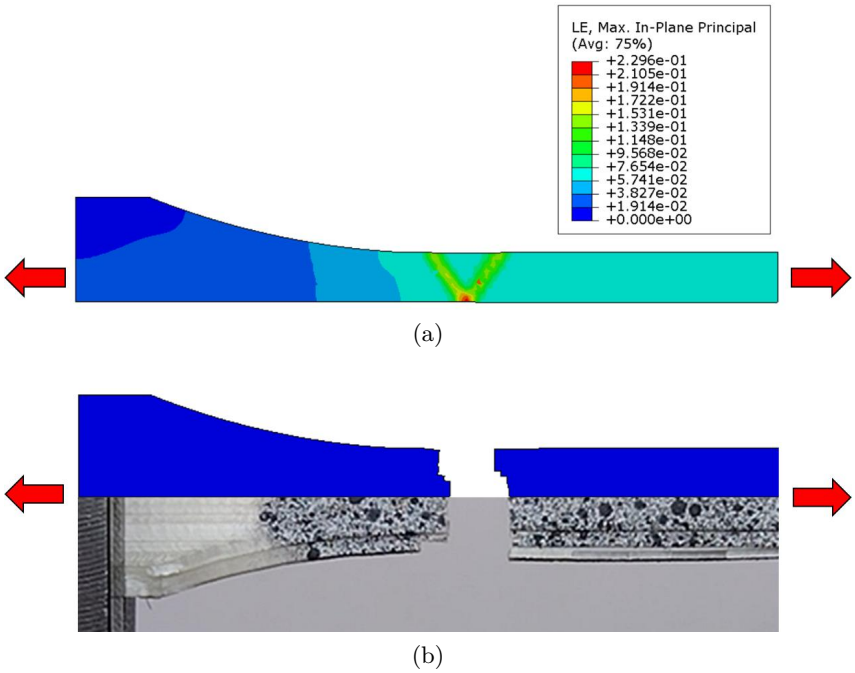

(a)

(b)

Figure 3.15: Failure of 3D printed PEI dogbone under tensile stress. (a) Shear band predicted by FEA. (b) Comparison between the experimental and numerical dogbone fail.

CT is able to visualize imperfection with a minimum voxel dimension of 13.87μ mm. The effective area was computed by multiplying the material zones (black pixel) by the voxel dimensions. The imperfections were computed as the ratio between the effective area to the dogbone envelope. The imperfections are white pixels (air) and they are located along the interfaces between the deposited filaments. The voids percentage is 3.46%. The stress-strain curves should be computed on the effective area thus the measured stress-strain curves were multiplied taking into account the decreased area. The updated curves are consistent with the numerical predictions.

In the end, further FE analyses were carried out to demonstrate the consistency with experimental tests, as shown in figure3.17. The numerical prediction is always higher than the experimental one due to the imperfections or porosity inside the specimens. Furthermore, 3 notched specimens were tested to confirm the model's effectiveness. The ultimate failure strain measure through DIC was depicted by green circles in figure3.13. Both experimental results are consistent with numerical predictions. The updated constitutive material model was used to model the solid part of 3D-printed honeycombs.

3.4 Numerical modeling of cellular materials

The numerical modelling of cellular materials follows a scale-based approach. Usually, three scales are defined in the function of characteristic length:

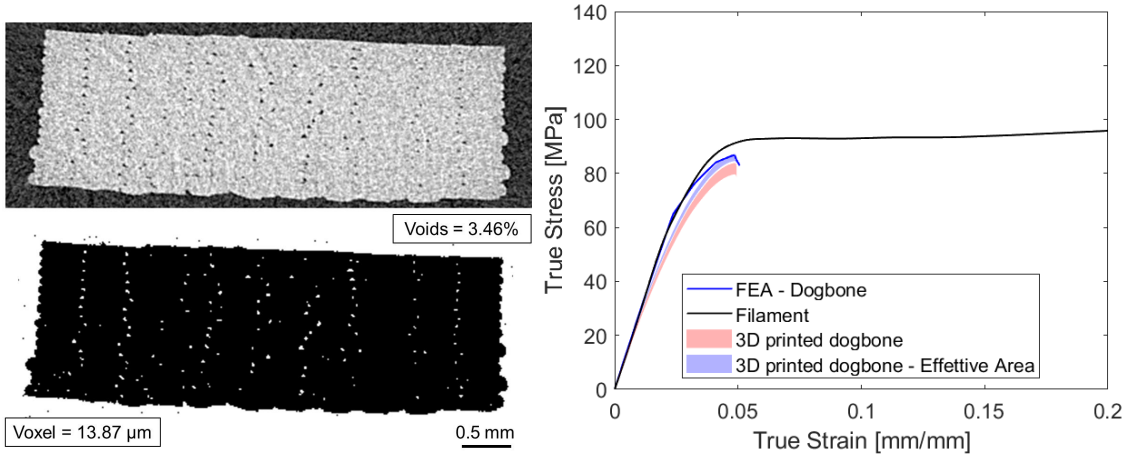

(a) (b)

Figure 3.16: Imperfections inside the 3D PEI printed dogbone. (a) Voids distribuion inside the specimen through tomography scanning and image analysis post-processing. (b) PEI tensile properties taking into account the effective area.

- $\mathscr{L}^m$: the characteristic length is associated with the microscopic features (e.g. grains, molecular chains, reinforcements). It can equivalently be at nanometer-,micrometer-, millimeter-, or meter-scale;
- $\mathscr{L}^{RVE}$: the characteristic length is associated with a Representative Volume Element (RVE). RVE is a material volume whose effective behaviour is representative of that of the material as a whole[120]. RVE is a statistically homogeneous material when the cellular materials belong to the foams or sponge family. Otherwise, RVE is a unit-cell topology material when the cellular materials belong to the architected cellular materials family. Consequently, the RVE can be defined in two-dimensional space or in three-dimensional space;
- $\mathscr{L}^M$: the characteristic length is associated with macroscopic features.

The key condition of separation is: $\mathscr{L}^m < \mathscr{L}^{RVE} < \mathscr{L}^M$ [121].

In this study, the mechanical performance of 3D printed PEI honeycombs are evaluated through traditional macroscale, e.g entire honeycomb, and through RVE scale, e.g. unit-cell topology. The honeycomb solid materials are modelled imposing the 3D printed PEI mechanical properties from the previous material characterisation (traditional approach). Therefore, the results of a hypothetical microscale approach should have the same results as material characterization.

3.4.1 Finite Element Analysis on Representive Volume Element

The PEI cellular materials belong to the honeycomb family, so the unit-cell topology is articulated in two-dimensional space. The RVE of each honeycomb coincides

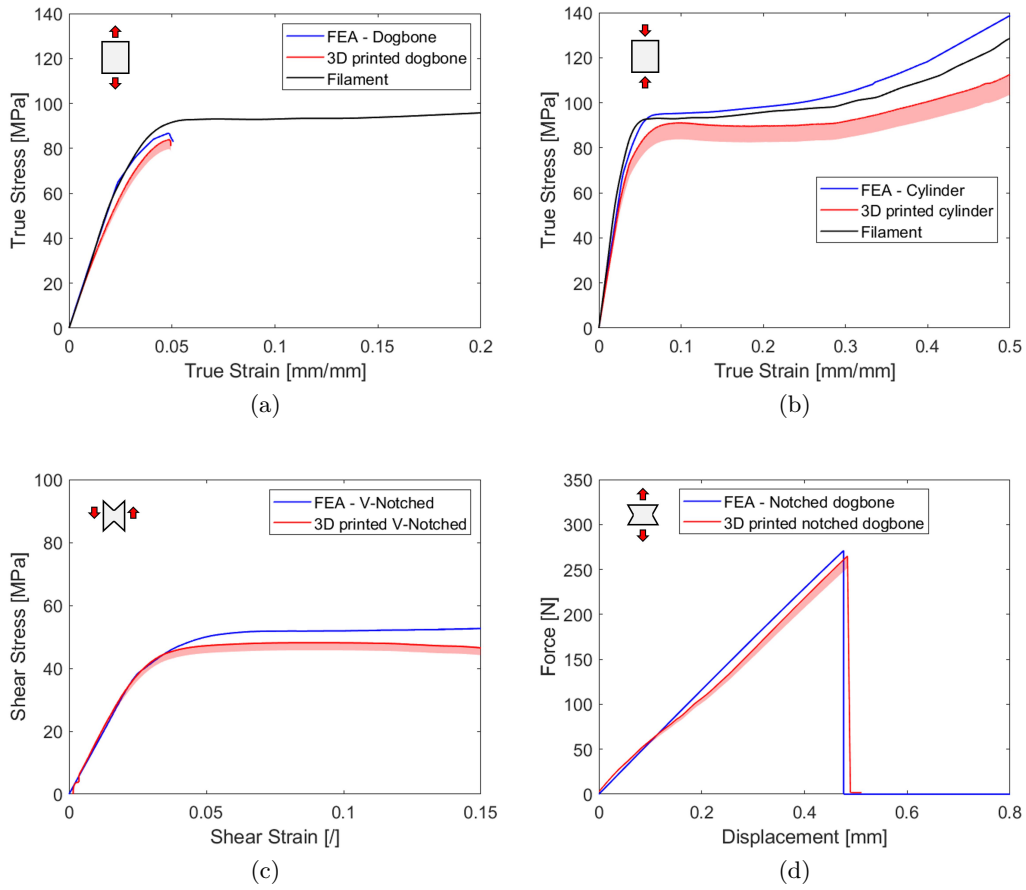

Figure 3.17: FEA with updated consitutive PEI model on tensile, compression, shear and triaxial stress tests. (a) Results of tensile test on dogbone ASTM D638. (b) Results of compression tests on cylinderical specimens. (c) Results of shear tests on V-Notched specimens. (d) Results of tensile test on notched specimens.

with its own unit cell. However, the loading condition that governs the unit-cell deformation must be imposed correctly. The boundary conditions to impose on the RVE system must follow the Periodic Boundary Condition theory. The PBC entails the simulation of a structure as an infinite system with all pairs of opposing boundaries deforming in an identical manner, ensuring the geometry of the system remains periodic throughout deformation. PBC avoids all edge effects and contiguous RVE interactions. PBC conditions coupled with RVE theory enable the investigation of the mechanical properties of the system when the overall cellular materials are composed of a high number of unit-cell. In this study, 4x4 fashion guarantees the applicability of this numerical modelling strategy.

In literature, there are several methods to ensure the unit-cell boundaries deform in an identical manner under external loading [14]. One of the most commonly employed methods in FE analysis is to use fixes and strains to constrain the simulated

cell to retain its original shape. The method is quickly depicted in figure3.18a. The unit-cell is modelled as a system with a rectangular envelope and it is simply supported from the nodes at one of the horizontal and vertical edges of the cell. The external loading is applied along the needed direction imposing the external nodes remaining horizontal or vertical based on the loading direction. The remaining edges are coupled in order to ensure that they remain straight. The limitation of this method is the hypothesis to retain the original unit-cell shape. For example, a buckling phenomenon along the boundary condition is wrongly neglected.

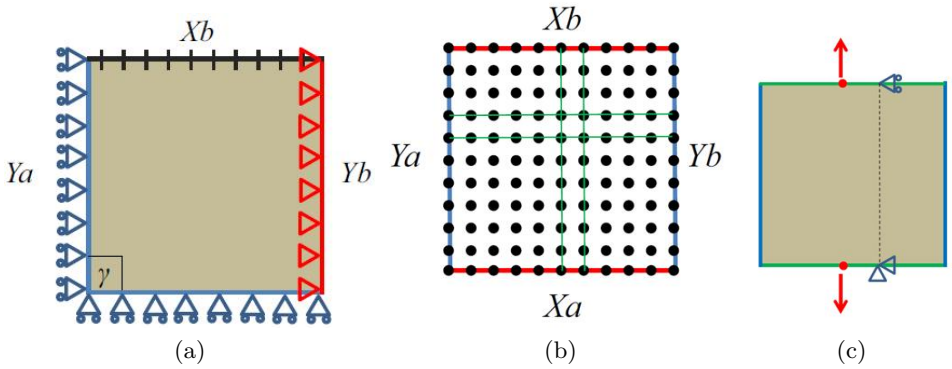

Figure 3.18: Implementing Periodic Boundary Conditions. (a) Sketch of nodes connections inside unit-cell with common PBC[14]. (a) Sketch of nodes connections inside unit-cell with advanced PBC[14]. (c) Sketch of loading application with advanced PBC[14].

Mizzi et al. proposed an alternative and advanced PBC implementation method through the use of constraint equations. Constraint equations are used to force the displacement of the nodes on one boundary onto the corresponding nodes on the opposite periodic boundary, as figure3.18b shows. This method does not enforce the edge nodes to retain their original alignment with adjacent nodes[14]. This advanced PBC implementation method requires a governing node pair for each direction, i.e. x, y, and z. All other nodes are coupled with the governing nodes imposing that the number and position of nodes on opposing periodic boundaries are identical. The constraint equations for the displacements of every boundaries node in the x-y plane are formulated in the following manner (governing nodes 1 and 3):

$$\begin{aligned} UX1 - UX3 &= UX2 - UX4 \qquad & UY1 - UY3 &= UY2 - UY4 \\ UX1 - UX3 &= UX5 - UX6 \qquad & UY1 - UY3 &= UY5 - UY6 \\ UX1 - UX3 &= UX(N_l) - UX(N_r) \qquad & UY1 - UY3 &= UY(N_l) - UY(N_r) \end{aligned} \tag{3.9}$$

The rigid body motion of the system is avoided ensuring the system remains aligned with either the x- or y-axis during deformation. The loading condition is imposed through the application of a force or displacement normal to the loading direction on the governing nodes belonging to the unit-cell edges, as figure3.18c shows. Mizzi

et al. confirmed the limitations of implementing PBC with the first method to calculate the mechanical properties of auxetic honeycombs [14]. The advanced PBC implementation method was used to impose the PBC in this study.

The unit-cells topologies were imported from nTopology to Abaqus software as planar deformable parts. The 3D-printed PEI material properties were imposed on the solid part. Contact interactions were imposed along the normal and tangential directions. Contact interactions guarantee sliding with friction properties based on a penalty factor (0.1) and allow the separation after a compression loading (hard contact). The PBC conditions are imposed manually by writing the equations constraint directly in the .inp file through the Matlab routine. The PBC conditions appear in Abaqus inside the section "interactions". In the beginning, the Abaqus implicit solver was used to simulate the compressive unit-cell behaviour. However, the explicit solver turned out to be more robust in case of failure or contact interactions. 4-node elements with plain strain formulation were used with the smallest mesh size of about 0.1 mm in order to have a stable time increment of 10^{-7}. Loading conditions were applied in 10 s to avoid dynamics phenomena during the compression. The compression loading step was anticipated by the buckling analysis step. Thus, the unit-cells were compressed from their own buckle shapes in order to predict the geometric unit-cell instabilities.

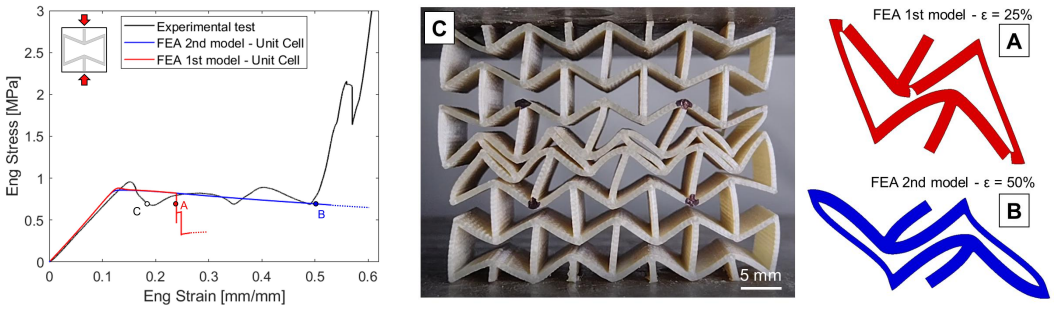

(a) (b)

Figure 3.19: Comparison between the experimental result and RVE analys of Re-Entrant $\rho = 20\%$ compressive behaviour. The FEA results are obtained using the 1st (red) or 2nd (blue) constitutive model. (a) Comparing mechanical properties. (b) Comparing the deformed shapes at A and B strain levels.

The numerical model based on RVE analysis with PBC was applied to each unit-cells (UC) topology. The numerical results for re-entrant UC with $\bar{\rho} = 20\%$ were depicted in figure3.19. In this figure, the numerical simulation was carried out with the 1st and 2nd PEI constitutive models. The stress-strain curves were shown in figure3.19a. The black line corresponds to the experimental results whereas the blue and red lines correspond to numerical results with the 1st and 2nd PEI models, respectively. Both RVE analyses are consistent with the experimental in terms

of Young's modulus. The initial collapse stress is underestimated but consistent. However, the 1st model shows extremely brittle behaviour. This further confirms of 2nd model's effectiveness.

Once the stress-strain curve obtained in RVE analysis overtake a specific deformation value, the curve was plotted by a dotted line instead of a continuous one. The dotted line represents a false stress-strain relationship. At that specific value, the deformed shape should create new interaction inside itself. The RVE theory does not take into account new cell wall interaction. That means the RVE stress-strain curve has to be evaluated up to that strain value.

The deformed shapes at the same stress level were depicted in figure3.19b. The deformed shape at the B stage is consistent with the compressed layer in the experimental test, C stage. Both deformed shapes exhibit buckling phenomena with subsequent compaction without reaching failures. The deformed shapes are zoomed in figure3.20. The numerical analysis predicted a triangular plastic zone close to the stretched zone inside the ligaments. The plastic deformation is also visualized on the real structure in the same location. The zoomed image of the re-entrant ligament was performed by optical microscope.

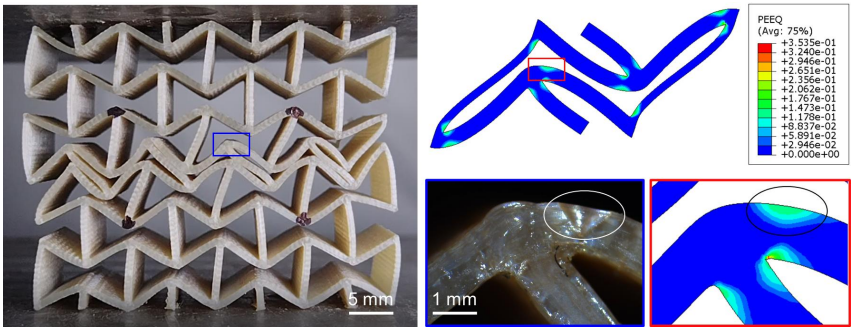

Figure 3.20: Predicting deformed shapes of Re-Entrant $\rho = 20\%$. The non-homogenous deformation predicted by RVE analys is compared with deformed ligament inside blue box post compression.

The numerical results for re-entrant UC with $\bar{\rho} = 30\%$ were depicted in figure3.21a. Increasing the relative density, the stress-strain curve moves up. The predicted Young's modulus remains consistent with the experimental ones as well as the initial collapse stress. The deformed shape at the same stress value is shown in figure3.21b. Both shapes exhibit buckling instability as in the lower density case confirming the effectiveness of RVE analysis.

As predicted in the experimental results section, high-density structures start to lose unit-cell integrities through inter-layer delamination failure mode. The numerical results for re-entrant UC with $\bar{\rho} = 40\%$ were depicted in figure3.22a. The stress-strain curves are completely different. The RVE analysis predicts about two times higher initial collapse stress. Although the deformed shapes can not be evaluated at the same stress level they differ either qualitatively or quantitatively.

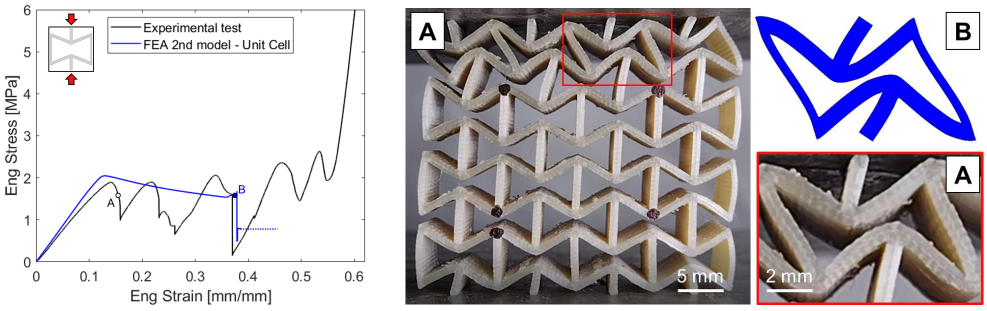

(a) (b)

Figure 3.21: Comparison between the experimental result and RVE analys of Re-Entrant $\rho = 30\%$ compressive behaviour. The FEA results are obtained using 2nd constitutive model. (a) Comparing mechanical properties. (b) Comparing the deformed shapes at A and B strain levels.

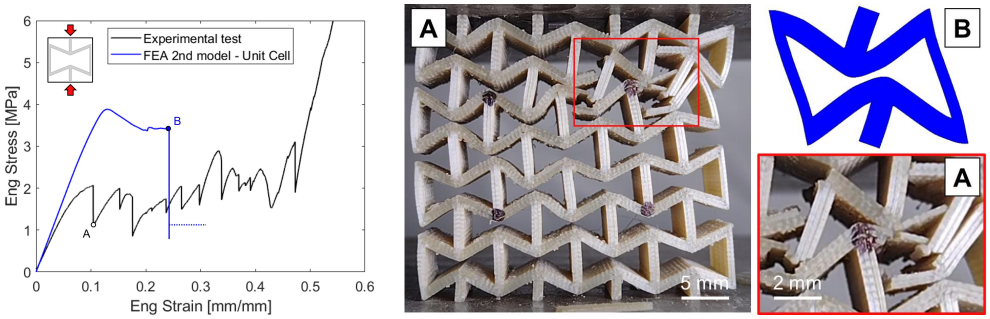

(a) (b)

Figure 3.22: Comparison between the experimental result and RVE analys of Re-Entrant $\rho = 40\%$ compressive behaviour. The FEA results are obtained using 2nd constitutive model. (a) Comparing mechanical properties. (b) Comparing the deformed shapes at A and B strain levels.

Therefore, the RVE analysis is able to predict Young's modulus, initial collapse stress, and Poisson's ratio in turn. The mismatches are due to losing unit-cell integrity. A comparison between these mechanical properties obtained through RVE analysis and experimental tests is shown in figure3.23. Figure3.23a shows Young's module. The numerical results predict a slightly stiffer linear elastic behaviour than an experimental one. As the relative density increases the predicted Young's module increase the numerical results exhibit an increase in the values differences. Figure3.23b shows the initial collapse stresses. The numerical results of unit-cell with relative density $\bar{\rho} = 20\%$ are consistent with the experimental ones. As the increase the relative density the numerical results start to diverge. As the relative density increases, the numerical prediction is getting higher and higher. The re-entrant unit-cell with relative density $\bar{\rho} = 30\%$ is still exhibiting the same initial collapse stress. The agreement has already been discussed before, the inter-layer delamination does not occur due to high filaments bonding strength. Figure3.23c

shows Poisson's ratio. The values are consistent also at higher relative density. This is because Poisson's ratio was computed at the initial strain values. The strain ratio is strongly dependent on the geometrical relationships in cellular materials rather than a constitutive one. Thus, the Poisson's ratio in these ranges is not affected by the nonlinear material response.

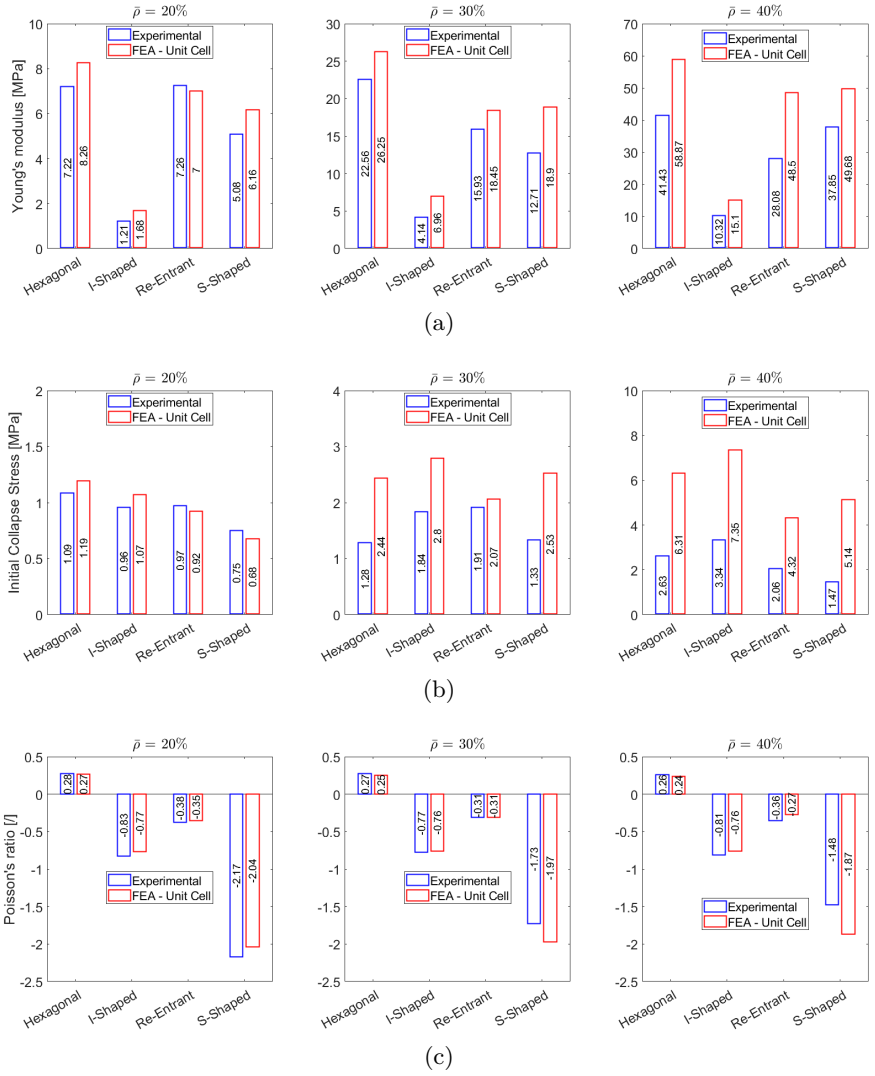

Figure 3.23: Comparison between the experimental and RVE analysis results in terms of Young's modulus (a) and Initial Collapse Stress (b).

3.4.2 Finite Element Analysis on Macro-Scale

The FEA on RVE shows an applicability limit on studying the absorption energy of cellular materials. The main issue is connected with the impossibility to evaluate the mechanical properties of the cellular materials being compacted. New cell-wall interactions are born during the unit-cell compression so the RVE analysis provides incorrect results after these points. To simulate the exact mechanical behaviour it

is needed to switch from the RVE scale to the macro-scale.

The FEA on macro-scale needs the real structure dimensions. The CAD model of each PEI honeycomb is sectioned along the vertical axis in order to create a planar shape with the 4-by-4 unit-cell configuration, as shown in figure2.4. The planar shapes were imported from nTopology to Abaqus software as deformable planar surfaces. The constitutive material model of 3D printed PEI was imposed on the planar shapes. The compression loading was not imposed on nodes as in the RVE analysis was done. The compression behaviour should be investigated also taking into account the interaction between the structure and the compressive metal plates. The metal plates were modelled in Abaqus as rigid wires. The plate length overtakes the structure length (48 mm) to guarantee a uniform compression when, also, the structure loses its integrity.

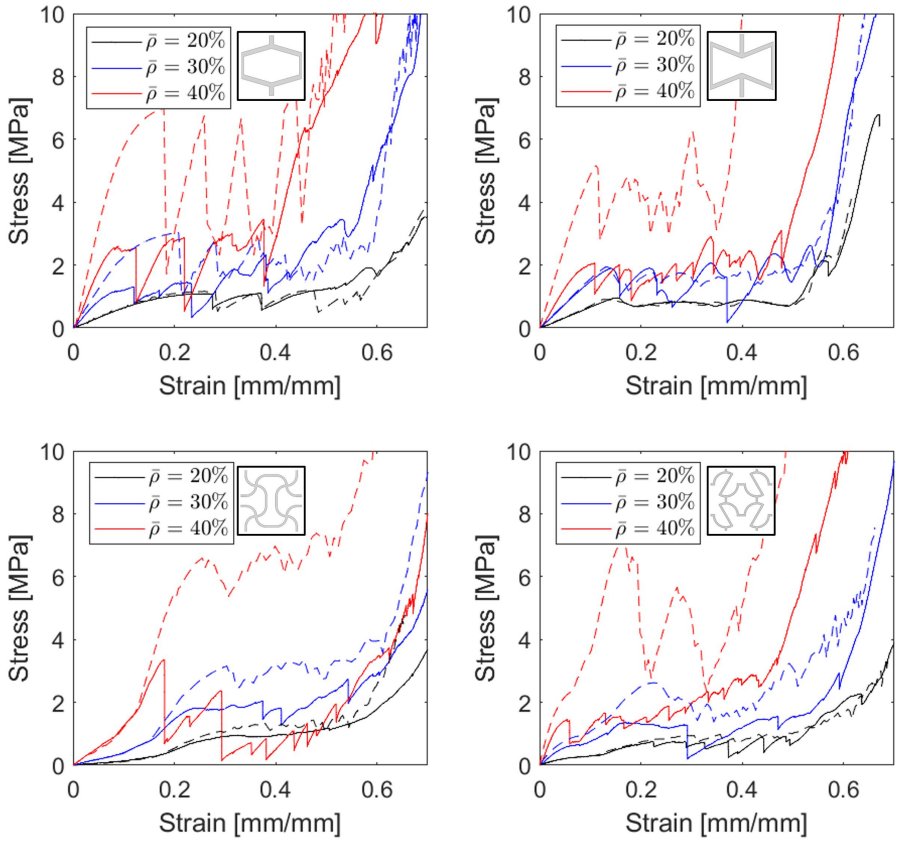

Figure 3.24: Mechanical properties of 3D printed structures. Continues lines are the experimental results. Dotted lines are the entire structures FEA results by using the 2nd constitutive model.

As in the FEA on RVE, the Abaqus explicit solver was used to perform the FEA on a macro-scale. The FE model has got the same features as the FE model on RVE. However, the first simulations exhibited dynamics compression effects. In detail,

compression loading is used to generate compressive waves that press stage-by-stage unit-cells from the moving plate to fixed ones up to the structure is compacted [122, 123]. This phenomenon is common in cellular materials under dynamics loading and it needed to be avoided in this study. Another undesirable phenomenon used to occur once the structure broke: the failure generates noisy waves inside the cellular material that led to undesirable unit-cell fluctuations or vibrations. Actually, some fluctuations led even to unit-cell premature failures. To eliminate these undesirable effects the model was improved by increasing the overall simulation time, from 10 s to 30 s, and introducing structural damping compatible with the polymer materials nature. The FEA computational effort became higher than in FEA on the RVE scale, so the mesh size was slightly increased from 0.1 mm to 0.3 mm. The stable increment time remains lower to 10^{-7}.

The stress-strain curves obtained by FEA on the macro-scale are shown in figure3.24. The mechanical response predicted by FEA results is consistent with experimental just for lower density honeycombs, i.e. black continuos (experimental) and black dotted (FEA) lines. The drop-off predicted by FEA is strictly connected with the failure of unit-cell layers. For example, the FEA on hexagonal honeycombs shows four stress drops off. They coincide with the failure of the four unit-cell layers. On the contrary, bending-dominated structures, i.e. I-shape and S-shape unit-cells, show a progressive stress-strain curve.

As discussed in the experimental section, the mechanical properties of the medium and high relative density honeycomb seem filtered in terms of stress by the inter-layer delamination failure mode. In fact, FEA predicts an extremely higher stress-strain curve than the real structure has. As the density increases the FEA results show higher initial collapse stress and plastic regimes with low-stress fluctuations. Otherwise, the densification strains are greater than the experimental because of the multi-delamination failure that decreases the unit-cells integrity.

The mechanical response of re-entrant structures was studied deeply to figure out which is the limit of the implemented numerical model. Both FEA and experimental results for re-entrant honeycomb with $\rho = 20\%$ were illustrated by the figure3.25. The stress-strain curves with the associated deformed shape are discussed. The A stage depicts the first layer collapse. Both FEA and experimental results show the unit-cell collapse mechanism due to cell wall instability. The re-entrant honeycombs keep compressing with the same collapse mechanism, i.e. B stage, up to the onset of densification strain is reached, i. e. C stage. The buckling phenomena occur layer-by-layer compacting the unit-cell without reaching brittle failures. The experimental evidence confirms the accuracy of the entire numerical model, from the constitutive model to the simulation settings. The extended ductility as well as the deformed shape further confirms the proposed strategy's effectiveness to evaluate 3D-printed PEI properties.

Subsequently, the FEA and experimental results for re-entrant honeycomb with $\rho = 30\%$ were illustrated by the figure3.26. The predicted collapse mechanism

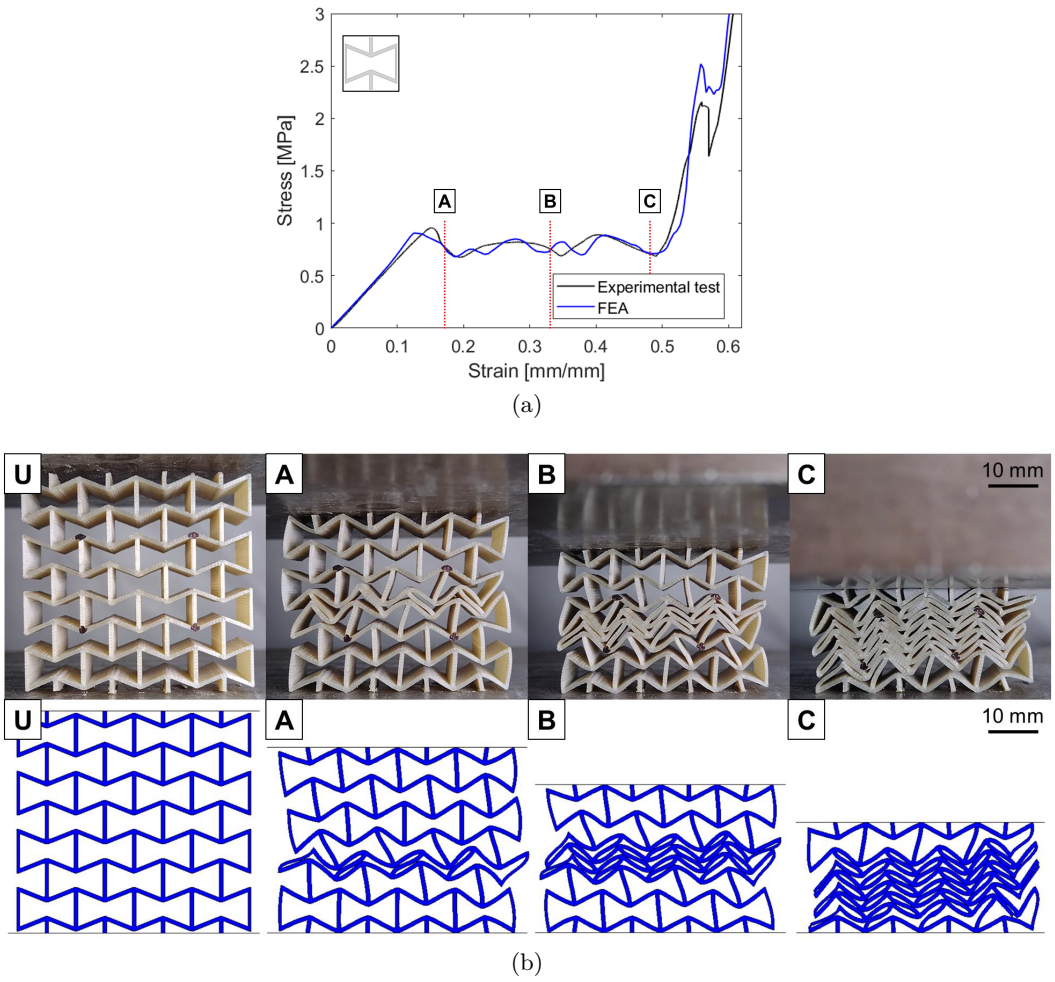

(a)

(b)

Figure 3.25: Compressive properties of Re-Entrant structure $\rho = 20\%$; experimental and entire structure FEA results. (a) Stress-Strain curves. (b) Deformed shapes in U,A,B,C strain levels.

si completely different from the experimental one. FEA predicts a layer-by-layer failure as the stages from A, B, and C show. The 3D-printed PEI is no longer able to withstand loading without failure once it is buckled. FEA reveal there is a small drop in tensile ductility on cell walls due to the presence of a multi-axial stress state[124]. Cell wall thicknesses are thicker than ones in lower relative density unit-cell, so the multi-axial stress state generates a high tensile stress state close to the stretched zone resulting in a drop in ligaments ductility.

The ligament failure occurs instantly because of the brittle 3D-printed PEI behaviour. The cracks propagate normally to the principal tensile stress direction. However, failures in experimental test results aligned to the extruded filament interfaces, i.e. interlayer delamination, as the red circles denote in figure3.26 (A and B stages). Implemented damage and damage evolution models are not able to predict these preferential crack propagation as well as all other damage models in Abaqus.

In addition, the recorded test videos show micro-sliding along these interfaces as the loading increases. These micros-slidings generate a premature change in the slope of the stress-strain curve.

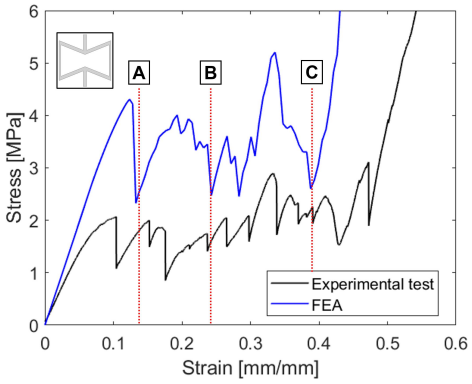

(a)

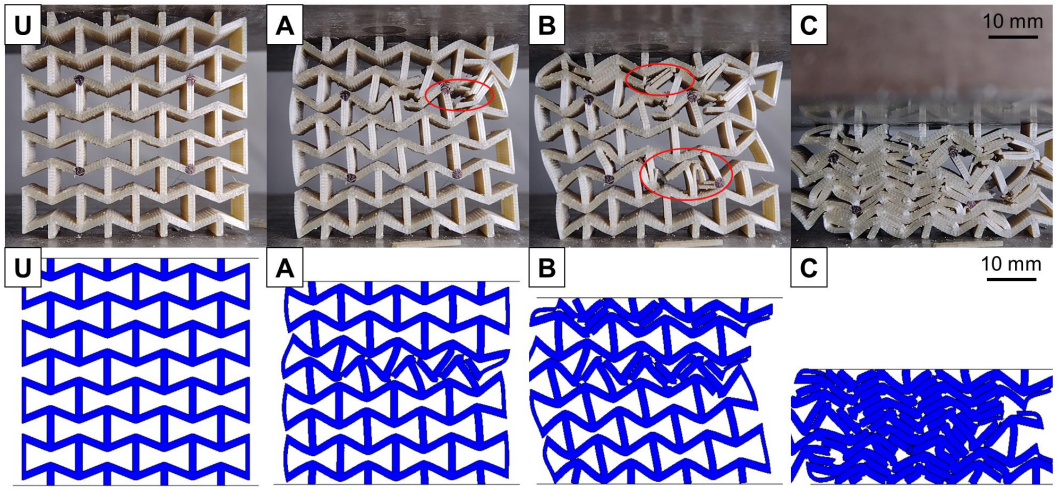

(b)

Figure 3.26: Compressive properties of Re-Entrant structure $\rho = 30\%$; experimental and entire structure FEA results. (a) Stress-Strain curves. (b) Deformed shapes in U,A,B,C strain levels.

.

The damage mechanism is also investigated on a micro-scale through tomography analysis. CT analyses were carried out on broken re-entrant honeycomb specimens, as shown in figure3.27. Although the re-entrant honeycomb with $\bar{\rho} = 20\%$ was printed extruding two filaments close to each other, the printed geometry does not exhibit defects along the filament interfaces. That means the structure has got a strong cohesion between the deposited filaments. In fact, the mechanical performances are accurately predicted by FEA. Blue circles denote cracks on stretched regions as the triaxial damage model predicted (equation XX from polymer mechanics). Moreover, a CT scan visualizes the stretched zone with darker than undeformed regions. Thus, these zones must have a lower density than undeformed regions and

these can be associated with craze formation, as figure3.2b shows. Deformation based on shear yielding mechanism should have been visualized with the same relative density of undeformed regions due to the shear yielding occurs at constant volume as well as plasticity in metals. Therefore, the CT scan confirms also experimentally the craze sensibility of 3D printed PEI. Moving to re-entrant honeycomb

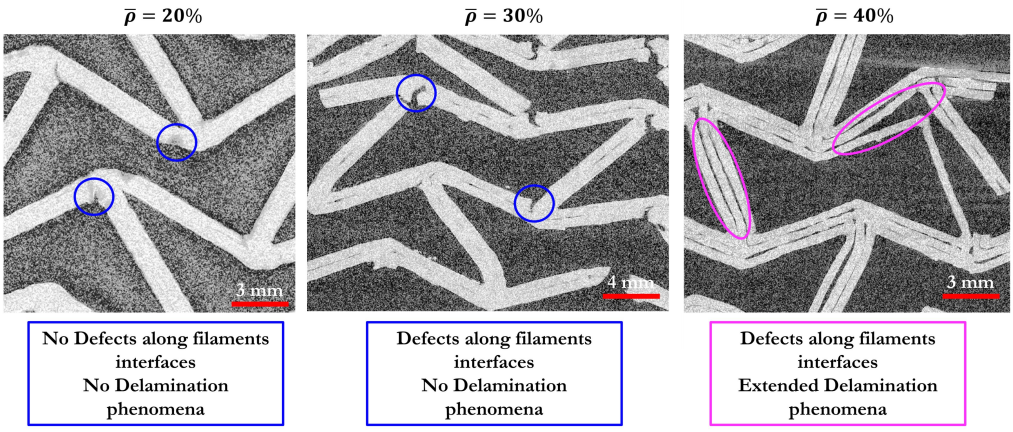

Figure 3.27: Computed Tomography Analisys of Re-Entrant structures after compression tests.

with $\bar{\rho} = 30\%$, micro-porosities along the interfaces of extruded filament appear. Although the number of filaments is the same, i.e. 2, the inter-layer delamination failure mode does not result. The failures are close to the unit-cell nodes as well as in lower-density structures. However, the crack propagates along the ligament's thickness breaking the re-entrant unit-cell.

On the contrary, the re-entrant honeycomb with $\bar{\rho} = 40\%$ exhibits micro-porosities along the extruded filament interfaces which generate extended inter-layer delamination zones once the bonding strength was overtaken. As discussed in the experimental section, the delamination phenomena reduce the unit-cell integrity leading to a premature failure of 3D-printed honeycombs. The need to improve the numerical model arises.

In literature, the mechanics of interlayer bonding in FFF-printed parts are still being studied[70]. Two approaches are commonly used to describe interlayer behaviour: microstructural or empirical based. The microstructure-based approach usually studies the thermal effects due to extruding process to polymer molecular entanglements and molecular diffusion[125, 126]. These models predict how the profile temperature affects the isothermal polymer strength at the interface involving microstructural phenomena such as entanglements, polymer relaxation, diffusion process, and so on. A graphical representation of interlayer bonding physics is illustrated in figure3.28. The fracture toughness at the bond interface G_c^w is connected to polymer microstructural properties and for instance the mode I fracture toughness

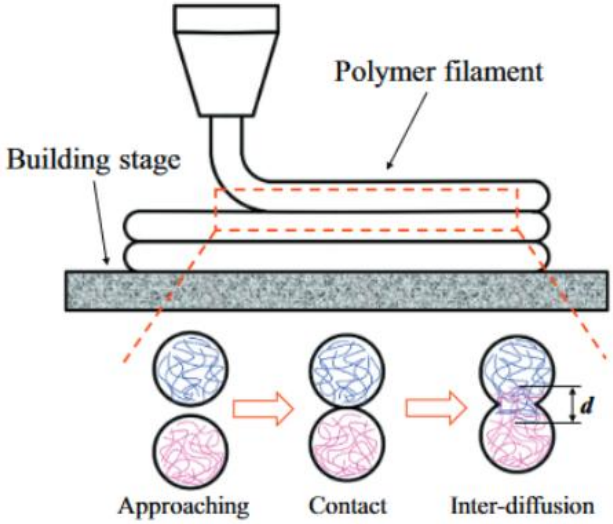

Figure 3.28: The inter-molecular diffusion between polymer fibers during FDM [15].

could be expressed by the following equation

$$G_c^w \approx \left(1 - \frac{1}{q v_w Z_{eq}}\right)^2 \tag{3.10}$$

where $q = 0.6$, v_w is for the entanglement fraction at the bond zone and Z_{eq} is the entanglement number of a melted polymer at the core. However, all this information is strictly dependent on the extrusion process and becomes challenging to predict the fracture toughness in each cellular structure point. Thus, the fracture toughness becomes also dependent on building plate temperature, extrusion speed, nozzle temperature, environment, and other printing parameters. In addition, interlayer failure can be generated by fracture mode I, mode II and mode III. This approach needs extensive effort to characterize the interlayer bonding strength.

The interlayer behaviour can be described through empirical failure criteria[85]. This approach is well-known in fibre composite materials and adhesives. These failure criteria are usually based on the Coulumb-Mohr hypothesis of brittle failure. These criteria define a maximum surface in shear - normal stress plane or space which can be defined as a safe zone, the most used are Coulumb-Mohr, Puck, maximum traction law, and so on[127]. If the multiaxial loading at the interface overtook the surface, a brittle failure will result. Among these criteria, Abaqus have already implemented failure criteria in which the damage interface is assumed to initiate when a quadratic interaction function involving the nominal stress ratios reaches a value of one as defined in the following expression

$$\left(\frac{\langle t_n \rangle}{t_n^0}\right)^2 + \left(\frac{t_s}{t_s^0}\right)^2 + \left(\frac{t_t}{t_t^0}\right)^2 = 1 \qquad \left(\frac{\langle \sigma_x \rangle}{\sigma_x^0}\right)^2 + \left(\frac{\tau_{xy}}{\tau_{xy}^0}\right)^2 = 1 \tag{3.11}$$

where the t_n is the normal stress normal to the interface and t_s is the in-plane shear stress. The maximum values are associated to t_n^0 and t_s^0, respectively. The vectot notation can be also expressed in terms of tensile stress σ_x and τ_{xy}, respectively. The criterion surface can be defined through multiaxial test on the filament interface.

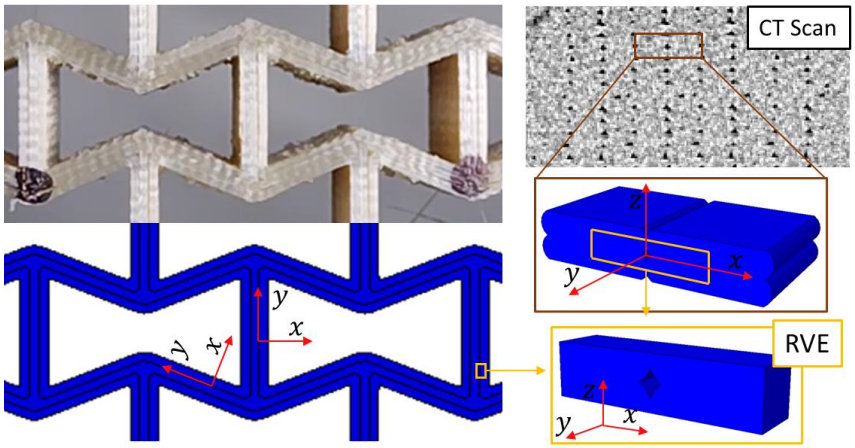

Figure 3.29: Strategy to determine the inter-layer delamination criterion. Sketch of Representive Volume Element along the extruded filaments interfaces.

In this study, a failure criterion based on an empirical approach was used. The failure criterion is exactly described by the equation3.11. However, the failure envelope was determined by FEA based on RVE theory instead of experimental testing. The proposed procedure is illustrated in figure3.29. From the CT scan of the dog-bone specimen with the same printing parameters of cellular materials, the CAD model of extruded filaments was obtained. The deposition strategy reveals a constant porosity distribution along the filament interfaces due to the extruded path, so the same porosity distribution is assumed to be also in 3D printed cellular materials. The reference system in figure3.29 allows explaining how the porosity should be oriented on the 3D-printed re-entrant honeycomb. As aforementioned in the experimental section, unit-cell 12x12 mm guarantees this constant solid part fillings as the density increases. From the CAD model, an RVE was obtained taking into account the porosity inside the RVE.

FEA on RVE of 3D printed PEI with periodic boundary conditions was carried out. The constitutive model of 3D printed PEI was used to describe the solid part in RVE. Subsequently, tensile loading and shear loading were applied to RVE. The maximum loading in terms of homogenized normal and shear stresses was calculated. These values correspond to the σ_x^0 and τ_{xy}^0 in the interface failure criterion on cellular materials. The obtained values were fitted by the equation3.11 and the surface is depicted in figure3.30.

This strategy neglects the mechanical properties close to the interaction because it is assumed the failure is due to the porosity distribution on RVE coupled with the brittle failure of 3D printed PEI. Therefore, this strategy aims to evaluate the

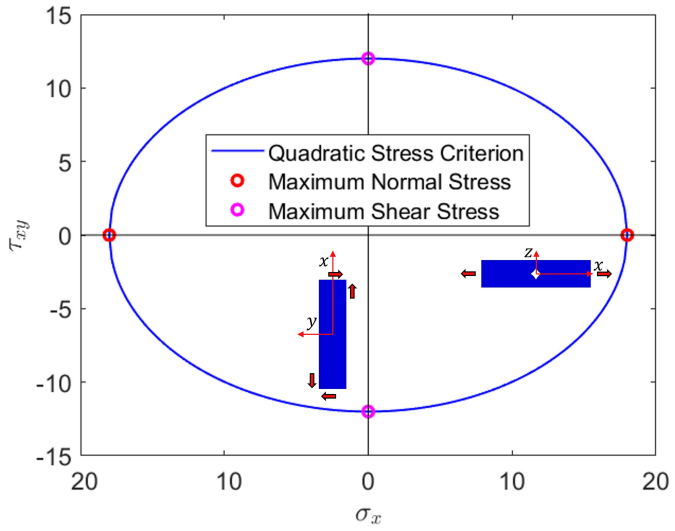

Figure 3.30: Quadratic stress criterion envelope. Simulated test were carried out to define the maximum normal and shear stress.

interface properties without performing another experimental test directly on the interfaces. For example, the σ_x properties can be evaluated by filling the dogbone specimens transversely to their own axis. However, the outer shells that usually envelope the filling must be eliminated because are aligned to the specimen axis. Otherwise, the transverse properties are not evaluable. Consequently, this study aims to propose an alternative procedure to simulate the cellular material mechanical response streamlining the experimental material characterization approach on FFF-printed material.

The previous numerical modelling was integrated with inter-layer delamination failure mode. The honeycomb topologies were modified according to the cellular materials associated extrusion path. The planar surfaces in Abaqus were split in the function of extruded filament inside the cellular materials. The interlayer failure was imposed on all interfaces through cohesive interaction in Abaqus in which the critical stress state follows the equation3.11. The damage evolution was imposed according to the tensile mechanical response obtained with FEA on RVE. In addition, normal and tangential interactions were imposed on the new broken interfaces which born after the failure. These modified FEA are called "FEA-layer" in the discussion of the following results.

The mechanical response of the hexagonal honeycomb with $\rho = 30\%$ was illustrated by the figure3.31. The stress-strain curves with the associated deformed shape are discussed. The red line describes the FEA with interlayer delamination. The numerical stress-strain curve exhibits a mechanical response compatible with the experimental one. The FEA predicts a lower initial collapse stress than FEA without inter-layer delamination because of the localized deformation along the interfaces. The inter-layer phenomenon filters possible high mechanical properties as from ex-

perimental observations. The FEA is not able to predict all stress drop off but it seems to follow the entire mechanical response. The A stage in figure3.31 shows a qualitatively comparable deformed shape between FEA and the experimental test. The hexagonal unit-cell failure is no longer layer-by-layer but localized. Coupling the 3D printed PEI material damage with the inter-layer failure the unit-cell exhibits, it is predictable: the localized unit-cell snap-trough instability, brittle failure of ligaments and inter-layer delamination. The deformed shape of the A stage predicts consistently the effects on unit cells around the first failure. The coherence in terms of deformed shape is validated also at high strain stages, as B and C stages show in figure3.31.

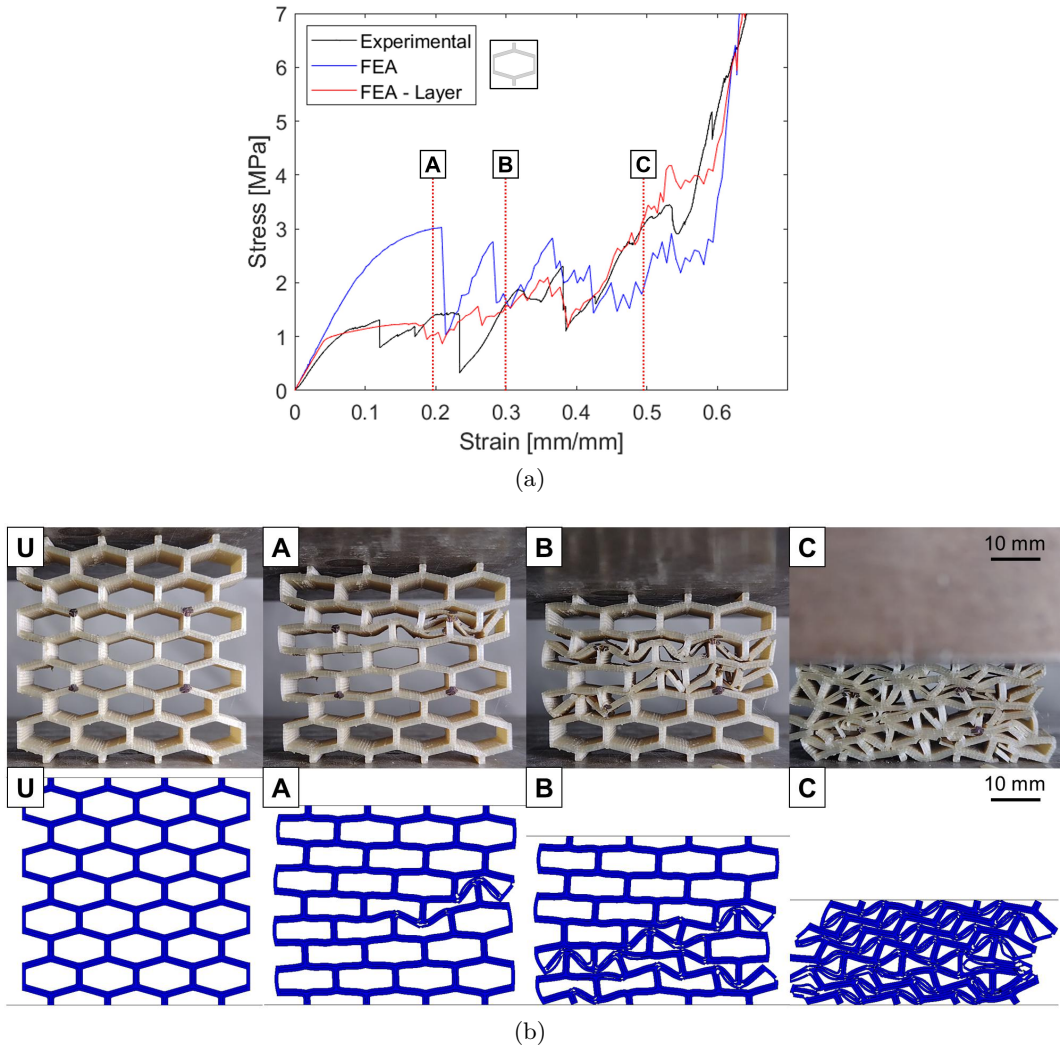

(a)

(b)

Figure 3.31: Compressive properties of Hexagonal structure $\rho = 30\%$; experimental and entire structure layer FEA results. (a) Stress-Strain curves. (b) Deformed shapes at U,A,B,C strain levels.

The mechanical response of re-entrant honeycomb with $\rho = 40\%$ was illustrated

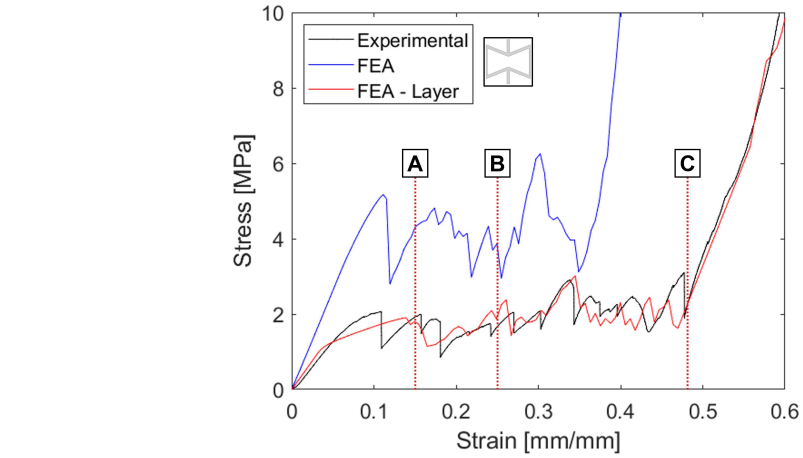

(a)

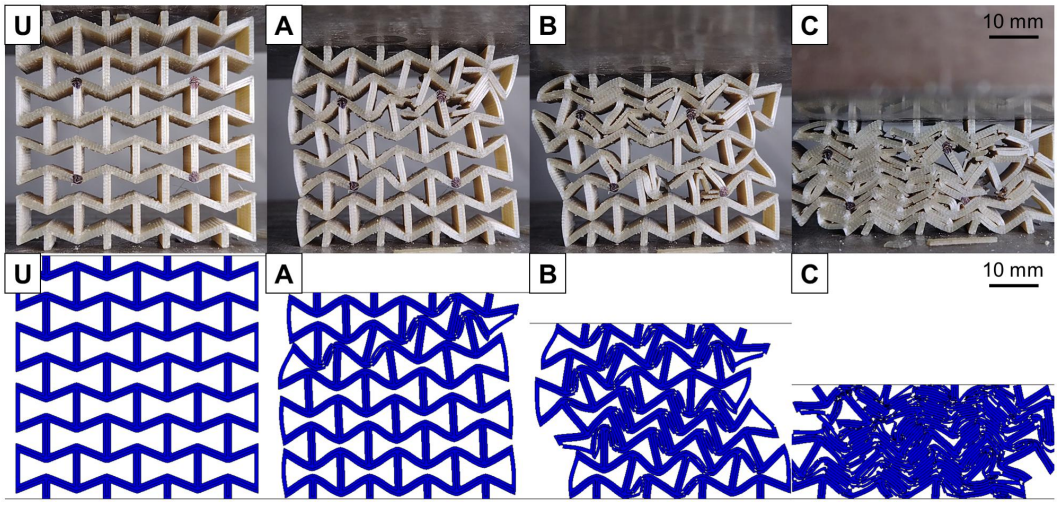

(b)

Figure 3.32: Compressive properties of Re-Entrant structure $\rho = 40\%$; experimental and entire structure layer FEA results. (a) Stress-Strain curves. (b) Deformed shapes at U,A,B,C strain levels.

by the figure3.32. The stress-strain curves with the associated deformed shape are discussed. Also in this case the red line exhibits a mechanical response compatible with the experimental one. The FEA predicts an angled deformation of re-entrant unit-cells instead of layer-by-layer as the A stage shows in figure3.32. The unit-cell topology generates unit-cell buckling phenomena but the inter-layer failure on cell walls avoids the unit-cell brittle failure folding the unit-cell walls. Experimental evidence confirms the angled compression response. The experimental test shows a slightly higher brittle failure on ligaments than FEA. That is a threshold of the numerical model predictions. The failure mode for the solid part and interlayer are defined separately, so once an interface fails the crack propagates parallel to the interfaces avoiding a possible transverse crack opening. However, the overall

honeycomb mechanical response is driven by inter-layer delamination instead of brittle failures.

Other two examples of deformed shape consistency between experimental and numerical results are discussed. The mechanical response of the I-shape honeycomb with $\rho = 40\%$ was illustrated by the figure3.33. Also in this case the red line exhibits a mechanical response compatible with the experimental one. The FEA without inter-layer failure predicts an extremely higher stress-strain curve than FEA with. The cause of this difference is illustrated in figure3.33b. At stages A, B, and C all structures reach the same strain associated with initial collapse stress in the experimental test. The deformed shape in the experimental test shows a local ligament folding due to the interactions between cell walls. In FEA without inter-layer, once the cell wall interactions occur the ligament keeps compressing without sloping. The structure integrity is able to withstand high horizontal compression caused by the vertical compression loading increasing the overall structural stiffness as the change in slope in stress-strain shows. That means, the inter-layer failure locally weakens the ligaments and then the horizontal compression folds these ligaments, as the FEA with inter-layer predicts. In fact, its deformed shape is consistent with the experimental test. The compression loading drops off because the folded cell walls enable sliding between them instead of reacting in the horizontal direction.

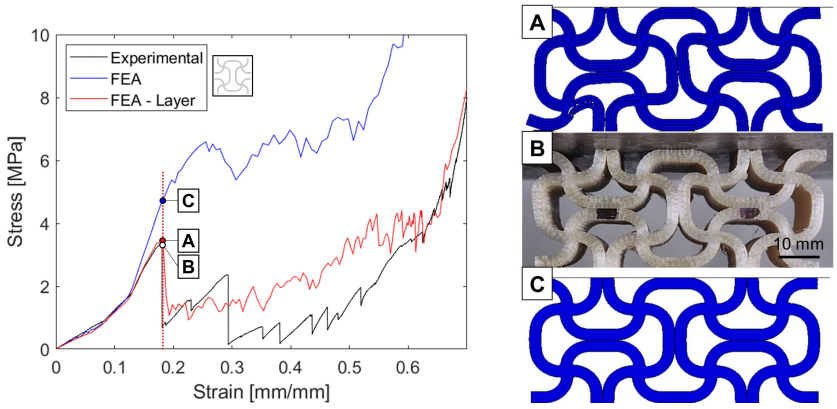

(a) (b)

Figure 3.33: Compressive properties of I-shape structure $\rho = 40\%$; experimental and entire structure layer FEA results. (a) Stress-Strain curves. (b) Deformed shapes at A,B,C strain levels.

The mechanical response of the hexagonal honeycomb with $\rho = 40\%$ was illustrated by the figure3.34. Also in this case the red line exhibits a mechanical response compatible with the experimental one. At stages A, B, and C all structures reach the same strain associated with initial collapse stress in the experimental test. However, the experimental results show a premature folding of horizontal ligaments due to the inter-layer debonding. The ligaments locally fold without exhibiting brittle failure. As in the previously discussed case, the inter-layer failure weakens the cell

walls avoiding the structure to withstand higher stress loadings.

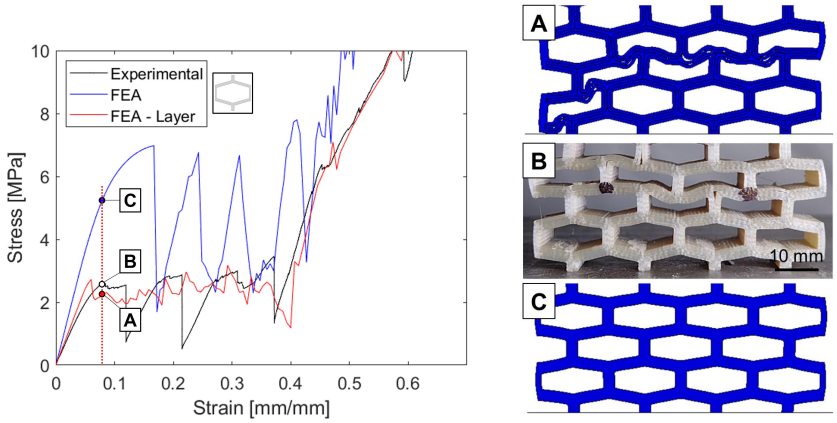

(a) (b)

Figure 3.34: Compressive properties of Hexagonal structure $\rho = 40\%$; experimental and entire structure layer FEA results. (a) Stress-Strain curves. (b) Deformed shapes at A,B,C strain levels.

Figures 3.38, 3.39, and 3.40 show a comparison in terms of stress-strain curves between experimental test and FEA results with and without modelling inter-layer failure. A great consistency between the experimental and numerical evidence confirms the accuracy of the FEA with inter-layer failure modelling; from the constitutive model, failure modelling to the simulation settings. The extended ductility as well as the deformed shape further confirms the proposed strategy's effectiveness to evaluate the mechanical performances of 3D-printed PEI cellular materials.

The numerical model results allow predicting the honeycombs' mechanical performance if they would not have inter-layer failures. The FEA without inter-layer failure shows stress-strain curves higher than the experimental, thus if the additive manufacturing process was able to avoid or reduce the porosity along the deposited filaments the mechanical performances should be the ones predicted by FEA without inter-layer failure. Moreover, the comparison could allow evaluating the achievable mechanical properties. Thus, it could determine if improving FFF process parameters is worth it instead of changing the base material or the manufacturing process.

Consequently, the mechanical performances are compared in figure3.35. The effects on Young's modulus and initial collapse stress are quite obvious. The inter-layer failure generates structures with lower stiffness as well as lower strength. In detail, the FEA predicts an increase of 50% in terms of strength for structures with $\bar{\rho} = 30\%$ and even an increase of 250% for structures with $\bar{\rho} = 40\%$. Young's modulus is lower sensible to inter-layer failure than strength; a mean increase of 20% for structures with $\bar{\rho} = 30\%$ and an increase of 50% for structures with $\bar{\rho} = 40\%$.

The SEA predicted by FEA without inter-layer failure results extremely higher than experimental tests. First of all, FEA results confirm the SEA of structures should have been increased as the density increases. Secondly, the results affirm that

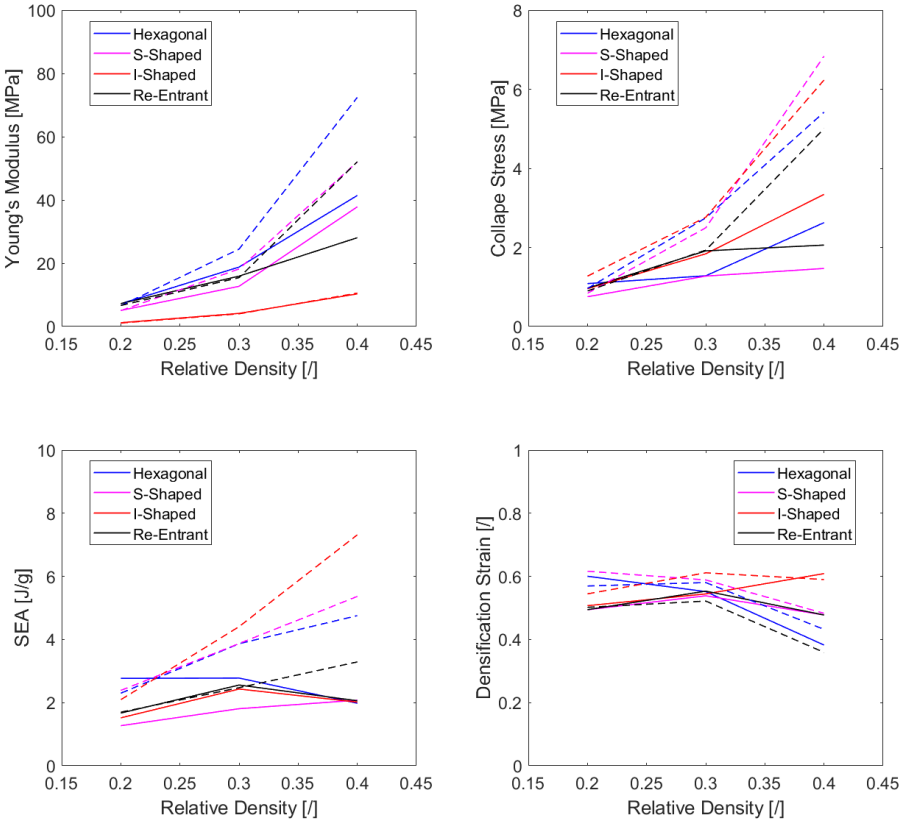

Figure 3.35: Mechanical properties of structures; Continuos lines are the experimental results. Dotted lines are the FEA results on entire structures without delamination criterion.

inter-layer failure are an extremely negative effect on the energy absorption capacity of structures. The SEA should have been raised about 240% in I-shape, S-shape, and hexagonal honeycombs. These findings could result in a countertrend, in many impact absorption applications the delamination failure of fibre composite material is a benefic effect. However, the delamination in those cases is useful because of the brittle behaviour of the composite material[128]. The delamination failure leads to progressive damage which enables a progressive energy absorption[129]. In cellular materials, the energy absorption capacity is guaranteed by the cellular material topology. Thus, the solid part of cellular material should be flexible and ductile to take advantage of all energy absorption peculiarities of cellular material. A low structural unit-cell integrity leads to premature failure and so limited mechanical properties.

On the contrary, the densification strain is not sensible to inter-layer failure. That means the solid part remains under the compressive plate without working. The delaminated zone keeps attached to each other and thus, the solid fraction of com-

pressed cellular material is the same.

FEA unveils hidden mechanical performances of the I-shape and S-shape, especially the SEA could be higher than all other structures. Both structures have a strong potential in energy absorption application.

The effects of inter-layer failure can be also seen in energy-absorption diagrams, in this chart the normalized collapse stress is adimentionalized by initial collapse stress and not by σ_p. Figure3.36 shows the honeycombs properties obtained by the experimental testing, i.e. real properties, and the honeycombs properties predicted by FEA without inter-layer failure, i.e. achievable properties. The chart shows increasing relative density there is not a real gains in terms of energy. All point remains confinated in the same area, i.e. yiellow ellipse. That means, both initial collapse stress and energy absorbed are not increasing. The inter-layer failure could give a positive effect on energy absorption application avoiding initial collapse stress increases. However, the associated energy values are too low to result a real positive effect. Neglecting the inter-layer failure, the EA performances increases but the initial collapse stress too. Thus, the honeycombs might be able to overtake the limit due to premature failure improving on additive manufacturing process parameters, as figure3.36 predicts.

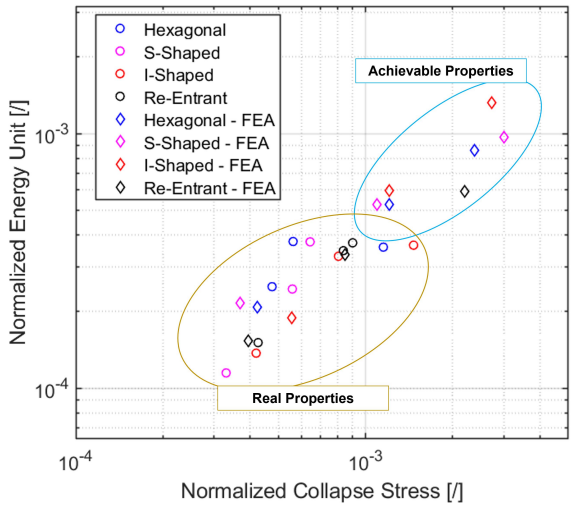

Figure 3.36: Achievable energy absorbtion properties.

3.5 Concluding Remarks

A numerical modelling strategy was introduced to simulate the PEI honeycombs' mechanical responses. According to glassy thermoplastic polymer physics, the 3D-printed PEI constitutive model was defined; hence, it was assumed the polymer mechanics can be described through competitions of crazing (brittle failure) and shear yielding (extended ductility). Firstly, the mechanical characterization was

carried out following traditional techniques. However, the extreme PEI brittleness revealed inconsistency between numerical and experimental results.

Following experimental and theoretical observations, the 3D-printed PEI properties were defined through an inverse method. The new failure strain under the tensile test was looked for along the stress-strain curve of the PEI filament. The numerical optimization revealed an increase in failure strain and thus an increase in PEI ductility. The updated numerical model was confirmed by comparing the experimental test results with the numerical ones: tensile, shear, compression, triaxial, and three-point bending tests.

The updated numerical model was used to predict the mechanical performances of PEI honeycombs. Firstly, the FE analysis on RVE with PBC was carried out. Secondly, the mechanical performances of the macroscopic structures were simulated. The FEA results predicted the stress-strain curves of structures with low relative density but, by increasing it, the results diverged. It was necessary to model the interlayer delamination failures.

The failure at the extruded filament interfaces was evaluated taking into advantage failure criteria based on shear-normal stress relation. A simulated test on RVE of 3D-printed PEI was carried out to define the failure criteria surface. Then, a criterion damage interface is assumed to initiate when a quadratic interaction function involving the nominal stress ratios reaches a value of one. In the end, the previous FEA on the macro-scale were improved with filament interfaces and this criterion.

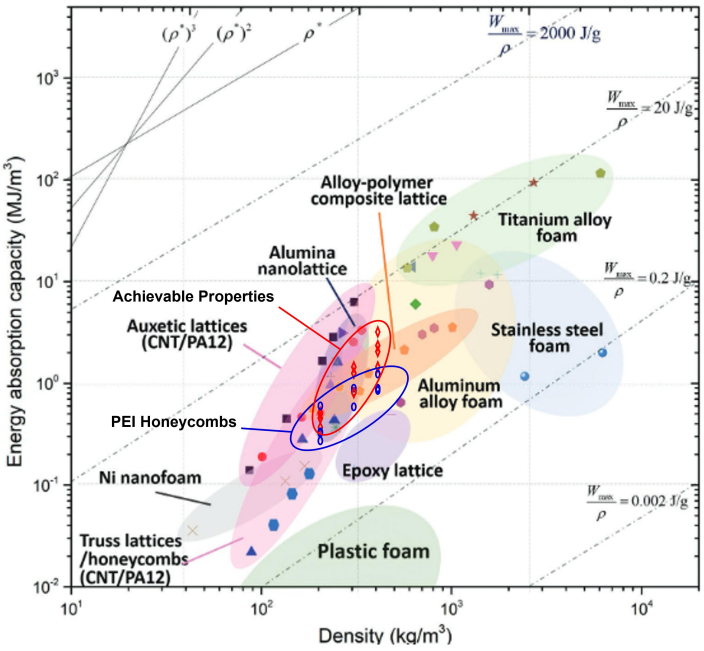

Figure 3.37: Ashby map of energy absorption per unit volume versus density [5]. The PEI cellular materials properties are depicted by blue circles. The achievable PEI honeycombs propertiesare depicted by red circles.

The FEA with interlayer failure were able to predict the compressive response of 3D-printed PEI honeycombs. Comparing both FEA results, it was evident that interlayer failures reduce the overall mechanical performance of 3D-printed parts. The comparison also explains why the SEA did not increase as the relative density increased. Moreover, FEA without interlayer failures unveils hidden mechanical performances of the I-shape and S-shape, especially since their SEA could be higher than all other structures resulting in a strong potential in energy absorption application.

In conclusion, the introduced numerical simulation procedure is able to predict the compressive mechanical behaviour of PEI honeycombs with three relative densities and four unit-cell topologies. It quantifies the negative effects due to interlayer failure and therefore to the additive manufacturing process. From another point of view, the numerical procedure allows for predicting the hidden mechanical properties of parts. For example, figure 3.37 shows the achievable energy absorption capacity of 3D-printed PEI honeycombs without interlayer failures (red circles), confirming the high PEI potentiality. The red circles are higher than the blue, i.e. real data, and this gap might be filled by improving additive manufacturing process parameters. Therefore, the numerical simulation procedure might be exploited to quantify the effectiveness of 3D-printing process parameters.

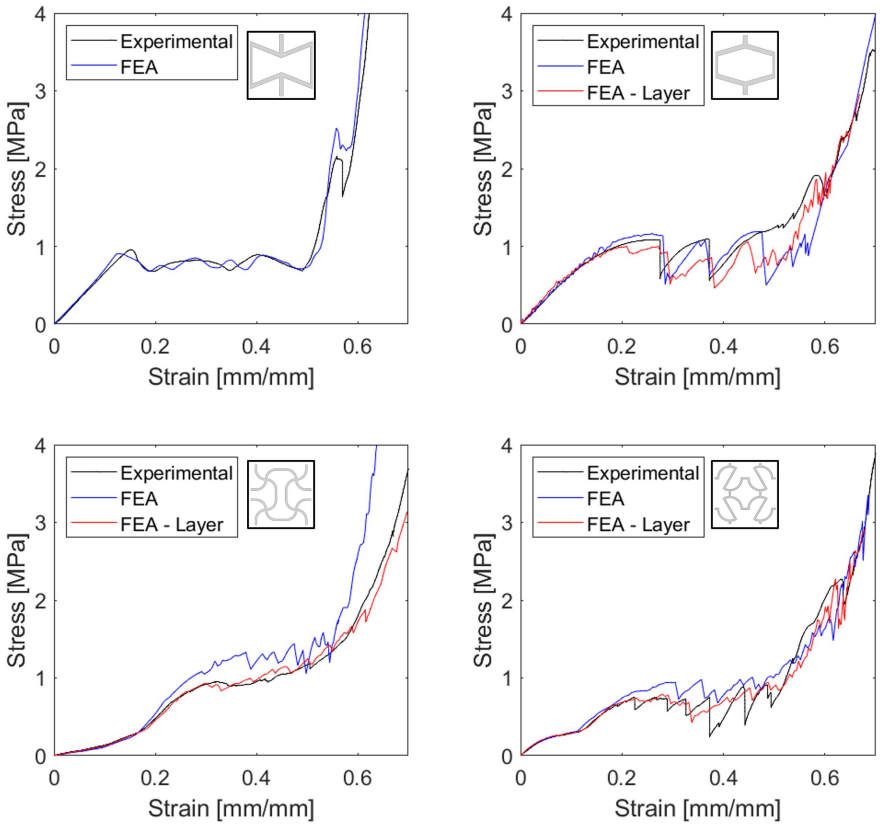

Figure 3.38: Compressive properties of structure $\bar{\rho} = 20\%$; experimental and entire structure FEA results.

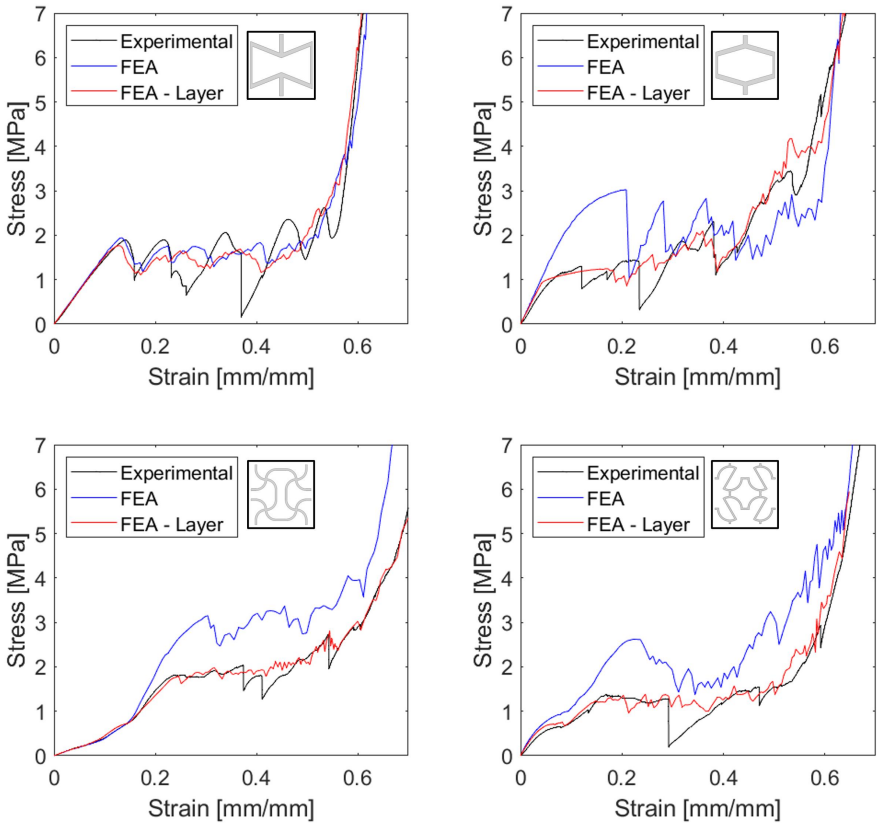

Figure 3.39: Compressive properties of structure $\bar{\rho} = 30\%$; experimental and entire structure FEA results.

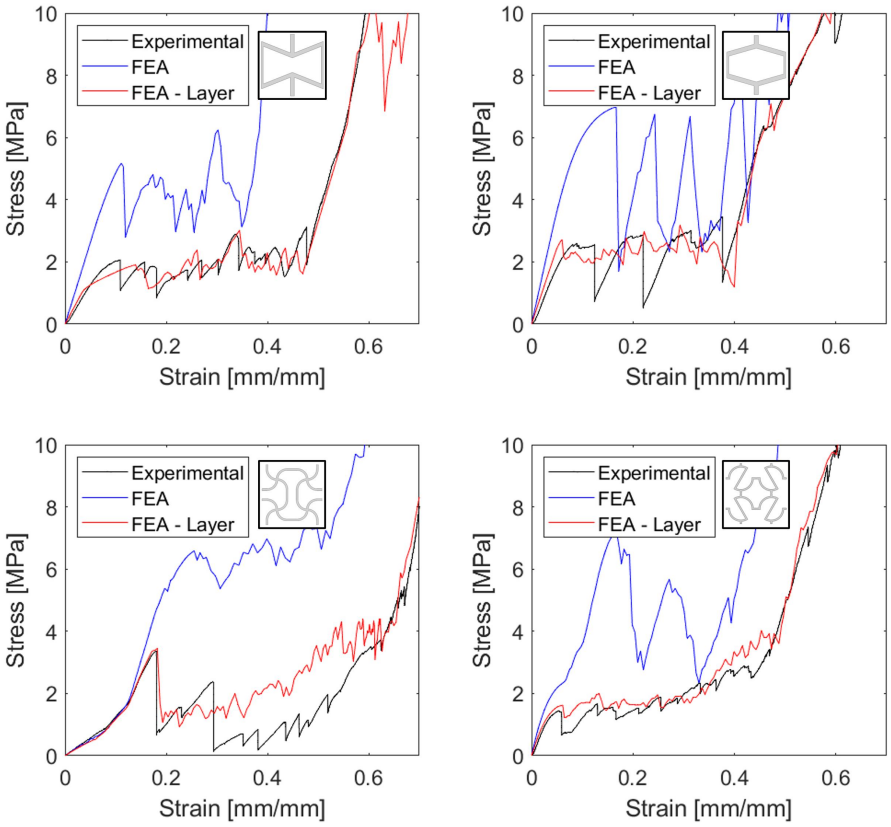

Figure 3.40: Compressive properties of structure $\bar{\rho} = 40\%$; experimental and entire structure FEA results.

Chapter 4

Self-Sensing PEI Composite Metamaterials

4.1 Introduction

Nowadays, designing cellular materials aiming to improve only mechanical properties is anachronistic. Human needs to design cutting-edge materials to overtake the limit that natural materials have. Two approaches enable that. At first, designing a material able to reach properties was unthinkable before. Secondly, designing a material able to achieve multi-functional performances. Both approaches drive cellular material design to the present and future. These new materials are called metamaterials.

The definition of metamaterials derives from a more elegant greek word $\mu\varepsilon\tau\alpha$ and Latin *materia*; the literal meaning is "beyond material". As the beautiful name suggests, a metamaterial is any kind of material have a property that is not found in natural materials. Therefore, metamaterials are human-made, usually called also artificially engineered materials or synthetic composite materials. For example, the auxetic honeycombs studied in the previous sections are metamaterials. In that case, artificial unit-cell topologies give these honeycombs a "beyond" property: auxeticity. No one material in nature exhibits a Poisson's ratio as low as the I-shape or S-shape did.

Metamaterials are usually referred to as architected cellular materials because they metamaterials majority are made up of periodic structures, open or closed cells, rationally repeated inside a single bulk material. As the cellular materials, the metamaterials can be periodic in 1-Dimension, 2-Dimension (metasurfaces[130]) or in 3-Dimension. The metamaterial can be classified according to the physics property that they are going to enhance: acoustic, mechanical, electromagnetic, optical, and transport. The strategy to enhance physics properties is based on similarities, e.g. acoustic-mechanics or electromagnetic-optical. In addition, the metamaterial can be designed as homogeneous or inhomogeneous metamaterial distribution[131].

The enhanced material property is usually referred to as an effective macroscopic property such as electrical conductivity, Hall coefficient, electric permittivity, Young's modulus, Poisson's ratio, and so on. As metamaterial belongs to cellular

materials, the homogenization technique becomes a strong tool to describe these effective macroscopic properties. Although, it is currently impossible to homogenize any arbitrary periodic map innovative techniques keep making progress in this direction[132].

Some examples of extraordinary metamaterials potentiality and innovative applications are proposed. In electromagnetism and optics, metamaterials enable negative refraction. These metamaterials are commonly called "left-handed material (LHM)" or "negative-index material (NIM)". Negative refraction affects the light propagation direction through an interface between two materials. LHM's, theoretically predicted by Veselago[133], have simultaneously negative electric permittivity ϵ and magnetic permeability μ. In nature is highly unusual that the material has got both electromagnetic properties negative[134]. This feature leads to a new interpretation of physical phenomena such as Poynting vector, Doppler effect, Cherenkov radiation, Snellius law, and Fermat principle. Moreover, LHMs achieve the conceptualization of perfect absorbers or perfect lenses.

Negative refractive indices can be obtained in acoustics in analogy to optics[131]. The compressibility κ in solids is mathematically analogous to the electric permittivity ϵ, and the mass densityρ is analogous to the magnetic permeability μ [135]. That conceptualization of a perfect acoustic absorber becomes real combining finite absorption with independent adjustment of frequency-dependent bulk modulus magnitude B(ω) and frequency-dependent mass $\rho(\omega)$. As aforementioned before, another example of metamaterials enhanced property is auxeticity. Elastic solid exhibits Poisson's ratio between +0.5 to -1, and metamaterial achieves Poisson's ratio lower than -1 as shown by S-shape cellular structure. This characteristic leads to a low bulk modulus B compared to shear modulus G, which means the metamaterial prefers to deform through volume change instead of shape change.

In mechanics, these kinds of metamaterials are usually defined as poroelastic metamaterials. They are cellular materials in which voids (support phonons) are filled by air or fluid (support acoustic waves). For example, Qu et al. propose a poroelastic material in which the bulk modulus B is negative or compressibility κ is positive[136]. Recent theoretical work makes a further step beyond introducing the gyroelastic metamaterials, which are the counterpart of Faraday active metamaterials in optics[137]. The traditional mechanics of solid is no longer able to describe the real mechanical properties of poroelastic materials because of the limits of Cauchy elasticity stress tensor statement. The mechanics of poroelastic materials need to couple displacement and rotation in continuum mechanics, thus the Erigen micropolar continuum mechanism is recently successful. The Erigen micropolar continuum mechanics is based on Cosserat elasticity instead of elastic elasticity[138]. Introducing this tensor is even possible to achieve the chirality effect, i.e. twisting phenomenon due to axial compression[139].

An extreme feature metamaterial achieves in electromagnetism and acoustic is *cloaking*[140]. Cloaking in physics is connected to the idea to make objects invisible

and derives from the "invisibility cloak". Hiding objects to the eye has a very long history but none achieved yet. Thanks to metamaterials are getting to be real[141]. Invisibility studies are quite established in electromagnetism or acoustic where the need to hide submarines or jets has driven the research on this topic. First stage of invisibility consisted to avoid the incident acoustic or electromagnetic waves bouncing back to the source. It is commonly called stealth. Nowadays, the idea of invisibility is improved and referred to as cloaking; for example, electromagnetic waves run in the air toward a body protected by a cloak. Once the waves overtake the body the electromagnetic field remains unchanged outside the cloak. Therefore, the body is invisible electromagnetically. Figure4.1 from Schurig et al. work explain better the cloaking phenomena[16]. Several articles can explain better how the cloak generates invisibility [141]. Analogies between electromagnetism, optic, acoustic, and mechanics lead to introduce cloaking also in dynamics of materials[142]. Designing an inhomogeneous metamaterial allows to the creation of a near-cloaking phenomenon also in elastic wave propagation[143, 144]. Now, the idea is hiding surface defects from incoming compressional, shear or Rayleigh waves, but in the future could be possible to hide an entire body or create the perfect impact absorber even.

Metamaterials belonging to the transport family are able to enhance response functions such as electrical conductivity σ, diffusivity D, thermal conductivity κ, Hall coefficient, magnetoresistance, and so on. An interesting study concerns the sign reversal of Hall coefficient in chainmail metamaterials. Kern et al. determine the Hall coefficient of metamaterials in functions of unit-cell topologies. Changing the chainmail topology can create a positive or negative metamaterial with Hall coefficient[145].

In this study, the PEI composite cellular materials are metamaterials belonging to transport and mechanical families. The mechanical properties to enhance are the Poisson's ratio as well as the PEI honeycombs discussed in the previous sections. In addition to that, composite PEI is electrically conductive with a strong nonlinear resistivity. This feature allows to composite PEI cellular materials to achieve orthotropic electric conductivity and piezoresistive behaviour. Piezoresistivity is the key property this study aims to investigate. Coupling mechanical, lightweight, electrical, and piezoresistive performance PEI composite honeycombs can be defined as smart metamaterials with a strong potential for self-sensing.

Self-sensing material is material able to monitor its properties by own self; hence, without any measuring instrument applied to it. That means the honeycomb's piezoresistive behaviour enables monitoring mechanical performance such as stress, strain, and damage evolution. Smart materials are getting more important in the biomedical sector where the need to monitor an implant without measuring instruments is real. However, smart materials are also important in aerospace, automotive, security, defence or industrial applications.

Piezoresistive materials are well studied in literature but they are usually referred to as natural materials[146]. Piezoresistive materials in nature exhibit giant piezore-

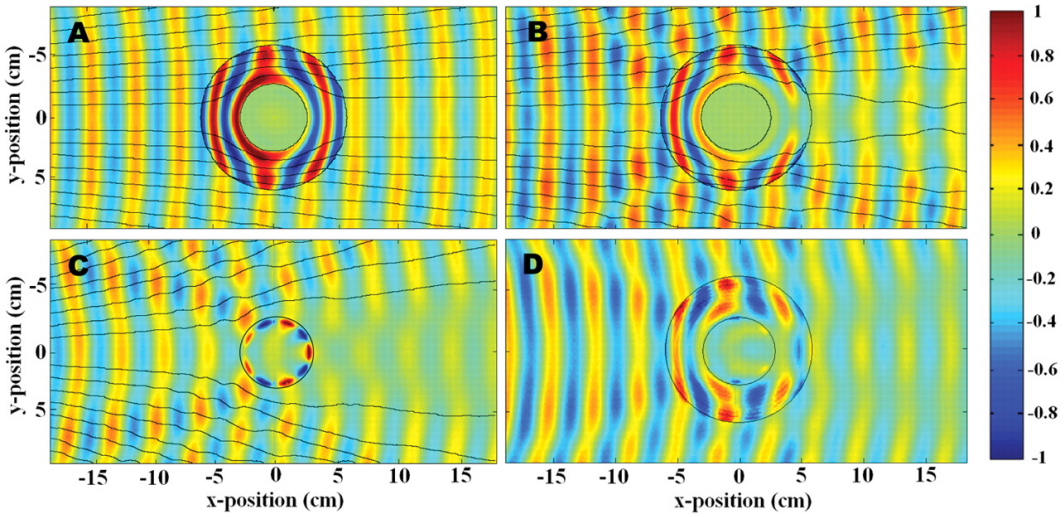

Figure 4.1: Snapshots of time-dependent, steady-state electric field patterns, with stream lines [black lines in (A to C)] indicating the direction of power flow (i.e., the Poynting vector). The cloak lies in the annular region between the black circles and surrounds a conducting Cu cylinder at the inner radius. The fields shown are (A) the simulation of the cloak with the exact material properties, (B) the simulation of the cloak with the reduced material properties, (C) the experimental measurement of the bare conducting cylinder, and (D) the experimental measurement of the cloaked conducting cylinder. Animations of the simulations and the measurements (movies S1 to S5) show details of the field propagation characteristics within the cloak that cannot be inferred from these static frames. The right-hand scale indicates the instantaneous value of the field[16].

sistivity as silver, nickel or carbon-based materials but they can not withstand high deformation. This disadvantage makes it impossible to create a self-sensing structure so they are usually used as measure instruments, i.e. strain gauge base materials. Additive manufacturing coupled with conductive dopant material enables the manufacturing of complex conductive composite cellular materials unthinkable before. Thus, it is possible manufacturing a self-sensing structure composite based. In literature, professor Kumar is a pioneer in the piezoresistivity of additively manufactured metamaterials. He investigates the piezoresistive behaviour and the achievable gauge factor of several FFF-based composite metamaterials, pointing out the strong honeycombs and lattice structures potentiality[67, 68, 72].

As aforementioned in the Introduction section, neat PEI is a high-performance thermoplastic material. It has extreme potential in applications where the structural, thermal and toxicity properties are the must-have properties. Moreover, the PEI amorphous microstructure gives it excellent 3D printability. PEI becomes conductive once carbon nanotubes are dispersed within it. All these advantages bring to PEI composite as a highly valuable base polymer for structural self-sensing meta-

materials.

The main innovation in this study is evaluating the self-sensing properties of PEI composite metamaterials due to none have done it before. Furthermore, a piezoresistive model based on Finite Element Methods is proposed. Multi-physics software like Comsol is able to model piezoresistive behaviour but they are not well established in research as Abaqus. Abaqus is able to solve large nonlinear complex problems, implement much constitutive behaviour, and be robust but the multi-physics options are still raw. In this study, a strategy to model the nonlinear piezoresistive behaviour in Abaqus is proposed and it was applied to validate experimental tests. The research is ongoing yet but it was proposed up to the last update. Both theory and testing of piezoresistive behaviour of metamaterials are not well explained in the literature, thus the piezoresistivity is discussed from theory to testing following the literature and own observations.

4.2 Piezoresistivity Theory and Mechanisms

Electrical resistivity or volume resistivity is a physic intrinsic material property that corresponds to the resistance of electric current flow. Lower is the electrical conductivity and higher is flowing of charged particles inside the solid. Electrical conductivity, i.e. σ, is the reciprocal quantity of electrical resistivity, i.e. ρ, and the units are S/m and Ωm, respectively.

The most general definition of electrical resistivity in space is by tensor resistivity $\bar{\bar{\rho}}$. It connects the electric field $\bar{E}$ with the electrical current density $\bar{J}$ following the general tensorial notation:

$$\bar{\bar{\rho}} = \frac{\bar{E}}{\bar{J}} \Leftrightarrow \begin{bmatrix} E_x \\ E_y \\ E_z \end{bmatrix} = \begin{bmatrix} \rho_{xx} & \rho_{xy} & \rho_{xz} \\ \rho_{yx} & \rho_{yy} & \rho_{yz} \\ \rho_{zx} & \rho_{zy} & \rho_{zz} \end{bmatrix} \begin{bmatrix} J_x \\ J_y \\ J_z \end{bmatrix} \tag{4.1}$$

The electrical current density $\bar{J}$ represents the amount of the charges per unit time that flows through a unit area and its unit is A/m^2, where A is Amperes and corresponds to $6.241509074x10^{18}$ electrons worth of charge moving past a point in a second or 1 Coulomb of charge per second. The electric field $\bar{E}$ originates from electric charges and time-dependent electric currents and its unit is V/m or kgm^2s^{-2}/C. In the electromagnetics of solids, the Hall conductivity, the Cowling conductivity and the Pedersen conductivity as well as the dispersion effect are generally not considered. The conductivity or resistivity tensors are defined as always symmetric and positive even if they were anisotropics[147].

From this most general definition can be defined as the extrinsic material properties R or electrical resistance for a monodimensional conductor. Assuming both electrical quantities are no time-dependent, the electric field is given by voltage divided by the conductor length, i.e. $E = \frac{V}{l}$ and the current density is given by electric

current divided by cross-sectional area, i.e. $J = \frac{I}{A}$. Imposing the first Ohm's law, i.e. $V = RI$, the equation connects the resistivity with electrical resistance takes the form:

$$R = \rho \frac{L}{A} \tag{4.2}$$

where L is specimen length and A is the cross-sectional area of the specimen.

Once the electrical resistance is defined, the piezoresistivity phenomenon can be introduced. The piezoresistive effect is a change in electrical resistivity in the function of external mechanical strain applied to a conductor material. The Piezoresistivity Factor, i.e. PF, is expressed as follows

$$PF = \frac{\frac{d\rho}{\rho}}{\varepsilon} \tag{4.3}$$

Actually, the electrical resistivity variation is challenging to measure experimentally. Electrical resistance is easier either to measure and manage than electrical resistivity. Therefore, the Gauge Factor, i.e. GF, is usually used to evaluate the piezoresistive effects and it takes the following form

$$GF = \frac{\frac{dR}{R}}{\varepsilon} \tag{4.4}$$

Therefore, the strain of conductor material can be calculated by monitoring electrical resistance at its edges. Conductor materials can be measure instruments and the most famous are strain gauges.

As the equation4.4 dictates, the GF is a function of geometric and constitutive relationship. Thus, it is a need to split the effects due to mechanics and electrical effects[148]. Applying the natural logarithms to equation4.2

$$\log R = \log \rho + \log L - \log A = \log \rho + \log l - \log (bw) = \log \rho + \log l - \log w - \log b \tag{4.5}$$

where l is the conduct length, b and w is the cross-sectional conductor sizes. Then, the equation4.5 is differentiated to provide information about how the change in resistance relates in geometrical or electrical features

$$\frac{dR}{R} = \frac{d\rho}{\rho} + \frac{dl}{l} - \frac{db}{b} - \frac{dw}{w} \tag{4.6}$$

In addition, it is supposed the conductor is an isotropic homogeneous material and it is undergoing a monoaxial stress state, so the strain field can be written as follows

$$\frac{dl}{l} = \varepsilon \qquad \frac{db}{b} = \frac{dw}{w} = -\nu\varepsilon \tag{4.7}$$

Consequently, the gauge factor is re-written imposing the constitutive, i.e. equa-

tion4.7, and the change in resistance, i.e. equation4.7 relationship

$$GF = \frac{d\rho}{\rho}\frac{1}{\varepsilon} + 1 + 2\nu = PF + 1 + 2\nu \tag{4.8}$$

The geometrical and electrical contributions are now clear from the equation4.8; hence, the geometrical contributions dictate a constant gauge factor depending on Poisson's ratio whereas the electrical contributes dictate a gauge factor depending on the material properties[149, 150]. According to equation4.8, it is also possible to define 3 kinds of materials based on piezoresistive behaviour:

- Semiconductor materials: the change in electrical resistivity is extremely non-linear so $GF = \frac{PF}{\varepsilon}$. The gauge factor is dependent on the strain sign applied and it can achieve giant piezoresistive behaviour.
- Conductor: the change in electrical resistivity is comparable to geometrical contribution so $GF = 2 + 2\nu$. The gauge factor is always constant, positive and medium-low.
- Metals: the change in electrical resistivity is zero so $GF = 1 + 2\nu$. The gauge factor is usually constant, positive and low.

Semiconductor materials reveal to be the best solution for high-sensitivity piezoresistive-based measure instrument needs. However, semiconductor usually exhibits a non-linear change in resistivity factor.

It is well-established in solid-state physics, and the electrical resistivity is composed of a 3x3 tensor. Moreover, quite all conductive materials exhibit diagonal resistivity tensors, i.e. it is always possible finding a coordinate system that makes the tensor diagonal. The nonlinear piezoresistive effects change the tensor components' values, increasing or reducing the overall conductor electrical resistivity. Therefore, the nonlinear resistivity tensor is expressed as follows

$$\bar{\bar{\rho}} = \begin{bmatrix} \rho_1^0 & 0 & 0 \\ 0 & \rho_2^0 & 0 \\ 0 & 0 & \rho_3^0 \end{bmatrix} + \begin{bmatrix} \Delta\rho_{11} & \Delta\rho_{12} & \Delta\rho_{13} \\ \Delta\rho_{21} & \Delta\rho_{22} & \Delta\rho_{23} \\ \Delta\rho_{31} & \Delta\rho_{32} & \Delta\rho_{33} \end{bmatrix} \tag{4.9}$$

where $\rho_{i,j}^0$ is the resistivity at zero loading and $\Delta\rho_{i,j}$ is the change in electrical resistivity, i.e. $\Delta\rho_{i,j} = \rho_{i,j} - \rho_{i,j}^0$. The tensor is re-written dividing all terms per the electrical resistivity at zero loading, so the electrical resistivity takes the following form

$$\bar{\bar{\rho}} = \left[\bar{\bar{I}} + \bar{\bar{r}}\right] \rho^0 \tag{4.10}$$

The tensor results easier to be visualized and managed once completely developed,

namely

$$\bar{\bar{\rho}} = \begin{bmatrix} 1 & 0 & 0 \\ 0 & 1 & 0 \\ 0 & 0 & 1 \end{bmatrix} \begin{bmatrix} \rho_1^0 \\ \rho_2^0 \\ \rho_3^0 \end{bmatrix} + \begin{bmatrix} r_{11} & r_{12} & r_{13} \\ r_{21} & r_{22} & r_{23} \\ r_{31} & r_{32} & r_{33} \end{bmatrix} \begin{bmatrix} \rho_1^0 \\ \rho_2^0 \\ \rho_3^0 \end{bmatrix} \tag{4.11}$$

where $r_{i,j} = \frac{\rho_{i,j} - \rho_{i,j}^0}{\rho_{i,j}^0}$ and they coincide with the differentiation of electrical resistivity, i.e. $r_{i,j} = \frac{d\rho_{i,j}}{\rho_{i,j}}$. In this study, the tensor $\bar{\bar{r}}$ is called the piezoresistance tensor. Thanks to this visualization it is possible to figure out anisotropy phenomena due to external loading.

In order to model the piezoresistivity effects it needs to introduce a relationship that connects the change in electrical resistivity with the external loadings [151]. In literature, physics dictates a strong connection between stress and piezoresistance. For example, the conductive dopant materials dispersed into a composite material matrix get closer once the compression loading is applied. The conductive paths connect fillers inside the matrix to become shorter and, thus the conductivity higher. Therefore, the microstructure governates the change in resistivity. The relationship between stress components and piezoresistance tensor takes the following form

$$\bar{r} = \bar{\bar{\Pi}}\bar{\sigma} \tag{4.12}$$

where Π is the piezoresistive stress matrix and it connects stress to piezoresistance as well as the constitutive matrix in solids does. The tensor results easier to be visualized and managed once completely developed, namely

$$\begin{bmatrix} r_{11} \\ r_{22} \\ r_{33} \\ r_{23} \\ r_{13} \\ r_{12} \end{bmatrix} = \begin{bmatrix} \Pi_{11} & \Pi_{12} & \Pi_{13} & \Pi_{14} & \Pi_{15} & \Pi_{16} \\ \Pi_{21} & \Pi_{22} & \Pi_{23} & \Pi_{24} & \Pi_{25} & \Pi_{26} \\ \Pi_{31} & \Pi_{32} & \Pi_{33} & \Pi_{34} & \Pi_{35} & \Pi_{36} \\ \Pi_{41} & \Pi_{42} & \Pi_{43} & \Pi_{44} & \Pi_{45} & \Pi_{46} \\ \Pi_{51} & \Pi_{52} & \Pi_{53} & \Pi_{54} & \Pi_{55} & \Pi_{56} \\ \Pi_{61} & \Pi_{62} & \Pi_{63} & \Pi_{64} & \Pi_{65} & \Pi_{66} \end{bmatrix} \begin{bmatrix} \sigma_{11} \\ \sigma_{22} \\ \sigma_{33} \\ \sigma_{23} \\ \sigma_{13} \\ \sigma_{12} \end{bmatrix} \tag{4.13}$$

where the $\Pi_{i,j}$ is the piezoresistive stress components.

The piezoresistive stress matrix can be manipulated to ensure also a relationship with strain. In the linear elastic stage, the piezoresistive strain matrix is defined according to the constitutive material matrix, namely

$$\bar{r} = \bar{\bar{\Pi}}\bar{\sigma} = \bar{\bar{\Pi}}\bar{\bar{C}}\bar{\varepsilon} = \bar{\bar{\Psi}}\bar{\varepsilon} \tag{4.14}$$

where the Ψ is the piezoresistive strain matrix and C is the stiffness matrix.

The nonlinear piezoresistive behaviour of a generic metamaterials is discussed. The stiffness matrix for a generic metamaterials is usually defined orthotropic so it is imposed in equation 4.14. Thus, the piezoresistive strain matrix is written as

follow

$$\bar{\bar{\Psi}} = \begin{bmatrix} \Pi_{11} & \Pi_{12} & \Pi_{13} & \Pi_{14} & \Pi_{15} & \Pi_{16} \\ \Pi_{21} & \Pi_{22} & \Pi_{23} & \Pi_{24} & \Pi_{25} & \Pi_{26} \\ \Pi_{31} & \Pi_{32} & \Pi_{33} & \Pi_{34} & \Pi_{35} & \Pi_{36} \\ \Pi_{41} & \Pi_{42} & \Pi_{43} & \Pi_{44} & \Pi_{45} & \Pi_{46} \\ \Pi_{51} & \Pi_{52} & \Pi_{53} & \Pi_{54} & \Pi_{55} & \Pi_{56} \\ \Pi_{61} & \Pi_{62} & \Pi_{63} & \Pi_{64} & \Pi_{65} & \Pi_{66} \end{bmatrix} \begin{bmatrix} C_{11} & C_{12} & C_{13} & 0 & 0 & 0 \\ C_{21} & C_{22} & C_{23} & 0 & 0 & 0 \\ C_{31} & C_{32} & C_{33} & 0 & 0 & 0 \\ 0 & 0 & 0 & C_{44} & 0 & 0 \\ 0 & 0 & 0 & 0 & C_{55} & 0 \\ 0 & 0 & 0 & 0 & 0 & C_{66} \end{bmatrix} \tag{4.15}$$

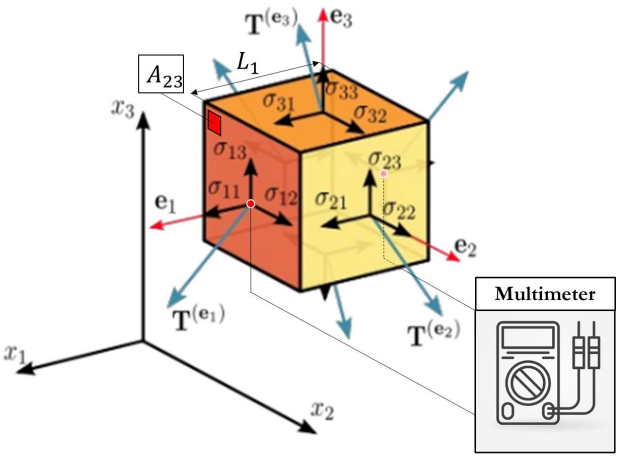

Figure 4.2: Sketch of piezoresistive tensor on elementary conductor cube.

The nonlinear resistivity is evaluated along the first principal direction as shown in figure4.2. The electrical resistance is dictated by the traditional equation4.2. The electrical resistance along the first direction becomes:

$$R_{11} = \rho_{11} \frac{L_1}{A_{23}} = \left[\rho_1^0 \left(1 + r_{11}\right)\right] \frac{L_1}{A_{23}} \tag{4.16}$$

where the L_1 is the metamaterial length and A_{23} is the cross-sectional area. To measure R_{11} the experimental test must be set up with a multimeter along the first principal direction, i.e. the pin must be connected to the up and lower side of the metamaterial. The length L_1 measures the long distance between the multimeter pins. The A_{23} is the area where the pins touch as shown in figure4.2. According to the piezoresistive strain matrix, the piezoresistance coefficient r_{11} is calculated as follow

$$r_{11} = \left[\Psi_{11}\Psi_{12}\Psi_{13}\Psi_{14}\Psi_{15}\Psi_{16}\right] \begin{bmatrix} \varepsilon_{11} \\ \varepsilon_{22} \\ \varepsilon_{33} \\ \varepsilon_{23} \\ \varepsilon_{13} \\ \varepsilon_{12} \end{bmatrix} \tag{4.17}$$

where

$$\begin{aligned}
\Psi_{11} &= \Pi_{11}C_{11} + \Pi_{12}C_{21} + \Pi_{13}C_{31} \\
\Psi_{12} &= \Pi_{11}C_{12} + \Pi_{12}C_{22} + \Pi_{13}C_{32} \\
\Psi_{13} &= \Pi_{11}C_{13} + \Pi_{12}C_{23} + \Pi_{13}C_{33} \\
\Psi_{14} &= \Pi_{14}C_{44} \\
\Psi_{15} &= \Pi_{15}C_{55} \\
\Psi_{16} &= \Pi_{16}C_{66}
\end{aligned} \tag{4.18}$$

The change in electrical resistance along the first principal direction is written following the geometrical relationship. Thus, the equation4.6 assumes the following form:

$$\frac{dR_{11}}{R_{11}^0} = \frac{d\rho_{11}}{\rho_1^0} + \varepsilon_{11} - \varepsilon_{22} - \varepsilon_{33} \tag{4.19}$$

where the change in electrical resistivity coincides with the first term in piezoresistance matrix r_{11}

$$\frac{d\rho_{11}}{\rho_1^0} = \frac{\rho_{11} - \rho_1^0}{\rho_1^0} = \frac{\rho_1^0\,(1 + r_{11}) - \rho_1^0}{\rho_1^0} = r_{11} \tag{4.20}$$

The change in electrical resistance along the first principal direction can be obtained imposing the extended form of r_{11} dictates from equation4.17 into the equation4.19. Thus, the complete form of electrical resistance along the first principal direction is written as follow

$$\frac{dR_{11}}{R_{11}^0} = (\Psi_{11}+1)\varepsilon_{11} + (\Psi_{12}-1)\varepsilon_{22} + (\Psi_{13}-1)\varepsilon_{33} + \Psi_{14}\varepsilon_{23} + \Psi_{15}\varepsilon_{13} + \Psi_{16}\varepsilon_{12} \tag{4.21}$$

The equation4.21 can be reffered to a generic orthotropic material in which the transversal strains are defined thorugh the respective Poisson's ratio, i.e. $\frac{\varepsilon_{22}}{\varepsilon_{11}} = -\nu_{12}$ and $\frac{\varepsilon_{33}}{\varepsilon_{11}} = -\nu_{13}$. Therefore, the complete change in electrical resistance along the first principal direction for an orthotropic metamaterials is defines as follow

$$\frac{dR_{11}}{R_{11}^0} = (\Psi_{11} - \Psi_{12}\nu_{12} - \Psi_{13}\nu_{13} + 1 + \nu_{12} + \nu_{13})\varepsilon_{11} + \Psi_{14}\varepsilon_{23} + \Psi_{15}\varepsilon_{13} + \Psi_{16}\varepsilon_{12} \tag{4.22}$$

The equation4.22 denotes the strain aligned to the electrical resistance measurement plays the main contribute thanks to constant 1 and Ψ_{11} in which the sign usually disagrees with the strain sign. In fact, a conductive composite material usually exhibits a decrease in electrical resistance due to conductive path curtailment. Thus, the Ψ_{11} has to be defined as positive in opposition to negative strain. In addition, the transversal strains play a beneficial effect when the metamaterial is rubbery instead of auxetic. However, equation4.22 denotes an increase of benefit effects when the Ψ_{12} and Ψ_{13} are defined negative. The shear strain affects the electrical resistance if and only if the metamaterial exhibits piezoresistive effects.

Following the piezoresistivity theory, it can be defined the piezoresistivity and gauge factor along the first principal direction of a generic metamaterial from the equation4.3 and equation4.4, respectively.

$$PF_{11} = \frac{\frac{d\rho_{11}}{\rho_{11}^0}}{\varepsilon_{11}} = \Psi_{11} - \Psi_{12}\nu_{12} - \Psi_{13}\nu_{13} + \Psi_{14}\frac{\varepsilon_{23}}{\varepsilon_{11}} + \Psi_{15}\frac{\varepsilon_{13}}{\varepsilon_{11}} + \Psi_{16}\frac{\varepsilon_{12}}{\varepsilon_{11}} \tag{4.23}$$

$$GF_{11} = \frac{\frac{dR_{11}}{R_{11}^0}}{\varepsilon_{11}} = PF_{11} + 1 + \nu_{12} + \nu_{13} \tag{4.24}$$

Writing the gauge factor in this form clearly shows how the geometrical and constitutive contributes to its magnitude. Equation4.24 denotes the shear strain affects the GF linearly. That means, the GF can increase or decrease by shear strain effects once a stable compression strain is reached. A GF sensitive to shear strain is extremely rare in metals and not common in other materials in nature. If the GF was sensible to shear strain, it could be possible to figure out the shear strain sign and thus predict the metamaterials transversal direction in which it is deforming.

It is relevant making a comparison between three stress states on the conductor in order to define the higher gauge factor: monoaxial stress, monoaxial strain and pure shear stress states. It is assumed the electrical resistance is measured along the first principal direction, as figure4.2 shows. The gauge factors take the following forms:

$$\begin{aligned} GF_\sigma &= \frac{\frac{dR_{11}}{R_{11}^0}}{\varepsilon_{11}} = 1 + \nu_{12} + \nu_{13} + \Psi_{11} - \Psi_{12}\nu_{12} - \Psi_{13}\nu_{13} \\ GF_\varepsilon &= \frac{\frac{dR_{11}}{R_{11}^0}}{\varepsilon_{11}} = 1 + \Psi_{11} \\ GF_\tau &= \frac{\frac{dR_{11}}{R_{11}^0}}{\varepsilon_{12}} = \Psi_{16} \end{aligned} \tag{4.25}$$

where GF_σ dictates the monoaxial stress, GF_ε monoaxial strain and GF_τ pure shear stress states. Evaluating all gauge factors the monoaxial stress state turns out to be the best solution. The electrical resistance is a function of conductor length and cross-section, so a constant cross-sectional area as in pure shear strain and monoaxial strain removes geometrical contributions in gauge factor. Both gauge factors are dependent on the material piezoresistive effect. No piezoresistive materials result in having gauge factor measurement ineffective.

A comparison between extended to simplified theory is usually done in analytical modelling. Therefore, if the metamaterials is assumed to be ineffective by constitutive piezoresistive effects, i.e. $\Psi_{11} = \Psi_{12} = \Psi_{13} = \Psi_{14} = \Psi_{15} = \Psi_{16} = 0$, and isotropic, the equation4.22 takes the well-know form, i.e. equation4.8,

$$\frac{dR_{11}}{R_{11}^0} = (1 + 2\nu)\varepsilon_{11} \tag{4.26}$$

Thus, the gauge factor takes the same relationship defined before, i.e. equation4.8

$$GF_{11} = \frac{dR_{11}}{R_{11}^0}\frac{1}{\varepsilon_{11}} = 1 + 2\nu \tag{4.27}$$

4.3 Piezoresitive Model Based on Finite Element Analysis

In literature, multi-physics softwares like Comosol are able to achieve multiphysics behaviour in electromagnetism, optic, acoustics, and mechanics. However, these kinds of software do have not a long history in mechanical fields. Traditional software such as Abaqus, Nastran, and Ansys are well established in the research field once a complex mechanical behaviour of material needs to be modelled. They are usually robust and able to solve large nonlinear problems, implement nonlinear constitutive models, and implement customizable external subroutines. For example, modelling cellular materials with the same numerical model introduced in the previous section is impossible in other multi-physics software. Therefore, in this study Abaqus software was used to model the piezoresistive behaviour of conductive metamaterials.

Abaqus suites enable multi-physics simulation but they are limited compared to other software. Abaqus suites are able to carry out electrical simulations in which the electrical conductivity can be imposed on the constitutive material model. However, the electrical suite is not able to carry out time-dependent or strain-dependent simulations. There was a need to work around this issue or limit. Abaqus has got a well-established temperature-dependent suite which enables complex thermal simulations. Physics dictates an analogy between thermal and electrical equations and thus between thermal and electrical resistance. Therefore, physics aided to overtake the issue. Although thermal simulation has to be defined correctly inside Abaqus the piezoresistivity or the change in electrical resistivity in solids can be associated with a change in thermal resistivity. In other words, in this study, the Abaqus solver has been exploited to solve thermal equations without Abaqus knowing it was an electrical simulation.

Before moving on to metamaterials modelling, it is essential to introduce the limitation of this analogy and the assumptions underlying this strategy. From physics, the thermal conductivity, i.e. κ, behaviour is dictated by Fourier's law in which the heat is transferred from a hotter to a colder zone by conduction phenomena in conductor material. Fourier's law defines the equation for thermal conductivity is

$$\bar{\bar{\kappa}} = -\frac{\bar{q}}{\nabla T} \Leftrightarrow \begin{bmatrix} q_x \\ q_y \\ q_z \end{bmatrix} = - \begin{bmatrix} \kappa_{xx} & \kappa_{xy} & \kappa_{xz} \\ \kappa_{yx} & \kappa_{yy} & \kappa_{yz} \\ \kappa_{zx} & \kappa_{zy} & \kappa_{zz} \end{bmatrix} \begin{bmatrix} \frac{\partial T_x}{\partial x} \\ \frac{\partial T_y}{\partial y} \\ \frac{\partial T_z}{\partial z} \end{bmatrix} \tag{4.28}$$

where T_i is the temperature and q_i is the heat flux along the i principal direction in solid. The heat flux is usually expressed with unit W/m^2, the temperature in K

and thermal conductivity in $Wm^{-}1/K$.

As discussed before, assuming thermal quantities are no time-dependent, the thermal field is given by finite temperature difference divided by conductor length (from hotter to colder zone), i.e. $\frac{\partial T_x}{\partial x} = \frac{\Delta T}{l}$. The heat flux is given by conductive heat transferred divided by cross-sectional are, i.e. $q = \frac{Q}{A}$. Therefore, the temperature transferred through a monodimensional conductor is written as follows

$$\frac{Q}{A} = -\kappa \frac{\Delta T}{l} \tag{4.29}$$

Consequently, the thermal resistance terms is introduced thanks to analogy with Ohm's second law, namely

$$\Delta T = -\lambda \frac{l}{A} Q = R_T Q \tag{4.30}$$

where λ is the inverse of κ and it is defined thermal resistivity. The R_T is the thermal resistance defined as $R_T = -\lambda \frac{l}{A}$ and the unit is K/W. The thermal resistance results are analogous to electrical resistance. That means the equations governing the conductivity phenomena in terms of electrical or thermal are the same but only under time-independent conditions. Thus, the analogy can be easily written as follow

$$V = RI \Leftrightarrow \Delta T = R_T Q \tag{4.31}$$

Once the governing equations and analogy are introduced and figured out, the Abaqus simulation is managed through an implicit solver imposing a steady-state thermal-displacement step. The need to use steady-state conditions is mandatory. There is another crucial issue on this topic. In thermal dynamics simulation temperature transfer as well as heat transfer are governed by thermal diffusivity. Thermal diffusivity is a function of density and specific heat and quantifies the thermal inertia of a material. For example, in copper, the thermal diffusivity is about 1.17 cm^2/s.

The electrical inertia is not well established as the thermal one. In electromagnetism, there are three kinds of speed: electron velocity, drift velocity, and signal velocity. In this analogy, the signal velocity has to be compared to thermal diffusivity on the thermal field. The signal velocity is the speed at which the electromagnetic effects travel down solids or wire. For example, in copper, the signal velocity is about 300000 km/s, i.e. about the speed of light. This statement is compatible with thermal diffusivity which is the speed at which the heat spreads through solids. That means, the thermal effects should occur in about the same magnitude order of thermal diffusivity.

Furthermore, mechanics phenomena affect changes in temperature such as damage, breaks or plasticity. The release of energy in failure generates an increase in temperature as well as plastic deformation. Therefore, it is absolutely avoided to make thermal-electrical analogies in thermal dynamics simulations in which the steady-state condition is not established.

Moving forward to numerical modelling, the first simulation aimed to validate the gauge factor in homogeneous isotropic solids. The numerical modelling should confirm the gauge factor follows only geometrical contributions as equation 4.27 defines. An axisymmetric simulation is carried out in which the material model has the thermo/electric-mechanics properties listed in tabel 4.1. It is assumed a rubbery material with a thermal/electrical resistivity of ρ. Figure 4.3 shows a sketch of the

Table 4.1: Constitutive parameters of cylinder in piezoresistive numerical simulation

E	ν	ρ	R^0	ε	R	GF_{FEA}	GF
$[MPa]$	-	$[\Omega mm]$	$[\Omega]$	$[mm/mm]$	$[\Omega]$	-	-
3368	0.3956	1000	127.324	-0.01	125.041	1.7927	1.7912

numerical simulation procedure in Abaqus. The simulation is articulated in two steps:

- First step: steady-state thermal loading. A temperature of dummy 10 $°C$ is imposed at the top edge of the cylinder and 0 $°C$ at the bottom edge. Only vertical displacements are avoided at the bottom edge of the cylinder to guarantee the area restrictions. This step simulates constant thermal differences between the edges of the cylinder as it was an electrical potential difference;
- Second step: steady-state thermal-displacement loading. The boundary conditions remain the same. Compression loading is imposed at the top edge of the cylinder. Also, in this case, the transversal deformation is enabled. The cylinder is compressed from the top to the bottom along its axis and the temperature difference at the external edges is stable.

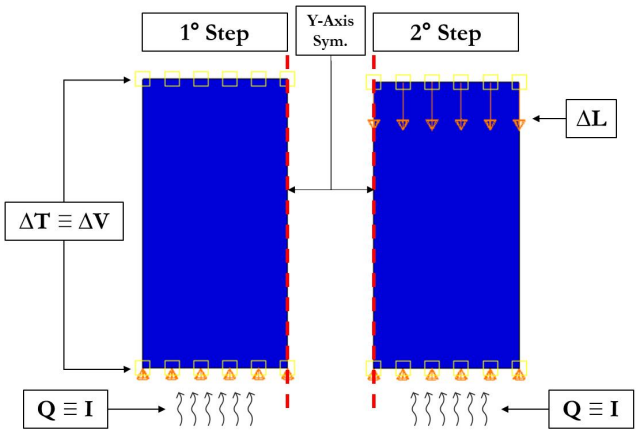

Figure 4.3: Sketch of numerical simulation procedure to predict piezoresistivity of bulk material in Abaqus.

To measure the changes in thermal resistance the heat fluxes information needs. The heat flux aligned with the cylinder axis is extrapolated from the top nodes

it is the same in the bottom nodes due to steady-state condition. The heat flux is constant at the top nodes due to homogeneous monoaxial compression stress. In inhomogeneous heat flux conditions, the standard methodology is connecting the macroscopic to discontinuous quantity through volume averaging or homogenization technique[152], namely

$$\bar{q}_{i,j} = \frac{1}{V}\int_S q_{i,j} dV \tag{4.32}$$

The heat flux is multiplied by cylinder area to obtain the heat transferred by the temperature difference, i.e. Q. The gauge factor is calculated by the equation4.4 and called GF_{FEA}. The GF_{FEA} is compared with the theoretical GF by the equation4.27. All values are listed in table4.1. The GF obtained by means of numerical simulation predict the change in resistivity due to geometrical relationship. That means the afforded strategy can be applied to measure the GF of complex structure.

Seen them already, four different honeycombs geometry with relative density $\bar{\rho} = 30\%$ were studiated: hexagonal, S-shape, I-shape, and re-entrant. In literature, none articles discuss the homogenized electrical properties of metamaterials have been found yet. Otherwise, thermal properties homogenization through RVE analysis is common in heat transfer applications[153]. In thermal RVE analysis it is crucial investigates the porosity effects on the heat transfer porperties because of air inside them.

Piezoresisitve simulation was carried out on unit-cell thorugh RVE analysis imposin PBC to evaluate how the piezoresistive theory works coupled with homogenization theory. The numerical simulation procedure is the same introduced before and, also in this case, a sketch of numerical simulation procedure in Abaqus is shown in figure4.4. Working on honeycombs structure the plain strain condition is applied to the unit-cell topology. The material properties of solid part is assumed to have the value introduced before on cylinder simulation. The compression loading step is carried out up to about $\varepsilon = -4\%$ in order to avoid structure nonlinearities like buckling phenomenon.

Once the second step is complete, the heat fluxes were measured at the external nodes. The heat flux is multiplied by the effective area in which the electric current travel down, i.e. the ligaments thickness by the unit-cell width. Consequently, the electrical resistance is calculated as discussed before. The results are listed in table4.2 The electrical resistivity ρ_{22} needs conductor length and cross-sectional area

Table 4.2: Constitutive parameters of cylinder in piezoresistive numerical simulation

ρ_s	ν_{21}	ρ^0_{22}	R^0_{22}	ε_{22}	R_{22}	GF_{22-FEA}	GF_{22}
$[\Omega mm]$	-	$[\Omega mm]$	$[\Omega]$	$[mm/mm]$	$[\Omega]$	-	-
1000	0.246	9812.24	389.72	-0.04167	387.95	0.109	1.246

to be derived by the electrical resistance. Thus, it is defined on unit-cell envelope dimensions, i.e. the orange box depicted in figure4.4. The ρ^0_{22} is calculated assuming

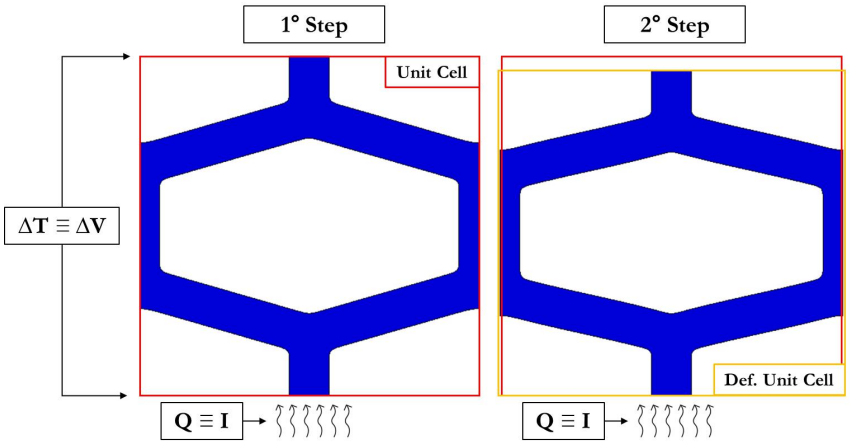

Figure 4.4: Sketch of numerical simulation procedure to predict piezoresistivity of unit-cell in Abaqus

the red box envelope, i.e. undeformed unit-cell. In RVE analysis is fundamental to refer to the metamaterial property as the associated bulk one. ρ_{22}^{0} results 9.812 times higher than bulk electrical resistivity. That means, the honeycomb structure exhibits higher resistance to electric current flow than the bulk material. Therefore, changes in unit-cell topology enable a new concept of conductive metamaterials with topology-based electrical resistivity.

The RVE analysis on hexagonal unit-cell predicts a $GF_{22-FEA} = 0.109$ whereas the analytical gauge factor predicts by imposing plain strain condition in equation4.19 $GF_{22} = 1.246$. Therefore, the RVE analysis reveals the gauge factors are inconsistent. The divergence is due to the assumption behind the gauge factor theory. In the piezoresistive theory discussed before, the base material is assumed to be homogeneous. The unit-cell topology results inhomogeneous and the electric current travels along a preferential path due to the unit-cell walls.

Moreover, the predicted numerical gauge factor $GF_{22-FEA} = 0.109$ is extremely lower than solid material. Therefore, it can affirm the hexagonal unit-cell is not sensible to change in electrical resistance. To make sensible the hexagonal structure needs the base material to have a constitutive piezoresistivity; hence, the constitutive piezoresistive contributes allow to compensate for the geometrical insensibility. Best materials these suit this peculiarity are conductive polymer or carbon-based composites. Hexagonal honeycombs based on solid metals, i.e. steel, are useless.

In this study, it is proposed a strategy to take into account the inhomogeneous distribution of solid parts inside RVE. According to the piezoresistive strain matrix, the nonlinear electrical resistivity is expressed as a function of strain as well as of stress. Thus, it is assumed the nonlinear resistivity due to unit-cell topology is compensated by those terms. The change in electrical resistance is described by the

nonlinear equation along the vertical direction, namely

$$\frac{dR_{22}}{R_{22}^0} = (\Psi_{21}-1)\varepsilon_{11} + (\Psi_{22}+1)\varepsilon_{22} + \Psi_{26}\varepsilon_{12} = (1+\Psi_{22}-\Psi_{21}\nu_{21}-\nu_{21})\varepsilon_{22} + \Psi_{26}\varepsilon_{12} \tag{4.33}$$

The terms Ψ_{22}, Ψ_{21}, and Ψ_{26} should be able to take into account the inhomogeneous piezoresistive behaviour. The Poisson's ratio is known from the stiffness matrix of metamaterials and they can be obtained from the homogenization technique on RVE. Therefore, the hexagonal piezoresistivity behaviour can be predicted by electric properties homogenization coupled with traditional mechanics.

Through electric properties homogenization, the piezoresistive strain matrix coefficients Ψ_{22}, Ψ_{21}, and Ψ_{26} can be defined. The numerical procedure disassembles the contributes of each coefficient carrying out three piezoresistive RVE analyses. The coefficients can be defined as follow:

$$\begin{aligned} \Psi_{21} &= \frac{dR_{22}}{R_{22}^0}\frac{1}{\varepsilon_{11}} + 1 \quad & \varepsilon_{22} = \varepsilon_{12} = 0 \\ \Psi_{22} &= \frac{dR_{22}}{R_{22}^0}\frac{1}{\varepsilon_{22}} - 1 \quad & \varepsilon_{11} = \varepsilon_{12} = 0 \\ \Psi_{26} &= \frac{dR_{22}}{R_{22}^0}\frac{1}{\varepsilon_{12}} \quad & \varepsilon_{11} = \varepsilon_{22} = 0 \end{aligned} \tag{4.34}$$

The FE analysis of RVE with PBC is carried out following the scheme described in figure4.4. The electrical resistance, i.e. R_{22}, is measured along the vertical direction, i.e. 2nd principal direction or vertical direction. The finite strain is imposed in each of the three FEA according to the strain coefficient to decouple. For example, the Ψ_{21} coefficient was determined avoiding vertical, i.e. ε_{22}, and shear, i.e. ε_{12}, strain on unit-cell. The compression loading was imposed through horizontal strain, i.e. ε_{11}. Once the horizontal strain is applied, the electrical resistance is measured along the 2nd direction through the same procedure based on measuring the effective heat from heat flux at the external nodes. All three directions are evaluated according to the boundary conditions in equations4.34. Table4.3 shows the obtained numerical values.

Table 4.3: FEA procedure to measure piezoresistive strain matrix coefficients

ρ_{22}^0 $[\Omega mm]$	R_{22}^0 $[\Omega]$	ε_{11} $[mm/mm]$	ε_{22} $[mm/mm]$	ε_{12} $[mm/mm]$	R_{22} $[\Omega]$
9812.24	389.72	0.0083	0	0	392.77
9812.24	389.72	0	-0.0417	0	384.38
9812.24	389.72	0	0	0.0166	389.73

The FEA on hexagonal unit-cell results piezoresistive strain matrix coefficients as follow

$$\Psi_{21} = 1.9379 \qquad \Psi_{22} = -0.67113 \qquad \Psi_{26} = 0.00568 \tag{4.35}$$

Substituting the calculated strain matrix coefficiens in equation4.35 in the general change in resistance behaviour of macroscopic conductive metamaterial, i.e. equation4.33; the theoretical gauge factor GF_{22} is updated to GF_{22-n} as follow

$$GF_{22-n} = \frac{dR_{22}}{R_{22}^0}\frac{1}{\varepsilon_{22}} = 1 + \Psi_{22} - \Psi_{21}\nu_{21} - \nu_{21} + \frac{\Psi_{26}\varepsilon_{12}}{\varepsilon_{22}} = 0.102 \tag{4.36}$$

GF_{22-n} is now consitent with the numerical prediction GF_{22-FEA}. The homogenization procedure coupled to FEA on RVE with PBC results a effective tool to calculate the piezoresistive strain matrix coefficients able to describe the theoretical gauge factor for an inhomogenues solid starting from the homogeneus solid theory.

Once this strategy is confirmed by numerical and analytical evidences, the piezoresistivity of different unit-cell topologies is investigated. For the sake of semplicity, only planar anisotropy is investigated. First of all, the piezoresistive strain matrix is populated following the previous procedure. For example, in hexagonal RVE the piezoresistive strain matrix takes the following form:

$$\begin{bmatrix} \Psi_{11} & \Psi_{12} & \Psi_{16} \\ \Psi_{21} & \Psi_{22} & \Psi_{26} \\ \Psi_{61} & \Psi_{62} & \Psi_{66} \end{bmatrix} = \begin{bmatrix} 0.1459 & 1.2980 & 0 \\ 1.9379 & -0.6711 & 0 \\ 0 & 0 & 0 \end{bmatrix} \tag{4.37}$$

The piezoresistive strain matrix coefficients results zero, i.e. 3rd raw and 3rd column. The shear strain in hexagonal unit-cell does not affect the resistivity alligned to principal direction. Then, the in-plane electrical resistivity is defined as follow

$$\bar{\bar{\rho}} = \begin{bmatrix} 1 & 0 \\ 0 & 1 \end{bmatrix} \begin{bmatrix} \rho_1^0 \\ \rho_2^0 \end{bmatrix} + \begin{bmatrix} r_{11} & 0 \\ 0 & r_{22} \end{bmatrix} \begin{bmatrix} \rho_1^0 \\ \rho_2^0 \end{bmatrix} \tag{4.38}$$

The r_{12} is zero due to the 3rd row of the piezoresistive strain matrix being zero. Thus, the principal directions coincide with the horizontal and vertical directions in the hexagonal unit-cell. First of all, the resistivity at zero loading is discussed. The figure4.5a shows the resistivity at zero loading of the 4 unit-cell topologies with relative density $\bar{\rho} = 30\%$: re-entrant, I-shape, S-shape, and hexagonal. The in-plane anisotropic behaviour is visualized through a spherical coordinate system, the mathematical procedure is well-defined in these papers [154, 155]. Figure4.5a reveals unti-cell can exhibit anisotropic electrical resistivity. Only the I-shape has got an isotropic electrical resistivity. That means the conductive path inside the unit-cell is symmetric whereas all other cases do not. Hexagonal unit-cell exhibits the highest electrical conductivity in both directions. This behaviour might be connected to the rubbery behaviour. The auxeticity in unit-cells is allowed by the topology. I-shape, S-shape, and re-entrant are designed to fold cell walls once the structures are compressed so they are more articulated than simple hexagonal unit-cell. Otherwise, the hexagonal exhibits the highest stiffnes so the solid part must be established on the shortest path that connects opposite edges.

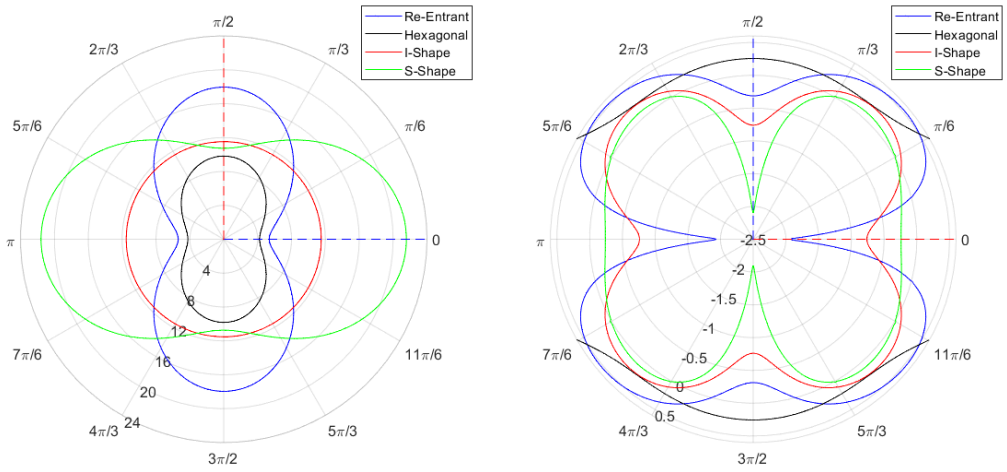

(a) (b)

Figure 4.5: Visualizing elastic and electric anisotropy. (a) Electrical resistivity at zero loading. (b) Poisson's ratio

Figure4.6 shows the in-plane Young's modulus of the 2D structures. The stiffness is adimensionalized by its own maximum value; the scales are different and not comparable. Comparing the principal electrical resistivity directions with the principal stiffness direction, it is clear that stiffness plays the main role in electrical resistivity. The higher the stiffness and higher is electrical conductivity. As introduced before, a stiffer unit-cell needs the solid part established along the shortest path that connects two opposite directions. However, this statement is not valid at all. The I-shape has got lower electrical resistance than the re-entrant although the stiffness is lower. Therefore, the ligaments are well aligned to vertical or horizontal directions but the bending-dominated behaviour of the I-shape leads to lower stiffness than re-entrant.

In order to evaluate the in-plane nonlinear piezoresistivity behaviour of all 2D structures, it is needed the in-plane Poisson's ratio, as equation4.17 and equation4.38 dictate. The in-plane Poisson's ratio of all 4 2D structures is shown in figure4.5b. Poisson's ratio as well as Young's modulus was obtained carrying out the homogenization of RVE's with PBC in which the solid part has got the material properties listed in table4.1. From the homogenization, the associated compliance matrix was obtained. To visualize Poisson's ratio anisotropy, as well as Young's modulus from the stiffness or compliance matrix, needs a technical realisation. It is able to identify the characteristic parameters of the fourth-order elasticity tensor, which is classified by three-dimensional symmetry groups. Nordmann et al. deeply discussed the mathematical relationship to visualize in spherical coordinates the anisotropy of bulk, Young, shear modulus as well as Poisson's ratio[156, 157].

The nonlinear electric resistivity in principal directions are defined in extend ver-

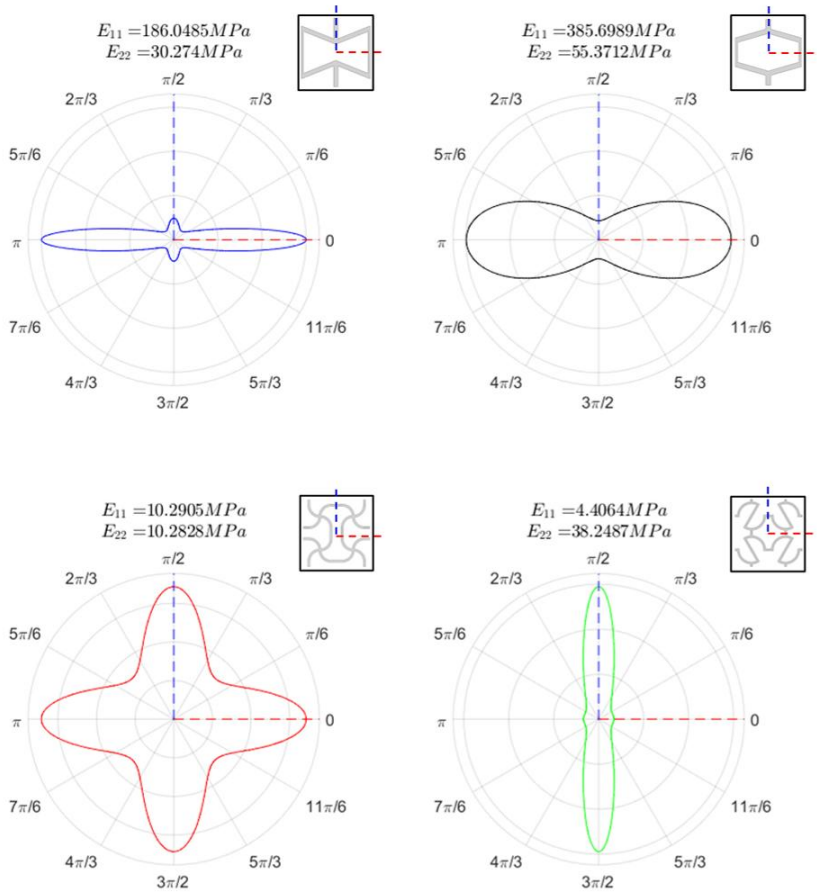

Figure 4.6: Visualizing elastic anisotropy: Young's modulus.

sion from equation4.17 and equation4.38 as follow

$$\begin{aligned} \rho_{11} &= \rho_{11}^{0}\left[1+\left(\Psi_{11}-\Psi_{12}\nu_{12}\right)\varepsilon_{11}\right] \\ \rho_{22} &= \rho_{22}^{0}\left[1+\left(\Psi_{22}-\Psi_{21}\nu_{21}\right)\varepsilon_{22}\right] \end{aligned} \tag{4.39}$$

Taking into advantages of spherical coordinate system and in-plane Poisson's ratio, the directional in-plane electrical conductivity becomes

$$\rho(\theta)=\rho_{11}^{0}\left[1+\left(\Psi_{11}-\Psi_{12}\nu(\theta)\right)\varepsilon_{11}\right]cos^{2}(\theta)+\rho_{22}^{0}\left[1+\left(\Psi_{21}\nu(\theta+\pi/2)-\Psi_{22}\right)\nu(\theta)\varepsilon_{11}\right]sin^{2}(\theta) \tag{4.40}$$

The directional in-plane electrical conductivity is a trivial function of strain. It is assumed the $\rho(\theta)$ is a function of one principal direction to visualize the nonlinear trend after compression or tensile loading. The transversal strain is calculated through geometric consideration enabled by Poisson's ratio. The nonlinear electrical resistivity behaviour of the 4 planar unit-cell is depicted by figure4.7, where the scale of the polar plots is adimensionalized by its own polar plot maximum value. The polar plots allow us to figure out how the geometrical shape affects the electrical

resistivity in three conditions: compression, tensile, and zero loadings. The loading conditions are generated by imposing a positive or negative strain inside the $\rho(\theta)$. The I-shape shows a constant electrical resistivity during deformations, thus the shape is not geometrically piezoresistive. On the contrary, the hexagonal structure shows a higher change in resistivity.

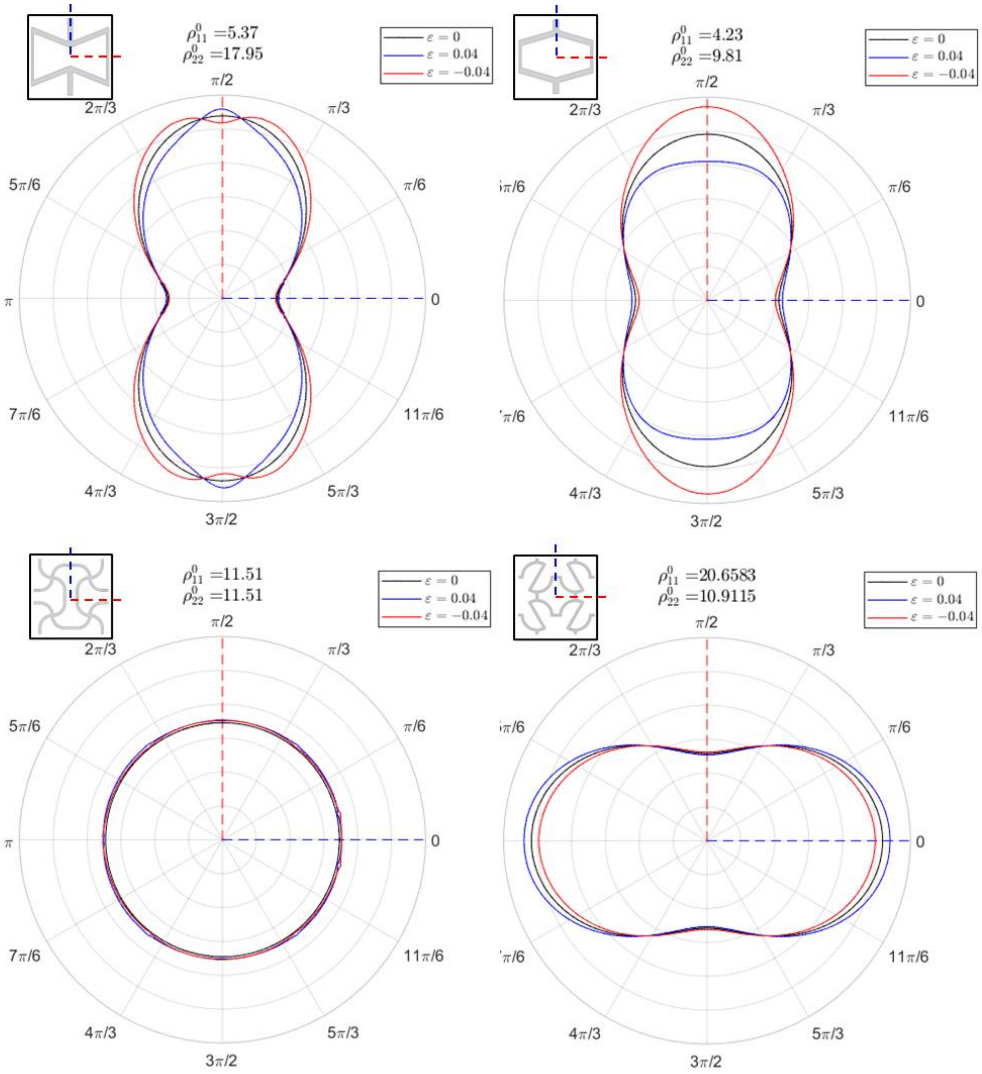

Figure 4.7: Visualizing nonlinear electrical anisotropy: electrical resistivity.

Hexagonal, re-entrant and S-shape unit-cells show a re-shape of electrical resistivity at zero loading once they are deformed. It is interesting the sign of electrical resistivity change. The auxetic structures show a resistivity decrease when compressed whereas the hexagonal one shows a resistivity increase. That geometrical behaviour is especially useful when a constitutive piezoresistivity of a solid is introduced. Both contributions would reduce the electrical resistivity under compression loading, thus the gauge factor should be higher.

4.3.1 Nonlinear Piezoresistive Numerical Model

Conductive materials usually exhibit constitutive piezoresistivity so a complete piezoresistivity phenomenon needs to be investigated. The numerical procedure introduced before was updated to take into account constitutive piezoresistivity. Abaqus is not able to model nonlinear thermal resistivity (electrical resistivity under thermal-electric analogy). However, Abaqus allows the introduction of time-dependent or field-dependent variables through external subroutines based on Fortran scripts. In this study, the stress field was manipulated to generate a field variable so that the Abaqus calculates the thermal resistivity according to the field variable introduced. The updated numerical simulation procedure is depicted in figure4.8.

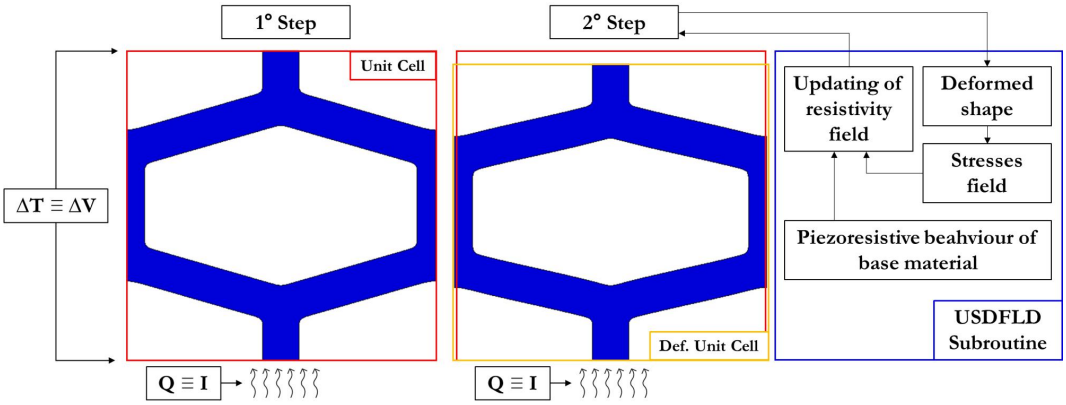

Figure 4.8: Sketch of numerical simulation procedure to predict nonlinear piezoresistivity of unit-cell in Abaqus

In detail, the numerical procedure is split into two steady-state steps: thermal and thermo-mechanical steps. The first step generates the temperature field imposing a temperature difference at the external edges as the numerical model introduced before. The second step simulates the mechanical loading. The updating consists in implementing the Abaqus subroutine in the second step. USDLF subroutine has been used to manipulate the constitutive piezoresistivity. The USDFLD updates a field variable at the end of each time increment inside the second step. The USDLFD subroutine was used to impose in each integration point a field variable. Abaqus recognizes the field variable and updates the thermal resistivity according to the field variable that finds at each integration point. Once the field variable was updated at a time increment, Abaqus performed a thermo-mechanical analysis with the updated thermal resistivities.

In this study, the first dummy piezoresistive behaviour was introduced aiming to evaluate the piezoresistive effects on metamaterials through a simple piezoresistive case. A dummy mechanical and electrical properties were introduced. Table4.4 shows the multi-physics properties of a dummy material. For the sake of semplicity piezoresistivity is supposed to be a function of Von Mises stress. In this way, the constitutive piezoresistive contribution can be clearly discussed before moving to real

material piezoresistive behaviour. The mechanical and thermal resistivity response are functions of stress as physics dictates and they are depicted in figure4.9. It was supposed a linear elastic stage up to the yielding point and a subsequent hardening phase. Meanwhile, the electrical resistivity decreases rapidly up to a yielding point (Von Mises stress) and then it changes its slope.

Table 4.4: Mechanical and electrcial resistivity response of a dummy material.

E	ν_{21}	ρ^0	σ_s	E_t	Π_{22}	Π_{22p}
$[MPa]$	-	$[\Omega mm]$	$[MPa]$	$[MPa]$	$[1/MPa]$	$[1/MPa]$
3368	0.3546	1000	50	10	-0.018	-0.09

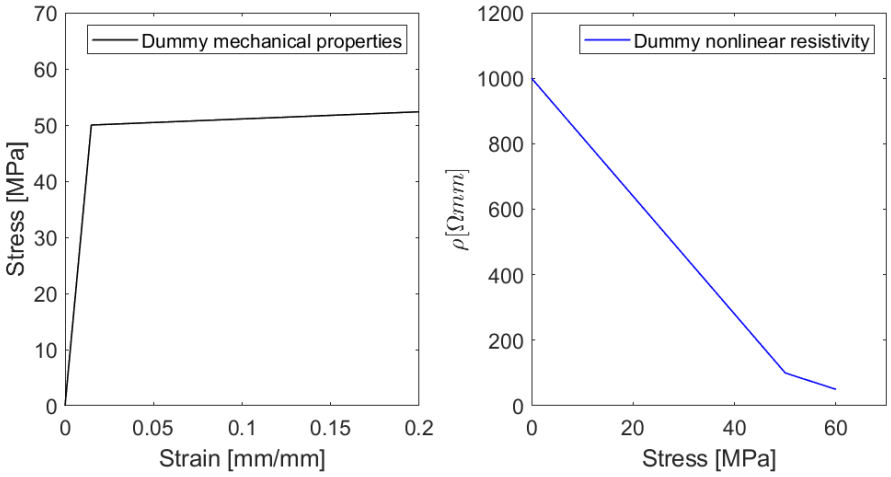

Figure 4.9: Mechanical and electrical resistivity response of a dummy material (function of Von Mises stress).

In this study, the first concept of USDLFD subroutine was implemented. As it was supposed the electrical resistivity is a function of Von Mises stress, the USDFLD extracts the Von Mises stress at each integration point and transforms them into field variables. The field variable associated with the integration points is red by Abaqus at the end of integration time. In Abaqus, the thermal conductivity in the material model is a defined function of the field variable so that Abaqus updates thermal resistivity at each integration point based on the field variable generated by USDFLD.

The FE analysis was carried out on RVE with PBC for each 2D unit-cell. Once the FEA is complete, the results are exported from Abaqus to Matlab. Through a Matlab code, the displacements and forces are transformed in stress and strains and plotted in figure4.10a. The heat flux is homogenized through equation4.32 and the thermal resistance history is calculated. According to the thermal-electrical analogy resistance as well as the electrical resistance have unit Ω. From the electrical resistance histories, the change in resistances are calculated and they are depicted in figure4.10b for each unit-cell topology.

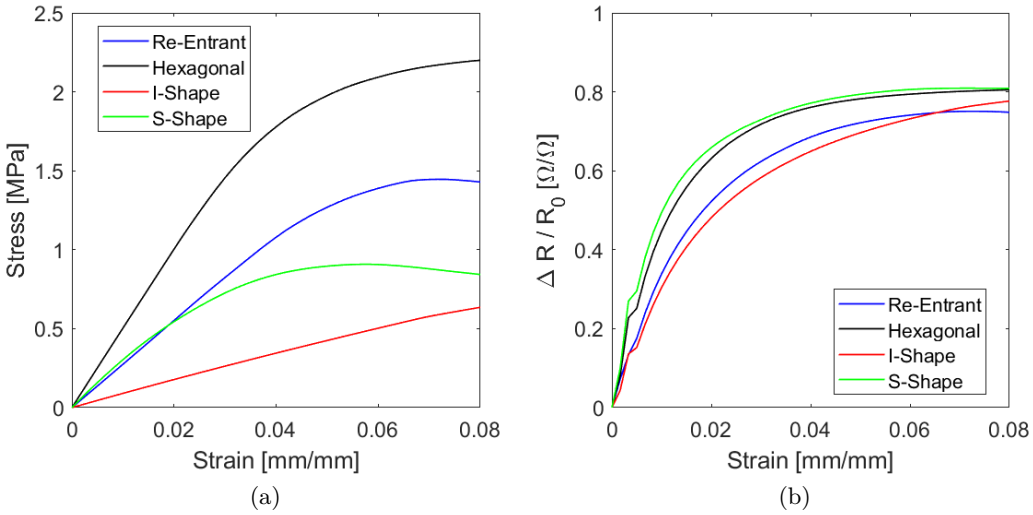

Figure 4.10: Piezoresistive FEA on RVE with PBC results in which solid has got dummy mechanical-thermal properties. (a) Stress-strain response. (b) Resistance variation history.

Figure4.10b shows the electrical resistance runs from the resistance at zero loading to a lower value due to the piezoresistive feature of solid material. It is interesting to denote the correlation between the first linear stages with linear elastic mechanical responses. That means the mechanical response may be associated with an electrical response in order to have a self-sensing structure. To quantify these relationships, the gauge factor needs to be calculated.

Figure4.11a shows the gauge factor histories. The gauge factor trends are not linear because of the complex stress state inside the solid part. The solid part is compressed or stretched in the function of unit-cell topology. The nonlinear trends tend to have a constant value once the structures come into the plastic phase. It is reasonable because the solid part overtakes the yielding point and it keeps compressing at the same stress value. In addition, the gauge factor should be merged at about a unique value for all topologies; if the solid part was completely plasticised the stress value should be the same in all structures, thus also the electrical piezoresistive. The geometrical contribution in terms of gauge factor is extremely lower than the constitutive one, as the results in equation4.36 showed. Therefore, the gauge factors tend to be close to each others confirming the numerical results.

Two punctual situations were evaluated: strain $\varepsilon = 1.5\%$ and strain $\varepsilon = 5\%$. The gauge factors in both stages are depicted by barplot in figure4.11b. The more sensitive to change in electrical resistance was the S-shape getting up to 39.82 and then the hexagonal unit-cell. The differences in gauge factors predict the gauge factors are dependent on the unit-cell shape even if the solid material has the same mechanical-electrical response. In literature, it has not discussed yet how the unit-cell affects the gauge factor, thus in this study a strategy to evaluate that is proposed.

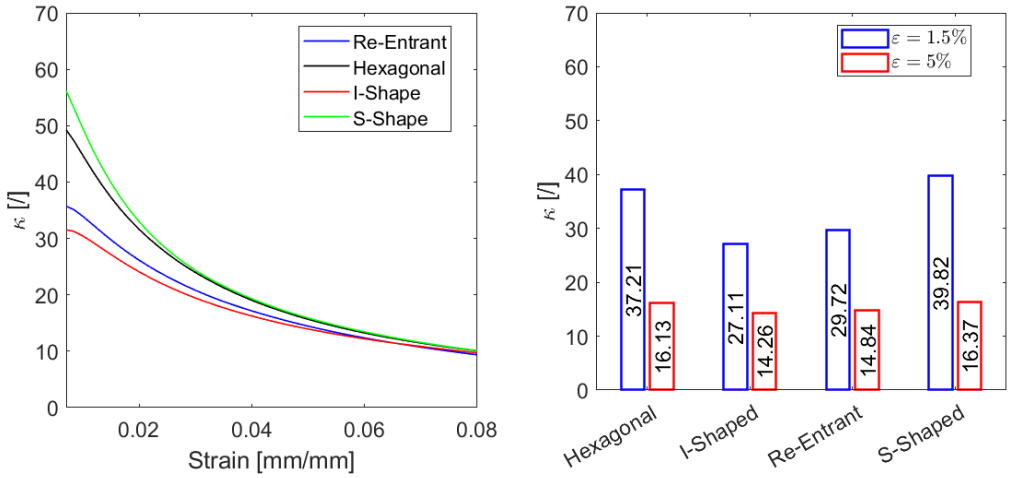

(a) (b)

Figure 4.11: Piezoresistive FEA on RVE with PBC results in which solid has got dummy mechanical-thermal properties. (a) Gauge factors history. (b) Puntual gauge factor values: blue barplot $\varepsilon = 1.5\%$ and red barplot $\varepsilon = 5\%$

Due to the gauge factor being a function of change in resistance and is generated by constitutive piezoresistive behaviour of solid part, stress drives all electrical features. The higher the stress state in a solid and higher is electrical conductivity inside it. Therefore, the higher the solid fraction with high stress at a defined strain stage and higher the change in resistance of the overall unit-cell. In this study, it is proposed a horizontal barplot in which the stress state in a solid at a defined strain stage is evaluated. Figure4.12 shows the stress state in the function of solid volume fraction for each kind of structure at strain stage $\varepsilon = 1.5\%$. The solid fraction can be easily exported from Abaqus from each element as well as the associated stress state.

The bar plots in figure4.12 enable figuring out why the I-shape has got a low gauge factor. In the solid part of the I-shape unit-cell there is a high percentage of solid volume with a low-stress state. That means the electrical resistivity inside it slightly changed from an undeformated state to a deformed and thus the gauge factor is lower than the other structures. In fact, both hexagonal and S-shape reach up to 30 MPa at the same macroscopic strain stage $\varepsilon = 1.5\%$. The change in stress is reflected in a change in the gauge factor. However, from these bar plots, the reason why the highest gauge factor turns belong to S-shape is not explained. The hexagonal structure shows a high percentage of solids with high stress. To explain that it needs to evaluate the electric current flow path or heat flow path in analogy.

Figure4.13 shows the heat flux magnitude and stress state fields in S-shape and Hexagonal unit-cells. The heat flux travels inside the solid part connecting the upper and lower edges along the shortest path. It is clearly visible in the S-shape unit-cell where the heat flux flows only in a vertical direction without travelling along the

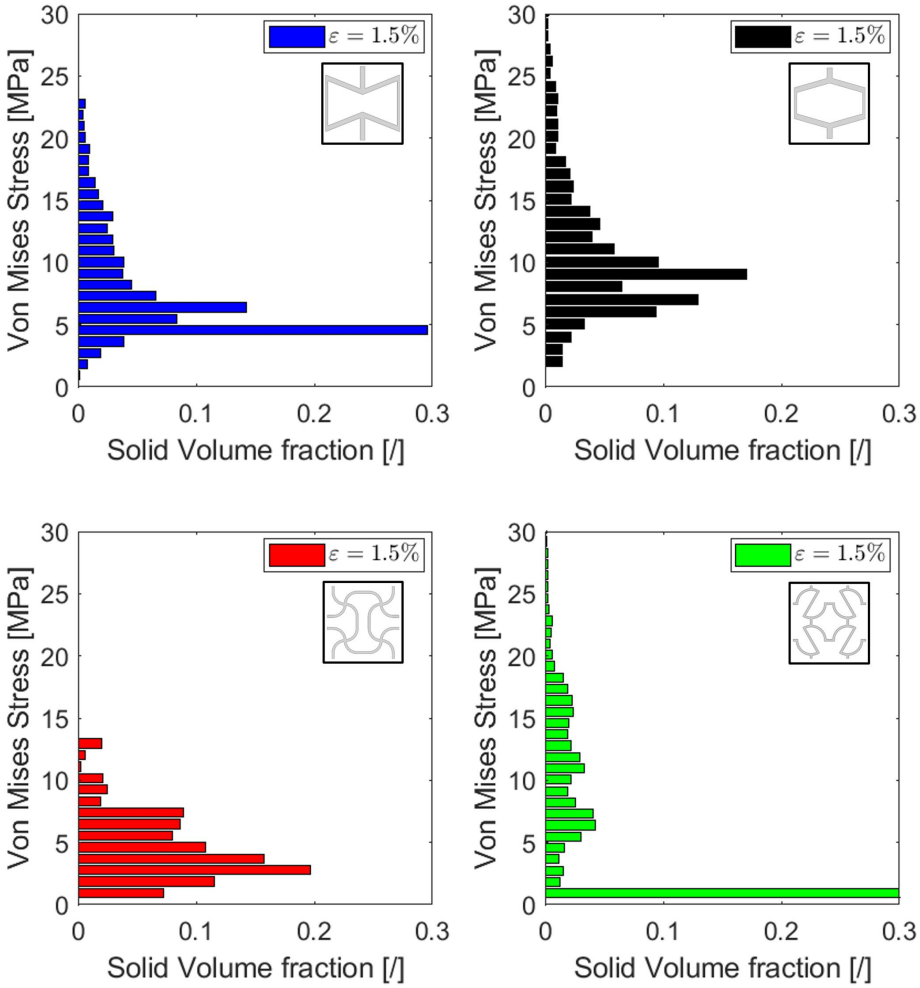

Figure 4.12: Stress state in solid part of unit-cell at macroscopic strain stage $\varepsilon = 1.5\%$.

central zone. In complex unit-cell topology, the shortest is not always associated with high-stressed zones. Thus, a highly stressed zone that exhibits lower electrical resistivity may not be travelled by electric current. Therefore, the perfect scenario is having the electrical current flows agree with the high-stress zone in a solid. A parameter ables to quantify the mutual contribution of stress and current flow is introduced. It is called MC and it is defined as follows

$$MC = \Phi = \sigma q \tag{4.41}$$

The MC value can be visualized as well as the stress field in unit-cell solid region. MC parameter for S-shape and hexagonal unit-cells are depicted in figure4.14. Figure4.14 shows the S-shape unit-cell has a higher solid fraction with high MC values

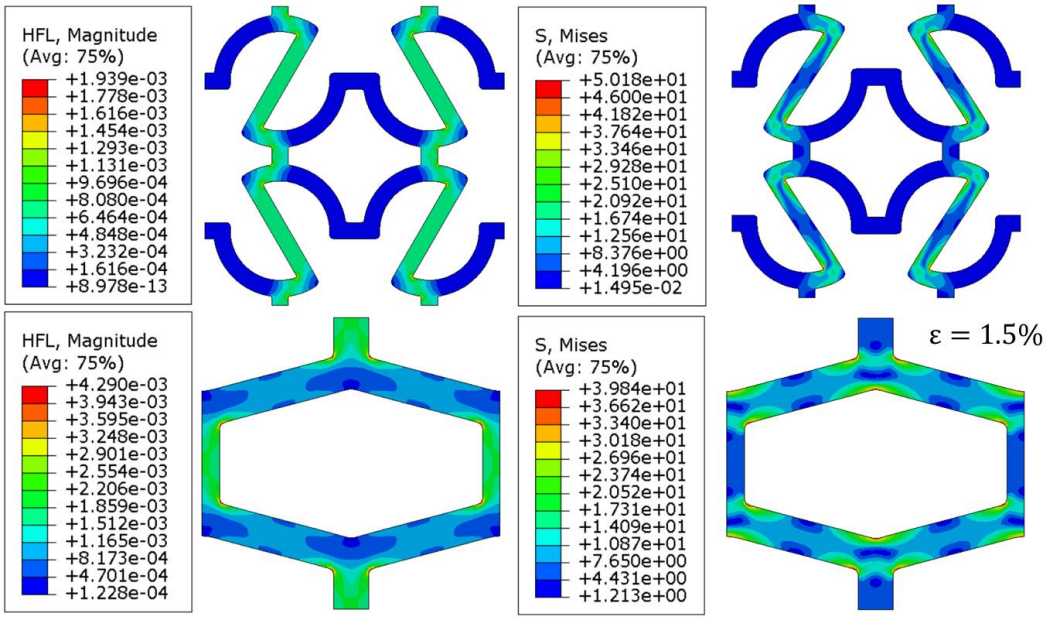

Figure 4.13: Heat flux magnitude and stress state fields in S-shape and Hexagonal unit-cells at macroscopic strain stage $\varepsilon = 1.5\%$.

than the hexagonal unit-cell. Therefore, the higher stressed zones in the S-shape unit-cell are also preferentially travelled by the electric current. The mutual contribution between stress and current path gives to S-shape higher change in electric resistance than hexagonal. Consequently, the gauge factor turns out to be higher in S-shape than in the hexagonal, explaining why the S-shape has got the best piezoresistivity properties.

At strain stage$\varepsilon = 1.5\%$ the solid part in cellular materials are in linear elastic phase whereas at strain stage $\varepsilon = 5\%$ the solid is not longer fully elastic; hence, some plasticized zone appear as figure4.15 shows. I-shape did not reach the plastic zone so the gauge factor should keep changing following the linear relationship. That means, at large strain, I-shape should turn out to be the structure with a higher gauge factor due to the other 2D structures' piezoresistive behaviours that may be limited by the constant stress in plastic zones.

4.3.2 Fully Nonlinear Piezoresitive Numerical Model

The numerical procedure introduced before turns out to be a high potentiality simulation tool of piezoresistive behaviour. However, it has got limits connected to the implicit solver. Implicit solver exhibits difficulties to model boundary nonlinearities, geometric nonlinearities, material nonlinearities, rupture, and dynamics of materials although it is extremely robust with low complexity computational time in linear problems. It was needed to improve the numerical procedure to achieve complex material behaviour like the PEI honeycombs compression response modelled in the previous section.

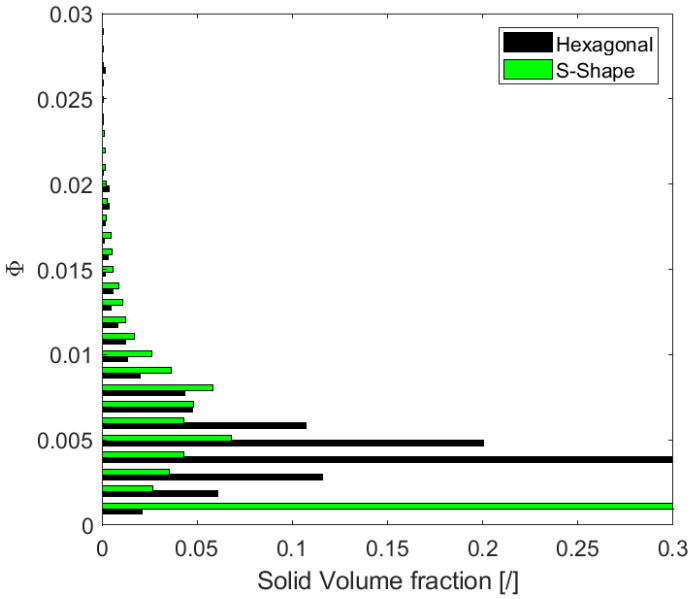

Figure 4.14: Mutual contribution of stress and current flow in S-shape and Hexagonal unit-cells at macroscopic strain stage $\varepsilon = 1.5\%$.

The idea to guarantee steady-state conditions drives the new numerical procedure concept. The proposed numerical procedure decouples the mechanical analysis from the thermal one. In this way, the piezoresistive behaviour can be simulated also in dynamics simulation and more parameters can be evaluated to describe the real piezoresistivity behaviour. The procedure conceptualization is depicted in figure4.16. Once the mechanical analysis is performed on cellular material, the associated deformation shapes are exported step-by-step. Moreover, Abaqus is able to export all kinds of information for each step. In piezoresistivity simulation, the stress field plays a crucial role so it must be exported at each step. In addition, the element status is exported to identify the deleted elements.

The thermal resistance is evaluated by carrying out steady-state thermal simulations for each step, like that introduced before through USDFLD subroutine. The implicit thermal solver enables the model of contacts and interactions between conductive surfaces or elements. The solution to this nonlinear problem is achieved by an implicit solver because the solution is not time-dependent. Therefore, for each mechanical analysis step an associated thermal resistance is guaranteed. Merging the thermal results with the mechanical results and applying the thermo-electric analogy, the piezoresistive behaviour is now modelled. The strong potentiality of this procedure is the coupling freedom of fictitious thermal resistivity. For example, the mechanical analysis can take into account the real temperature developed in compression or tensile test. The temperature can be exported step-by-step and then manipulated to change the fictitious thermal resistivity in the piezoresistive analysis. This procedure is applied to model the fully nonlinear piezoresistive behaviour of

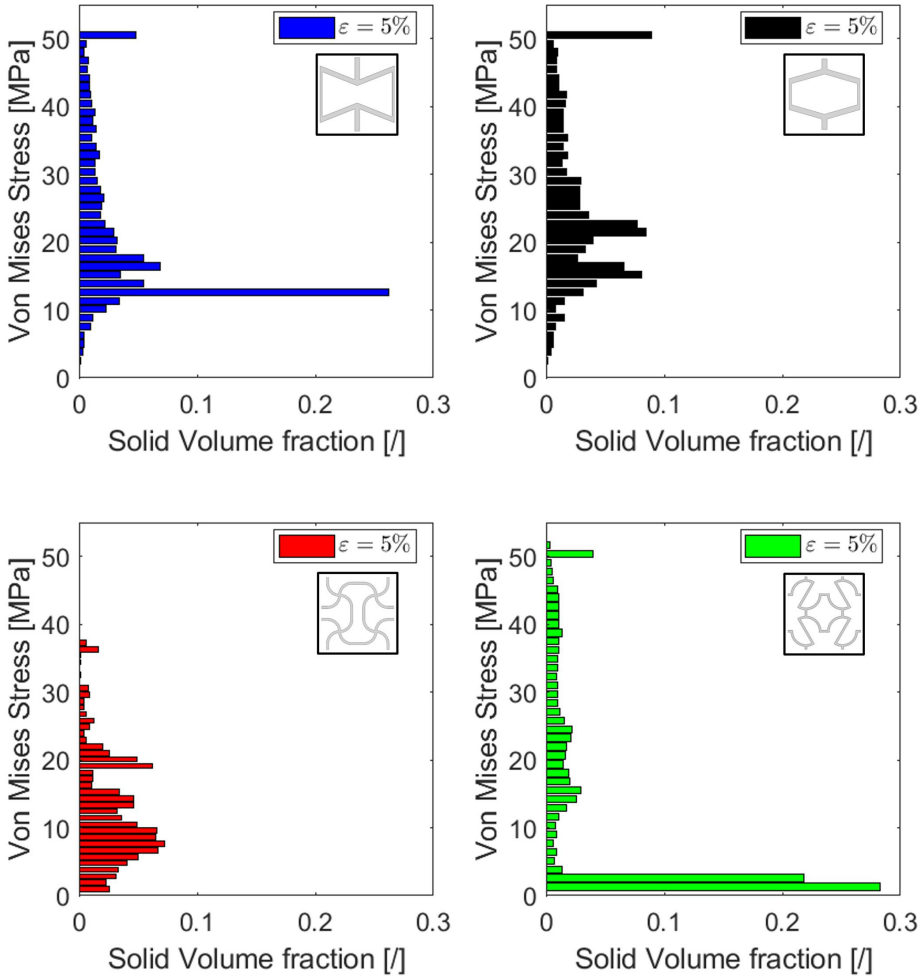

Figure 4.15: Stress state in solid part of unit-cell at macroscopic strain stage $\varepsilon = 5\%$.

the 4 unit-cell introduced in previous sections.

Mechanics of cellular materials describe the stress-strain curve by three stages: linear elastic, plastic or plateau, and densification regime. In order to model the densification phenomena a rigid plate needs to be defined in the mechanical analysis. In piezoresistive analysis, the rigid plate must be also conductive. The conductance at the interfaces must be taken into account to predict a change in resistivity due to compaction or interactions between rigid plates and structure. In this study, a high conductive plate was defined in mechanical analysis as figure4.17 shows. Figure4.17 explains in detail the interaction problems. The conductance at the interface is modelled by a step-wise function; hence, the conductance is extremely high when the gap is zero whereas the conductance is zero when clearances are generated. The figure4.17 shows also the structure interaction by folded cell walls and how Abaqus is able to simulate the interaction. These new paths created during the simulation

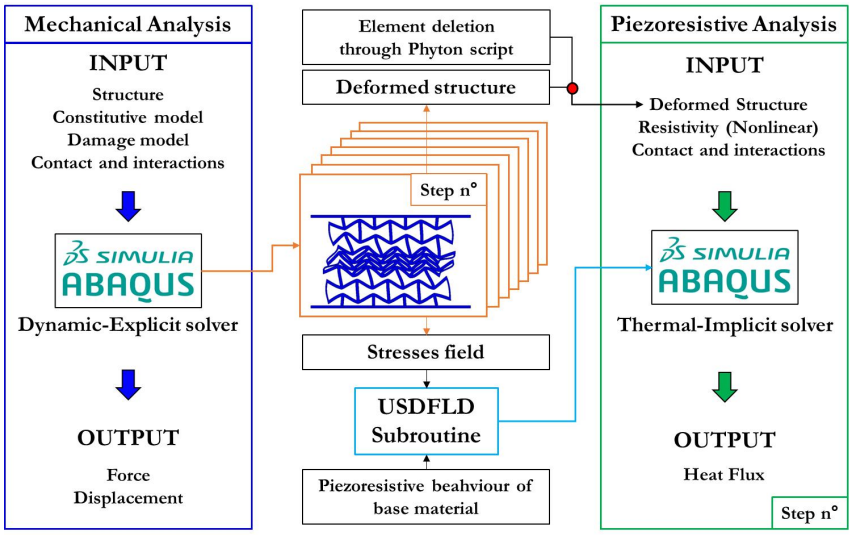

Figure 4.16: Sketch of numerical simulation procedure to predict fully nonlinear piezoresistivity in Abaqus

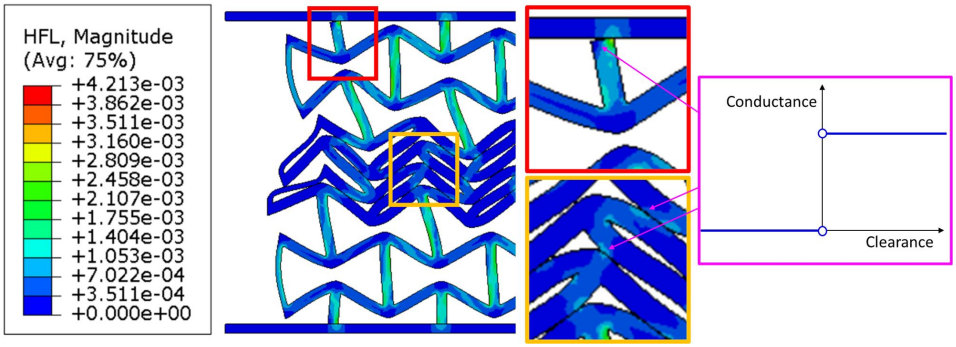

Figure 4.17: Contacts and interactions modelling in piezoresistive analysis.

are crucial to evaluate changes in electric current flow in the cellular material.

Figure4.18 shows the FEA results on honeycombs fashioned by 4x4 unit-cell with relative density $\bar{\rho} = 30\%$, i.e. I-shape, S-shape, re-entrant, and hexagonal unit-cell. The mechanical and thermal properties are the same introduced before, i.e. table4.9. No fails are modelled. Figure4.18a shows a well-known mechanical response of cellular material. Figure4.18b shows the change in resistance during the compression test. The three stages in mechanical responses are visualized also in electric response. In detail, the linear-elastic stage generates a quick rise in a change in resistance. Once the initial collapse stress is reached, the stress-strain curves exhibit the plastic or plateau stage in which the cellular materials is progressively collapsed. The change in electrical resistance also shows a like-plateau stage after the initial collapse stress. The change in resistance shows a hardening behaviour up to the onset of densification occurs. Beyond densification strain, the change in resistance is constant meanwhile the stress suddenly rises. The change in resistance is constant because the material is fully plastic, the stress does not increase and thus

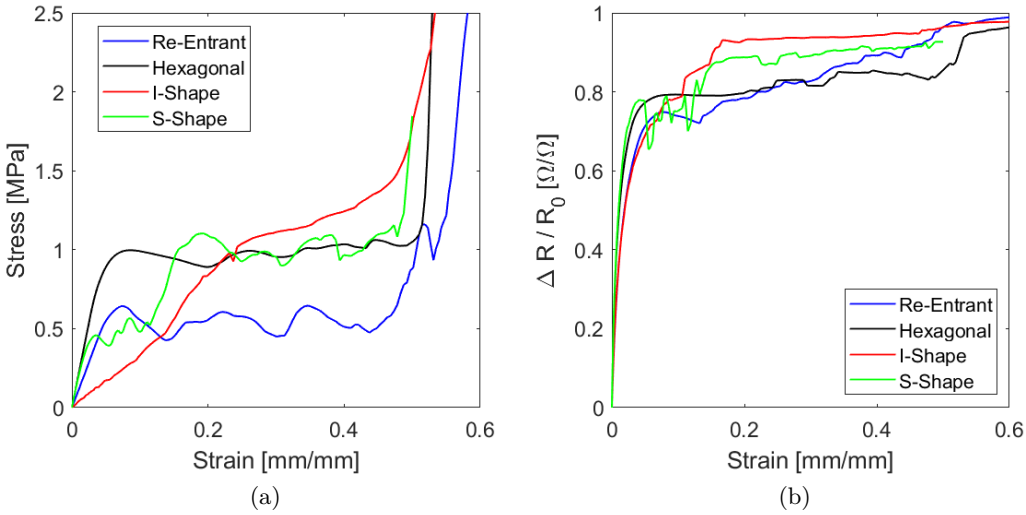

Figure 4.18: Piezoresistive FEA on honeycombs in which solid has got dummy mechanical-thermal properties. (a) Stress-strain response. (b) Resistance variation history.

the resistivity is affected by only geometrical contributions. These contributions are insignificant compared to the constitutive piezoresistive behaviour as demonstrated before.

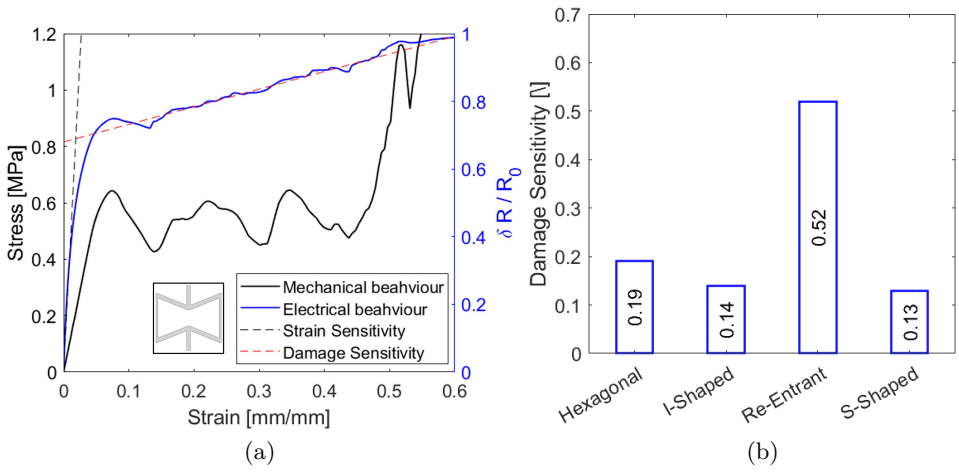

Figure 4.19: Damage sensitivity. (a) Mechanical and electrical response of re-entrant honeycomb. (b) Comparison of unit-cell damage sensitivities.

Consequently, the change in resistance behaviour can be described by the bilinear model as well as the mechanical properties[18]. A strain sensitivity parameter can be introduced; Young's modulus in mechanics can be associated with a strain sensitivity, i.e. the gauge factor GF, whereas the hardening modulus in mechanics can be associated with a damage sensitivity, as described in figure4.19a. The gauge factors

coincide with the linear FEA model on unit-cells and they are already discussed before. The damage sensitivity of each honeycomb is shown in figure4.19b. Re-entrant honeycomb exhibits a higher damage sensitivity. The buckling phenomenon on the collapse mechanism governs the plastic phase. The solid part does not reach yielding stress so the electrical resistivity is able to keep decreasing inside the folded cell walls, exhibiting the "hardening" trend in the plastic phase.

4.4 Electrical properties of PEI composite honeycombs

Polyetherimide (PEI) is a glassy thermoplastic polymer that belongs to the high-performance engineering polymer. It is well-known for its thermal properties and atoxicity. PEI is a dielectric material due to polymers nature. However, its high physics and mechanical performances lead to changes in the PEI dielectric nature in order to allow it to be conductive. Conductive PEI has got a great potentiality in structural applications in which a multi-functional design is needed. Therefore, a conductive PEI could be used as a solid constituent in cellular material. The achievable material properties would be beyond a cellular material made of traditional PEI has got. Therefore, the cellular material in which a solid is conductive PEI can be defined as a metamaterial.

4.4.1 Experimental testing

In this study, the PEI conductivity is allowed by reinforcing Ultem 1000 granules with 3 wt.% of Carbon nanotubes. PEI granules with CNT's are manufactured by professor Cebeci and it is not a commercial PEI composite, all information about the manufacturing process is referred to in the article[23]. The PEI composite is extruded by single-screw extrusion until filament winding. CNTs/PEI Filament is 3D printed by FFF printer Apium. The 3D printing parameters are quite similar to the neat PEI ones illustrated in the second section. 3D printing of CNTs/PEI was extremely challenging because the filament quality is not as good as commercial filament. Moreover, the CNT increases the polymer's thermal conductivity and increases polymer viscosity. Both properties affect the deposition quality; they lead to an increase up to 390°C the nozzle temperature and reduce printing speed.

In this study, honeycombs with relative density $\bar{\rho} = 30\%$ are 3D printed in PEI composite with 4 different unit-cell topologies: S-shape, I-shape, re-entrant, and hexagonal. The honeycombs sizes are 32x32 mm and the width were the half edges sizes, i.e. 16 mm. A fashion of 4x4 unit-cells unsures an acceptalbe corrispondence of overll honeycombs mechanical properties with the predicted on by means of Representative Volume Element theory [64, 49]. The FFF-parts are shown in figure4.20.

PEI composite honeycombs were tested under compression loading. In addition, a characterisation of mechanical and electrical properties was carried out. The bulk material properties were evaluated through tensile tests and compression tests.

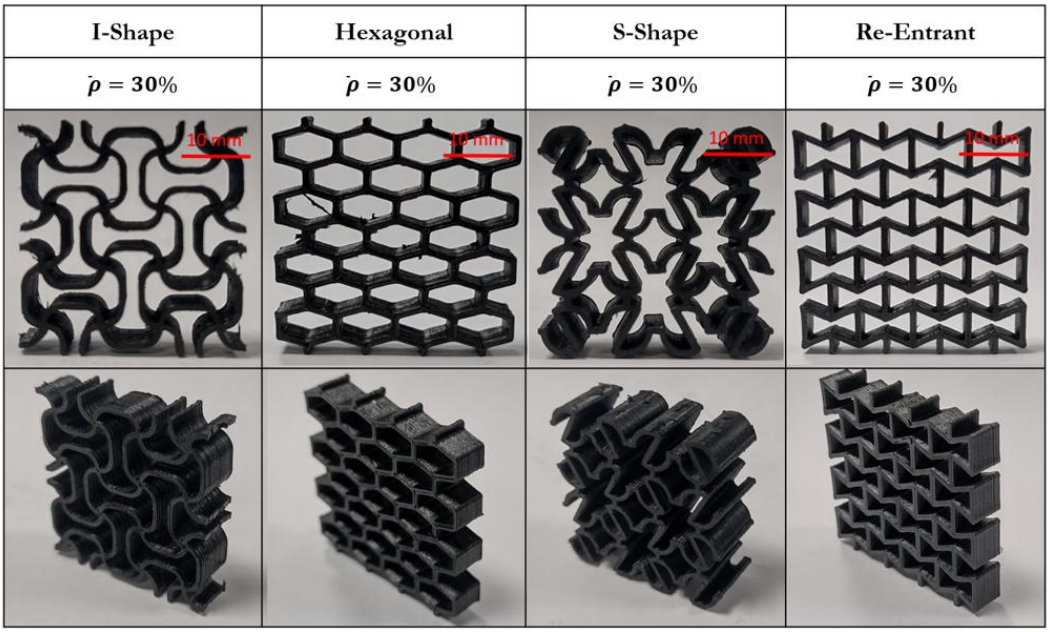

Figure 4.20: Additively manufactured PEI composite honeycombs $\bar{\rho} = 30\%$ with hexagonal, re-entrant, I-shape, and S-shape unit-cell topologies.

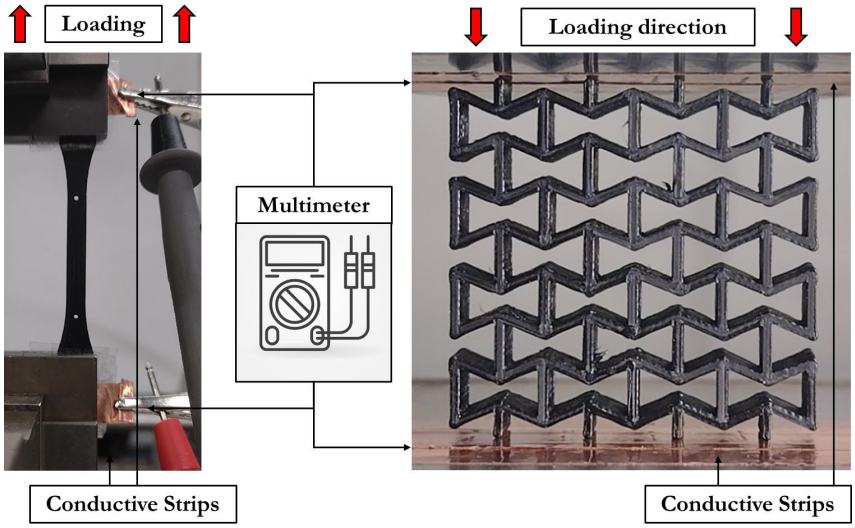

Figure 4.21: Experimental tests set up.

Dogbone specimens ruled by ASTM D638 were printed in which the deposition path is aligned to the loading direction. Only one printing direction was tested for now, in future could be interesting to evaluate the anisotropy behaviour of printed samples. Cylinder specimens with $d/h = 1$ ratio were printed, so the diameter d was equal to the height h. This ratio is well established in compression testing because it allows a uniform stress state also in dynamic conditions without showing buckling phenomena. The printing direction is aligned along the loading direction as well as inside the dogbone specimen.

The experimental set-up testing is quite similar to mechanical properties testing. Both monoaxial tensile and compression tests were performed through Zwick Roel Z050 and they are shown in figure4.21. The electric properties were measured through a digital multimeter that recorded the resistance as the loading was applied. Copper strips were applied on the eternal edges and the multimeter pins were fixed on them, as shown in figure4.21. The grippers or compressive plates were completely insulated in order to ensure the electrical resistance belongs only to the specimen.

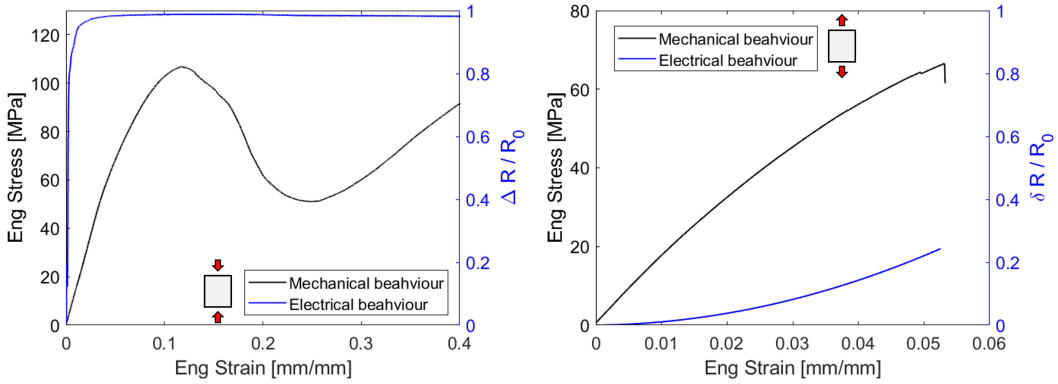

Figure 4.22: Mechanical and electrical properties of 3D printed PEI composite. (a) Compression test results. (b) Tensile test results.

The results of compression and tensile tests are shown in figure4.22. The PEI composite exhibits an extremely brittle behaviour under tensile loading. Otherwise, the compression test turns out the PEI composite is ductile with a strong strain-softening stage. However, the strain-softening stages are not completely due to the constitutive PEI composite properties. The cylinder deposition strategy affects the post-yielding stage; macroscopic fails and delamination appeared. The electrical resistance follows the deformation. In a tensile test, figure4.22b, the electrical resistance increases its value up to 20%. Once the failure occurs, the electrical resistance jumps to an infinitive value. On the contrary, the electrical resistance in the compression test, figure4.22a, shows a rapid arises at the beginning of the test and a quite stable electric resistance signal after the yielding point. The scale does not allow appreciating this because the PEI composite is extremely sensible and the electrical resistance changes quickly.

The PEI composite mechanical and electrical properties are listed in table4.5. PEI composite exhibits higher stiffness compared to the neat PEI printed in the previous sections. The CNTs dispersed inside the PEI increase the mechanical performances also in terms of yielding point reaching up to 112 MPa in compression state. Young's modulus is quite similar in compression and tensile states, so it is assumed to have the same values, i.e. 3368 MPa.

The 3D printed PEI composite electrical resistivity at zero loading is similar in

Table 4.5: Mechanical and electrical properties of 3D printed PEI composite.

E	ν	ρ^0	GF_C	GF_T	$GF_{C-1.5\%}$	$GF_{T-1.5\%}$
$[MPa]$	-	$[\Omega mm]$	-	-	-	-
3368	0.3956	828060	164.52	1.83	63.62	3.05

tensile and compression state. It was measured through the equation4.2 where the l was the pins distances and the A the cross-sectional area of the cylinder and dogbone. The gauge factors turn out to be extremely different in compression and tensile states, as figure4.23 shows. The gauge factor in the tensile state is quite similar to what theory dictates, i.e. $GF = 1 + 2\nu = 1.79$, whereas the gauge factor in the compression state is extremely high. The CNTs provide the PEI composite with a strongly nonlinear piezoresistivity once the compressive loading is applied. Both gauge factors are positive, which means the change in resistance is negative in the compression state and positive in the tensile state. The CNTs provide a linear gauge factor in the stress state and are strongly nonlinear in compression one.

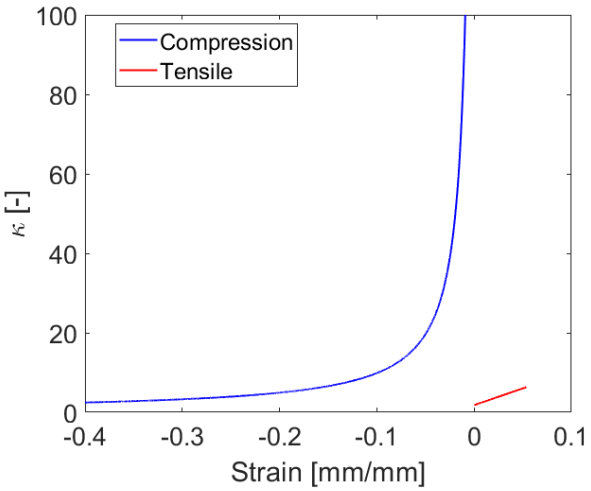

Figure 4.23: PEI composite gauge factors under compression and tensile loadings.

Figure4.24 shows the compression test results on 3D printed PEI composite honeycombs with different unit-cells: re-entrant, S-shape, I-shape, and hexagonal. The experimental results show a brittle behaviour of PEI composite honeycomb. The stress-strain curves do not exhibit a stable plastic phase, the densification regime is not even reached. The honeycombs come out of the compressive plate after some failures occur. The electrical resistance histories show a high piezoresistive behaviour as expected from bulk PEI composite results. The resistance changes instantly once a failure occurs. The electrical resistance jumps to an extremely high value because the honeycombs broke into several pieces. Thus, the honeycombs' contact with conductive strips got loosed. this phenomenon can be explained by the traditional theory of electrical resistance on continuous. If the honeycombs were supposed to

be modelled as electrical resistance fashioned in parallel, the equivalent electrical resistance could be computed as

$$\frac{1}{R_{Eq}} = \sum_i \frac{1}{R_i} \tag{4.42}$$

Once a failure occurs, an electrical resistance that makes up the equivalent electrical resistance system gets loose. Thus, the equivalent resistance should be increased instantly. In compression case, the change in electrical resistance should instantly goes up. $\frac{\Delta R}{R_0}$ is commonly plotted in reverse sign so the jump is commonly visualized in opposite direction.

The piezoresistive results show the PEI composite honeycombs are not suitable to monitor the mechanical collapse beyond the yielding point. The greater brittleness provides a poor self-sensing feature on the plastic phase.

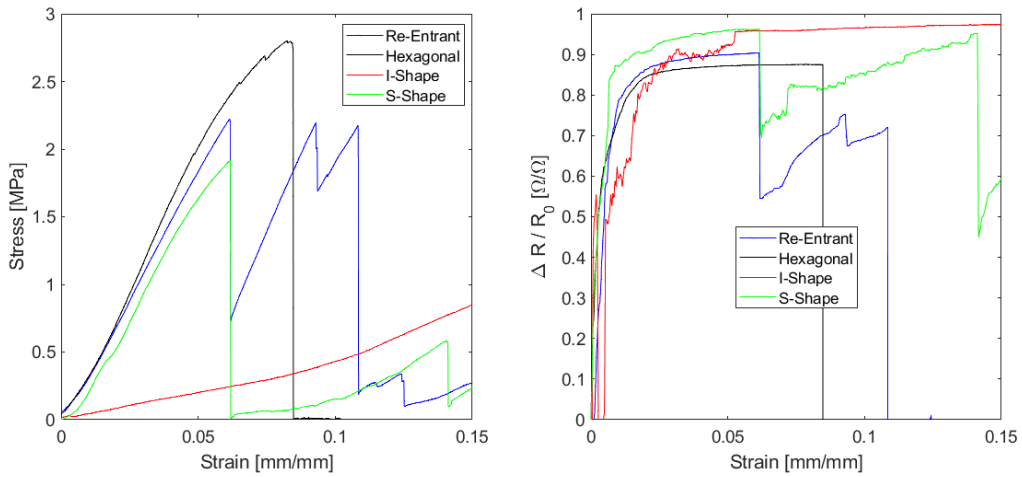

Figure 4.24: In-plane mechanical and electrical performances of PEI composite honeycombs with relative density $\bar{\rho} = 30\%$. (a) Stress-strain response. (b) Resistance variation history.

On the contrary, PEI composite honeycombs turn out to be extremely sensitive to loading changes in the linear elastic stage, as figure4.25 shows. The gauge factors are so higher that could be considered a giant piezoresistive effect. Two punctual situations were evaluated: strain $\varepsilon = 1.5\%$ and strain $\varepsilon = 5\%$. The gauge factors in both stages are depicted by barplot in figure4.25b. The more sensitive to change in electrical resistance was the S-shape getting up to 59.44. The higher piezoresistive behaviour was predicted also by FEA on unit-cell as well as the worst piezoresistive behaviour of I-shape. The results confirm the previous theory on stress state distribution in solid parts. Therefore, the gauge factors obtained show the PEI composite honeycombs are suitable to monitor the mechanical collapse up to the yielding point.

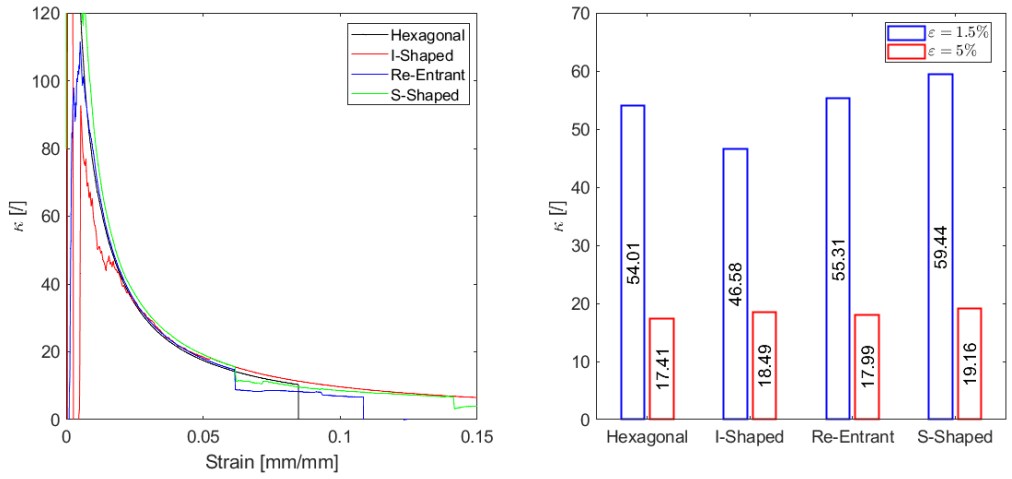

(a) (b)

Figure 4.25: Piezoresistive results of PEI composite honeycombs with relative density $\bar{\rho} = 30\%$. (a) Gauge factors history. (b) Puntual gauge factor values: blue barplot $\varepsilon = 1.5\%$ and red barplot $\varepsilon = 5\%$

The greater piezoresistivity provides a strong self-sensing feature on the linear elastic phase. In addition, the gauge factors measured at strain stage $\varepsilon = 1.5\%$ are slightly lower than bulk PEI composite. That means these self-sensing honeycombs provide the same order piezoresistivity of bulk material with a 70% of weight lower than bulk.

4.4.2 Numerical Analysis

The numerical analysis was only carried out on re-entrant honeycombs because the piezoresistivity study on the other structures is ongoing. The numerical approach has been introduced in the previous section and illustrated in figure4.16. The numerical procedure needs the information on electrical resistivity values of bulk material. Thus, the electrical resistivity was obtained from experimental testing through an analytical approach to constitutive relationships. The electrical resistivity at zero loading was already calculated by the equation4.2. The nonlinear electrical resistivity was a defined function of stress state as figure4.2 shows. The electrical resistance is a function of geometric and constitutive contributions. Thus, the nonlinear constitutive values must be decoupled by the geometric ones. Imposing the monoaxial stress state for isotropic material the electrical resistivity was calculated. It is assumed the loading direction is the 2nd principal direction. Thus, the length l is aligned to the 2nd principal direction and A is the plane normal to the 2nd principal direction. From equation4.2, the electrical resistivity is written as follows

$$\rho(\sigma) = \frac{RA}{l} = R(\sigma)\frac{A_0\left(1 - 2\nu\varepsilon_2 + \nu^2\varepsilon_2^2\right)}{L_0\left(1 + \varepsilon_2\right)} \tag{4.43}$$

The equation4.43, shows how much geometric contribution affects on change in electrical resistivity. The strain or sigma values have to be in agreement with the stress state, e.g. in compression loading, the strain/stress will be negative whereas in tensile loading the strain/stress will positive. The equation4.43 is correct up to the end of the linear elastic regime. Electrical resistivity values beyond yielding points were assumed constant with the same magnitude in yielding point.

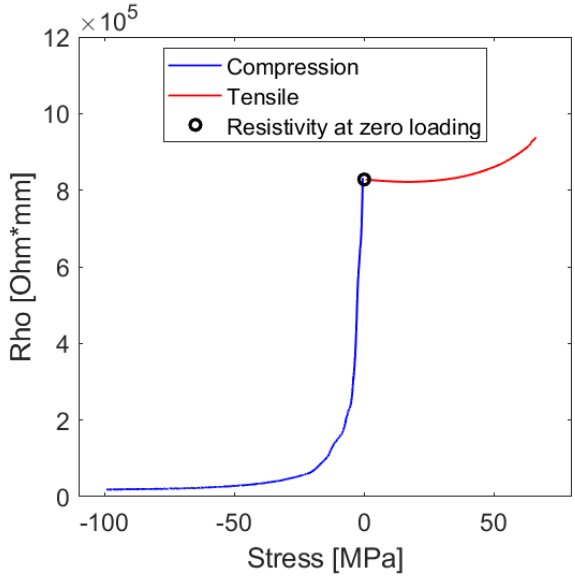

Figure 4.26: Nonlinear electrical resistivity of 3%wt. CNTs/PEI

The nonlinear electrical resistivity is shown in figure4.26. As predicted before, the electrical resistivity is quite constant in the tensile stress state whereas it changes abruptly in the compression state. This asymmetric behaviour will be used to model the piezoresistivity in FEA. The measured electrical resistivity at zero loading is called ρ^0. The $\rho^0 = 828060\,\Omega mm$ measured on bulk PEI composite under tensile and compression state coincides.

Table 4.6: Electrical resistivity comparison between experimental test, numerical prediction and numerical prediction of RVE.

ρ^0_M $[\Omega mm]$	ρ^0_{FEA} $[\Omega mm]$	ρ^0_{RVE} $[\Omega mm]$
14336156	15025523	14903586

It computed the re-entrant honeycomb electrical resistivity imposes the ρ^0 as base material thermal conductivity in the Abaqus model. The numerical prediction was articulated in two ways: the ρ^0_{RVE} is predicted by FEA on RVE and ρ^0_{FEA} is predicted by FEA on the macroscopic structure. The numerical analysis results are shown in figure4.6. The results are consistent. The re-entrant electrical resistivity is about 18 times higher than bulk material and it confirms the resistivity anisotropy

computed on RVE, as shown in figure4.7. These results uphold the introduced piezoresistive procedure based on FEA.

The mechanical response of bulk PEI composite is modelled through Concrete Damage Plasticity (CDP) model. CDP is well-established as a damaged plasticity model for concrete in which brittle failure under tensile test is common as well as an extended strain softening regime after the yielding point. The model in Abaqus is sketched through figure4.27. However, CDP provides a general capability for modelling concrete and other quasi-brittle materials in all types of structures. In literature, CDP is getting to be also used for modelling the mechanical properties of composite materials such as short fibre reinforced polymers or cementitious materials[158, 159, 160, 161].

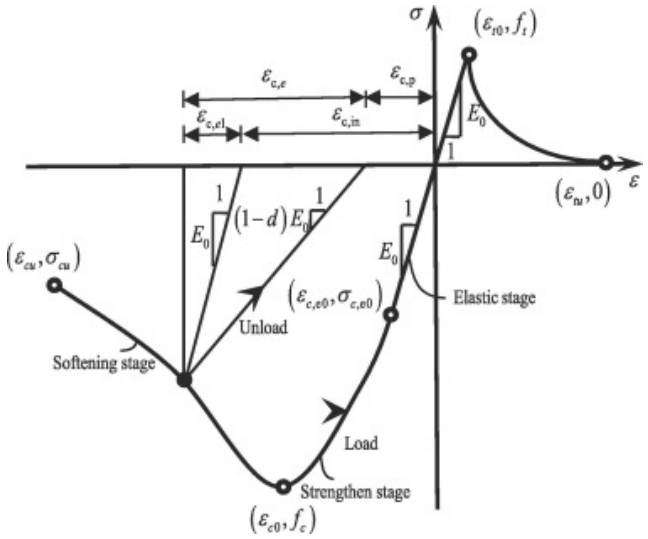

Figure 4.27: Concrete Damage Plasticity model

As the figure4.27 shows, the numerical model is qualitatively similar to PEI composite mechanical properties. However, CDP does not change the nature of polymer physics because the yielding surface is dependent on the hydrostatic pressure. CDP is considered a combination of Drucker–Prager plasticity with isotropic damage using a Rankine-type loading function [162]. In fact, the CDP damage properties suit considerably the brittle failure of composite materials. The damage mechanics change from polymer and composite materials. In composite materials, the specification of post-failure behaviour generally means giving the post-failure stress as a function of cracking strain [162]. The post-failure behaviour for direct straining is modelled with tension stiffening, which allows you to define the strain-softening behaviour for cracked materials. On the contrary, ductile damage models are based on plastic strain and they are well-established for ductile materials such as metals or polymers.

The numerical procedure to simulate the piezoresistivity decouples the mechanical to piezoresistive analysis as figure4.16 shows. First of all the mechanical analysis was

carried out. The re-entrant honeycomb is sandwiched between two conductive plates to take into account conducive interactions at the interfaces. The CDP model was calibrated with the experimental stress-strain curves and the model was assigned to the re-entrant honeycomb. 4-node elements with plain strain formulation were used with the smallest mesh size of about 0.1 mm in order to have a stable time increment of 10^{-7}. Loading conditions were applied in 30 s to avoid dynamics phenomena during the compression. Mechanical contacts are modelled along the tangential and normal direction through penalty parameters, 0.1 for tangential slipping and 1 for normal stiffness.

Once the mechanical analysis was complete, the Von Mises stresses, triaxiality, deformed shape and element status were exported step-by-step from Abaqus. It is supposed the electrical resistivity was a function of Von Mises stress instead of stress along the principal direction. The compressive or stretched zone is defined through the triaxiality parameter. I.e. the compressed zone has got a triaxiality lower than zero and the associated stresses are Von Mises stress. From the triaxiality and Von Mises's stress information, it was generated the field variable inside the USDFLD subroutine with which Abaqus associates the thermal resistivity in piezoresistive analysis. Consequently, the exported deformed shape was imported in Abaqus for piezoresistive analysis. Through Phyton scripting, the elements were deleted according to the element status file exported before. In piezoresistive analysis, the interactions between surfaces were modelled through thermal contact in which the conductance is a function of clearance. The piezoresistive analysis was finally carried out. Figure4.28 allows figuring out better how the nonlinear electrical resistivity is implemented. This procedure is done for each step. At the end of each step, the heat flux is exported and resistance is calculated. The thermal-electrical analogy is finally applied.

Figure4.28 shows the strain stage A pointed out in figure4.29. Figure4.28 shows clearly how the high conductive zones are associated with compressed zone based on negative triaxiality assumption. The asymmetric resistivity affects the heat flux. In these zones, the heat flux travels preferentially as the heat flux magnitude field demonstrates.

The predicted piezoresistive response of PEI composite re-entrant honeycomb with relative density $\bar{\rho} = 30\%$ through FEA is shown in figure4.29. The FEA results predict a first linear elastic stage with a brittle failure as well as the experimental test results. Stage A in figure4.29 depicts the onset of failure. The re-entrant structure is compressed without showing instabilities or plasticized zones. The piezoresistive properties associated with stage A are shown in figure4.29b. FE piezoresistive model shows a temperature linear field in which the temperature goes from 0 (reference) to $1°C$. The associated heat flux at the A stage flows through the 4 ligaments in contact with the conductive plates. FEA predict an inhomogeneous heat flux inside the 4 ligaments. The discontinuity is due to the clearance between the structure pins and conductive plates. Once the re-entrant structure gets to be compressed, the 4 pins

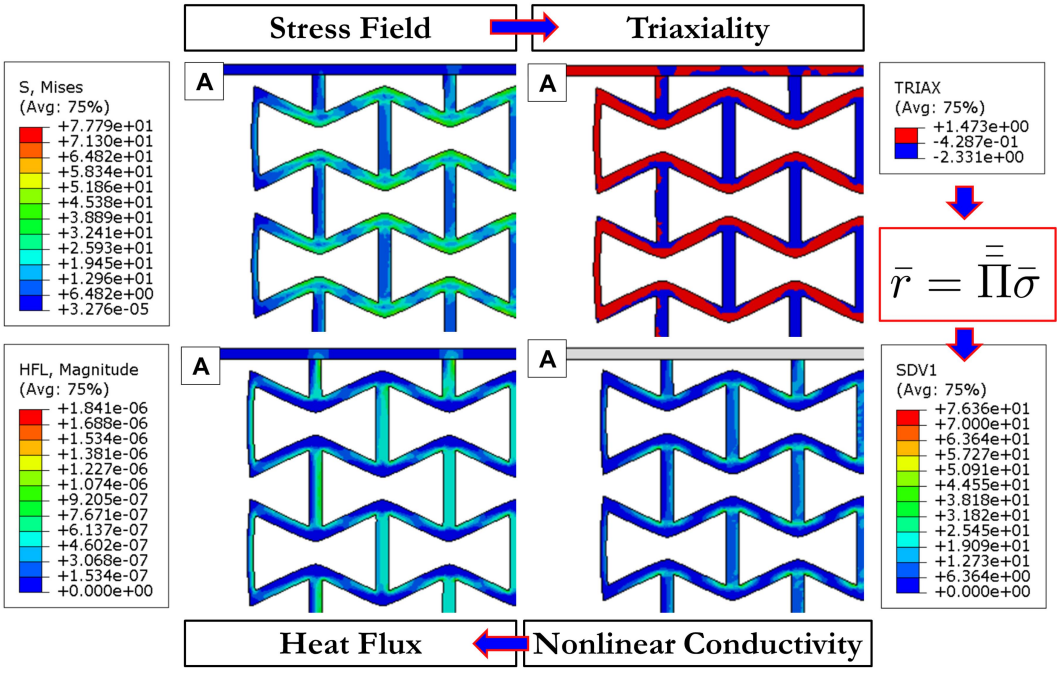

Figure 4.28: Implementing the nonlinear electrical resistivity in Abaqus. Firstly the Von Mises's stress is exported. Secondly, the triaxiality is calculated. Thirdly, the nonlinear conductivity is defined as field variable through piezoresistive stress matrix. At the end, the piezoresistive FEA is carried out

tend to slip due to the structure auxeticity behaviour. The friction counteracts the slipping at the interfaces so that the pins get to fold generating clearance between the conductive plates. As discussed before, the heat flux travels preferentially in the compressed zone so that the heat flux magnitude is higher along the vertical cell walls (pure compression stress state) and on the edges (compression due to bending).

The heat flux field is symmetric anyway with respect to the x-axis and y-axis, which means the heat flux flows in steady-state conditions. In fact, the heat flux can be measured at the structure's top or bottom but the overall value does not change.

After the first failure, the stress drops off and the resistance goes up showing coherent results with experimental ones. Stage B in figure4.29 depicts the failure phenomena. A brittle breaking occurs on the upper side of the structure as well as the FEA predicts. The piezoresistive properties associated with stage B are shown in figure4.29b. In this case, the field temperature is not linear because of ligaments breaking. The broken ligaments are disconnected from the structure thus the temperature can not increase inside them. The instant resistance increases can be also visualized in terms of the heat flux field in figure4.29b. The heat flux magnitude decreases after the failure because the 4 pins are no longer able to transfer heat to the upper conductive plate. Although the broken ligaments interact so that

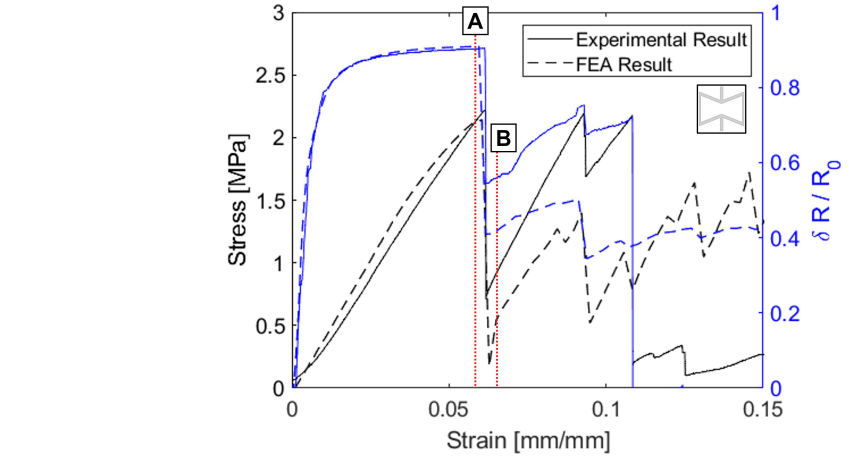

(a)

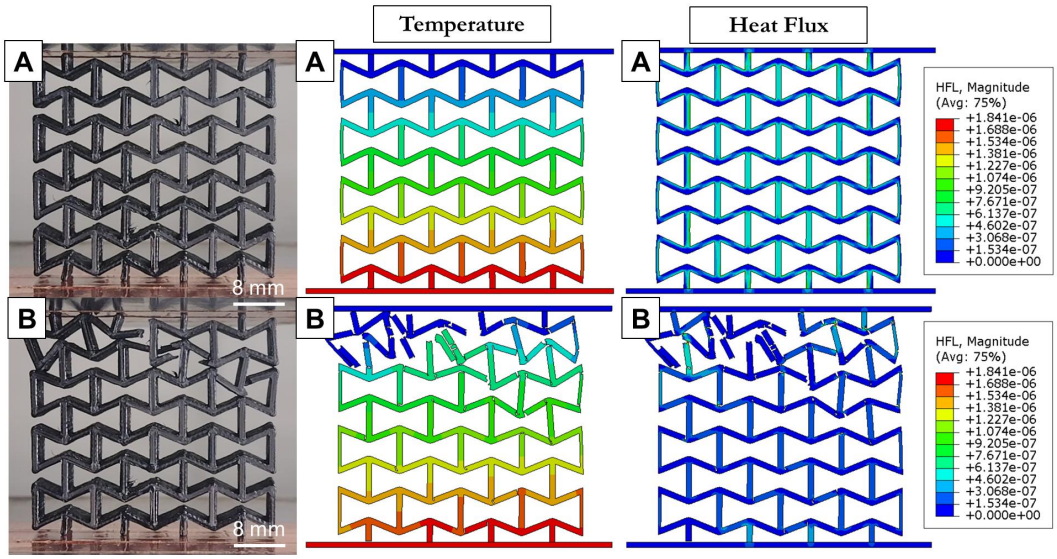

(b)

Figure 4.29: Numerical and experimental piezoresistivity behaviour of PEI composite re-entrant honeycomb with relative density $\bar{\rho} = 30\%$. (a) FEA predictings and experimental piezoresistive responses. (b) Deformed shape at stages A and B. Associated temperature and heat flux filed in FE piezoresistive analysis.

new paths are born, the heat transfer can locally increase, but the overall structure resistance follows the equation4.42. The FEA results diverge from the experimental after the first failure. The mechanical collapse mechanism is quite dependent on the progressive brittle failure of unit-cells, local material properties, and additive manufacturing process. It is quite challenging to describe perfectly the post-failure behaviour but the overall mechanical/electrical behaviour is acceptable.

The numerical results are also compared in terms of gauge factors. The gauge factors predicted by FEA and obtained through the experimental test of PEI com-

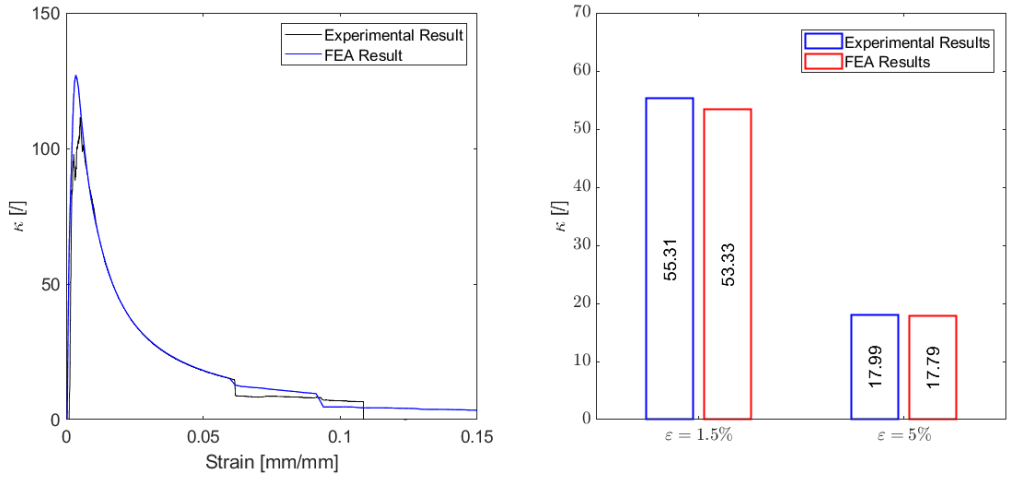

Figure 4.30: Comparison between FEA predicted and experimental gauge factors of PEI composite re-entrant honeycomb with relative density $\bar{\rho} = 30\%$. (a) Gauge factors history. (b) Puntual gauge factor values: blue barplot $\varepsilon = 1.5\%$ and red barplot $\varepsilon = 5\%$.

posite re-entrant honeycomb with relative density $\bar{\rho} = 30\%$ are shown in figure4.30. The gauge factors trend is consistent after some initial differences. The experimental results are affected by compressive adjustments at the interfaces that FEA is not able to predict. However, in the linear elastic phase, the results are superposed. It evaluated two punctual situations: strain $\varepsilon = 1.5\%$ and strain $\varepsilon = 5\%$. The gauge factors in both stages are depicted by barplot in figure4.30b. Both punctual values correspondence confirm the high numerical model accuracy.

The measured guage factors of FFF-printed 3% wt. PEI/CNT cellular composites are compared with those of extant piezoresistive materials, in figure4.31. The punctual gauge factor values are black at $\varepsilon = 1.5\%$ and blue at $\varepsilon = 5\%$. Both values are higher than all other FFF-printed cellular materials. Therefore, PEI/CNT results high value conductive solid material to create self-sensing metamaterials.

4.5 Concluding Remarks

The piezoresistivity of cellular materials was discussed through analytical, numerical and experimental observations. First of all, the piezoresistivity concept was analyzed from linear to nonlinear behaviour introducing the piezoresistive stress and strain matrixes. The analytical theory behind the gauge factor is also explained.

Subsequently, a numerical simulation strategy based on finite element method was introduced. The thermal-electrical analogy was used to simulate the piezoresistive behaviour in the Abaqus environment. The linear piezoresistive behaviour was first analyzed on bulk material in order to confirm the consistency between numerical

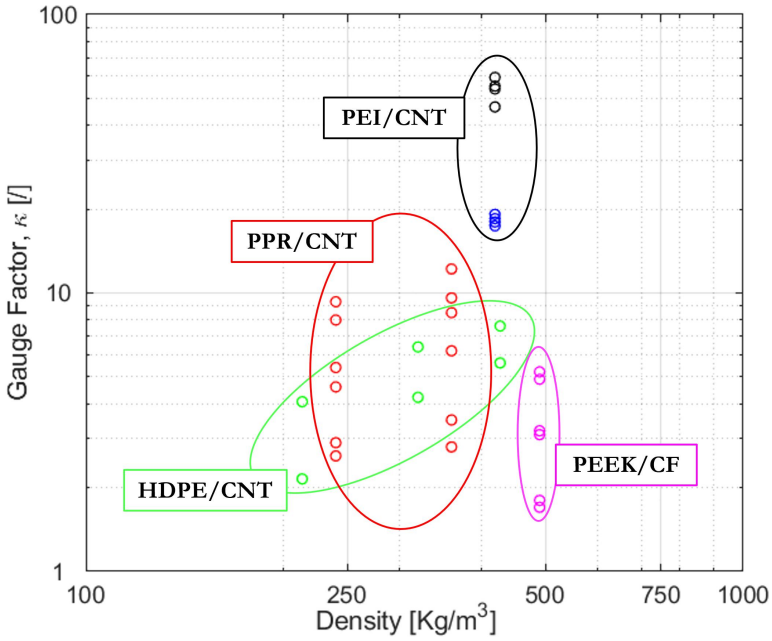

Figure 4.31: Comparison of gauge factors of FFF-printed 3% wt. PEI/CNT cellular composites with those of extant piezoresistive materials: PEEK/CNT [17]. PPR/CNT [18]. HDPE/CNT [19]. The punctual gauge factor values are black at $\varepsilon = 1.5\%$ and blue at $\varepsilon = 5\%$

and analytical results.

The piezoresistive response of four different unit-cell with relative density $\bar{\rho} = 30\%$ were investigated: I-shape, S-shape, re-entrant, and hexagonal unit-cell topologies. The unit-cells electrical resistivity was evaluated through FEA before applying to load. The numerical results predicted an anisotropy resistivity distribution for each unit-cell except for I-shape.

Afterwards, the electrical resistivities were investigated once the structures were deformed. The numerical simulation revealed a limit in the resistivity theory because of the inhomogeneous solid distribution inside the conductor. The homogeneous conductor hypothesis fails, thus the homogenized electrical properties were defined introducing geometrical nonlinearities in the electrical resistivity matrix. It was necessary to calculate the unit-cells elastic anisotropic properties. The in-plane Young's modulus and Poisson's ratio were obtained through a spherical visualization of the homogenised stiffness matrix for each unit-cells. The nonlinear electrical resistivity was finally written in terms of unit-cell Poisson's ratio and Young's modulus.

Subsequently, stress-dependent electrical resistivity was introduced in Abaqus to simulate the general behaviour of piezoresistive materials. Introducing dummy mechanical-electrical properties, the nonlinear piezoresistive response of each unit-cell under compression was simulated. The self-sensing properties of each unit-cell were discussed through bar plots that correlate the stress distribution to the cellular

material volume fraction. S-shape and hexagonal shape showed the highest gauge factors. Introducing the MC parameter, it was explained why the gauge factor of the S-shape was slightly higher than the hexagonal unit-cell.

A fully nonlinear piezoresistive model was defined. The mechanical analysis was decoupled from the thermal one. The new procedure was able to model contacts, interactions, and element deletion. Thus, it was possible to simulate the entire mechanical response of cellular materials under compressive loading up to the densification.

Self-sensing CNT/PEI honeycombs with four different unit-cell were printed through fused filament fabrication technology. The cellular materials were tested under compression loading to investigate their mechanical performances and self-sensing properties. The CNT/PEI honeycombs have a high nonlinear piezoresistive response. The S-shape turns out to have the highest gauge factor because the higher stressed zones in the S-shape unit-cell are also preferentially travelled by the electric current. The mutual contribution between stress and current path gives to S-shape higher change in electric resistance. The CNT/PEI honeycombs gauge factors are higher than other composite FFF-printed structures, as figure4.31 shows. It confirms the strong potential of CNT/PEI cellular materials as self-sensing metamaterials.

The fully nonlinear piezoresistive model was used to simulate the mechanical response of 3D-printed 3% wt. CNTs/PEI. The electrical resistivity of bulk CNT/PEI was obtained by carrying out compressive and tensile tests in which the electrical resistance was together measured. The CNT/PEI electrical resistivity resulted in extremely sensible to compressive stress and quite insensible to tensile stress.

The mechanical properties of CNT/PEI were defined inside the Abaqus through the concrete damage plasticity model. The piezoresistivity simulation was carried out step-by-step in each mechanical analysis step. The nonlinear resistivity was assumed to be a function of Von Mises stress. Thus, the nonlinear resistivity was assigned to each element through the USDFLD subroutine in the function of the Von Mises stress and the triaxiality field exported for each step. Coupling the electrical and mechanical results step-by-step, the piezoresistive response of the re-entrant honeycomb was obtained.

In the end, the piezoresistive behaviour of re-entrat honeycomb was simulated. The numerical model predicted the piezoresistive response up to the first failure. The mechanical response was dependent on the progressive brittle failure of unit-cells, local material properties, and additive manufacturing process. It is quite challenging to describe perfectly the post-failure behaviour but the overall mechanical/electrical behaviour could be considered acceptable.

Chapter 5

Conclusion

The research activity evaluated, simulated, and predicted the mechanical and multiphysics properties of honeycombs made of polyetherimide enabled via additive manufacturing.

Honeycombs made of polyetherimide show great potential in industrial applications in which high mechanical performances and absorption properties are needed. Therefore, coupling the excellent physics PEI properties, i.e. structural, thermal, chemical, and toxicity, with additive manufacturing is possible to realize high performance cellular materials. Unluckily the fused filament fabrication process causes premature interlayer delaminations in honeycomb cell-walls which limits the overall mechanical performances.

According to glassy thermoplastic polymer physics, 3D-printed PEI constitutive model was defined in Abaqus. It was assumed the polymer mechanics can be described through competitions of crazing (brittle failure) and shear yielding (extended ductility). Firstly, the mechanical characterization was carried out following traditional techniques. The extreme PEI brittleness revealed inconsistency between numerical and experimental results. Consequently, from physics and mechanics observations, it was supposed the printed polyetherimide might have higher crazing sensitivity due to the additive manufacturing process. A numerical optimization procedure defined a new failure strain involving an increase in PEI ductility.

The numerical results predicted the mechanical response of honeycombs with low relative density but, by increasing it, the results diverged from experimental ones. Interlayer delamination failures along the extruded filament interfaces dominated the damage mechanism. Therefore, the numerical model evolved again introducing a failure criterion based on shear-normal stress relation along the deposited filament interfaces. The FEA with interlayer failure were able to predict the compressive response of 3D-printed PEI honeycombs. Furthermore, the FEA results were also discussed to quantify the negative effects due to the additive manufacturing process and the honeycombs' achievable properties.

The piezoresistivity of cellular materials was discussed through analytical, numerical and experimental observations. The piezoresistive response of four different unit-cell with relative density $\bar{\rho} = 30\%$ were investigated: I-shape, S-shape, re-entrant, and hexagonal unit-cell topologies. The planar structures exhibit anisotropic electri-

cal properties and nonlinear piezoresistivity. The numerical results revealed a limit in the electrical resistivity theory because of the inhomogeneous solid distribution inside the theoretical conductor. The homogeneous conductor hypothesis fails, thus the homogenized electrical properties were defined introducing geometrical nonlinearities in the electrical resistivity matrix. The nonlinear electrical resistivity was finally written in terms of unit-cell Poisson's ratio and Young's modulus.

The self-sensing properties of each unit-cell were explained through bar plots that correlate the stress distribution to volume fraction. The S-shape turns out to have the highest gauge factor because the higher stressed zones in the S-shape unit-cell are also preferentially travelled by the electric current. The mutual contribution between stress and the current path gives to S-shape higher change in electric resistance. Consequently, the MC parameter explained why the S-shape has got the best self-sensing properties.

Self-sensing CNT/PEI honeycombs with four different unit-cell were printed through fused filament fabrication technology. The cellular materials were tested under compression loading to investigate their mechanical performances and self-sensing properties. The CNT/PEI electrical resistivity resulted in extremely sensible to compressive stress and quite insensible to tensile stress. This CNT/PEI high sensibility gives 3D-printed honeycomb gauge factors higher than all other FFF-printed cellular materials. The S-shape was confirmed as the best unit-cell topology. Therefore, PEI/CNT results in high-value conductive solid material to shape self-sensing metamaterials.

Afterwards, the piezoresistive behaviour of the re-entrant honeycomb was simulated. The nonlinear electrical resistivity of bulk CNT/PEI was implemented into Abaqus constitutive model. The mechanical response along with the piezoresistive behaviour of CNT/PEI honeycombs under compression was simulated. The numerical model predicted consistently the piezoresistive response up to the first failure.

The research on self-sensing CNT/PEI honeycombs is ongoing. The piezoresistive response of the other honeycombs will be simulated in the near future.

Bibliography

[1] N. A. Fleck, V. S. Deshpande, M. F. Ashby, Micro-architectured materials: past, present and future, Proceedings of the Royal Society A: Mathematical, Physical and Engineering Sciences 466 (2121) (2010) 2495–2516. doi:10.1098/rspa.2010.0215.
URL https://doi.org/10.1098/rspa.2010.0215

[2] S. J. Yeo, M. J. Oh, P. J. Yoo, Structurally controlled cellular architectures for high-performance ultra-lightweight materials, Advanced Materials 31 (34) (2018) 1803670. doi:10.1002/adma.201803670.
URL https://doi.org/10.1002/adma.201803670

[3] O. Al-Ketan, R. Rowshan, A. H. Alami, Biomimetic materials for engineering applications, in: Encyclopedia of Smart Materials, Elsevier, 2022, pp. 25–34. doi:10.1016/b978-0-12-815732-9.00019-x.
URL https://doi.org/10.1016/b978-0-12-815732-9.00019-x

[4] L. J. Gibson, M. F. Ashby, Cellular Solids, Cambridge University Press, 1997. doi:10.1017/cbo9781139878326.
URL https://doi.org/10.1017/cbo9781139878326

[5] S. Yuan, C. K. Chua, K. Zhou, 3d-printed mechanical metamaterials with high energy absorption, Advanced Materials Technologies 4 (3) (2018) 1800419. doi:10.1002/admt.201800419.
URL https://doi.org/10.1002/admt.201800419

[6] J. L. Bouvard, D. K. Ward, D. Hossain, E. B. Marin, D. J. Bammann, M. F. Horstemeyer, A general inelastic internal state variable model for amorphous glassy polymers, Acta Mechanica 213 (1-2) (2010) 71–96. doi:10.1007/s00707-010-0349-y.
URL https://doi.org/10.1007%2Fs00707-010-0349-y

[7] C. C. Chau, J. C. M. Li, Fracture of shear bands in atactic polystyrene, Journal of Materials Science 16 (7) (1981) 1858–1873. doi:10.1007/bf00540634.
URL https://doi.org/10.1007%2Fbf00540634

[8] A. J. Kinloch, R. J. Young, Fracture Behaviour of Polymers, Springer Netherlands, 1995. doi:10.1007/978-94-017-1594-2.
URL https://doi.org/10.1007%2F978-94-017-1594-2

[9] G. Jacoby, C. Cramer, Vorgänge vor und bis zum bruch bei statischer und dynamischer beanspruchung von polykarbonat, Rheologica Acta 7 (1) (1968) 23–51. doi:10.1007/bf01970313.
URL https://doi.org/10.1007%2Fbf01970313

[10] S. STERNSTEIN, Mechanical properties of glassy polymers, in: Properties of Solid Polymeric Materials, Part B - Treatise on Materials Science and Technology, Elsevier, 1977, pp. 541–598. doi:10.1016/s0161-9160(13)70095-4.
URL https://doi.org/10.1016%2Fs0161-9160%2813%2970095-4

[11] C. G'sell, N. A. Aly-Helal, J. J. Jonas, Effect of stress triaxiality on neck propagation during the tensile stretching of solid polymers, Journal of Materials Science 18 (6) (1983) 1731–1742. doi:10.1007/bf00542069.
URL https://doi.org/10.1007/bf00542069

[12] V. Novikov, E. Rössler, Correlation between glass transition temperature and molecular mass in non-polymeric and polymer glass formers, Polymer 54 (26) (2013) 6987–6991. doi:10.1016/j.polymer.2013.11.002.
URL https://doi.org/10.1016%2Fj.polymer.2013.11.002

[13] C. G. Sell, N. A. Aly-Helal, J. J. Jonas, Effect of stress triaxiality on neck propagation during the tensile stretching of solid polymers, Journal of Materials Science 18 (6) (1983) 1731–1742. doi:10.1007/bf00542069.
URL https://doi.org/10.1007%2Fbf00542069

[14] L. Mizzi, D. Attard, R. Gatt, K. K. Dudek, B. Ellul, J. N. Grima, Implementation of periodic boundary conditions for loading of mechanical metamaterials and other complex geometric microstructures using finite element analysis, Engineering with Computers (Jan. 2020). doi:10.1007/s00366-019-00910-1.
URL https://doi.org/10.1007/s00366-019-00910-1

[15] J. Yin, C. Lu, J. Fu, Y. Huang, Y. Zheng, Interfacial bonding during multi-material fused deposition modeling (FDM) process due to inter-molecular diffusion, Materials & Design 150 (2018) 104–112. doi:10.1016/j.matdes.2018.04.029.
URL https://doi.org/10.1016/j.matdes.2018.04.029

[16] D. Schurig, J. J. Mock, B. J. Justice, S. A. Cummer, J. B. Pendry, A. F. Starr, D. R. Smith, Metamaterial electromagnetic cloak at microwave frequencies, Science 314 (5801) (2006) 977–980. doi:10.1126/science.1133628.
URL https://doi.org/10.1126/science.1133628

[17] J. J. Andrew, P. Verma, S. Kumar, Impact behavior of nanoengineered, 3d printed plate-lattices, Materials &Design 202 (2021) 109516. doi:10.1016/j.matdes.2021.109516.
URL https://doi.org/10.1016/j.matdes.2021.109516

[18] J. Ubaid, J. Schneider, V. S. Deshpande, B. L. Wardle, S. Kumar, Multifunctionality of nanoengineered self-sensing lattices enabled by additive manufacturing, Advanced Engineering Materials 24 (7) (2022) 2200194. doi:10.1002/adem.202200194.
URL https://doi.org/10.1002/adem.202200194

[19] S. AlMahri, J. Schneider, A. Schiffer, S. Kumar, Piezoresistive sensing performance of multifunctional MWCNT/HDPE auxetic structures enabled by additive manufacturing, Polymer Testing 114 (2022) 107687. doi:10.1016/j.polymertesting.2022.107687.
URL https://doi.org/10.1016/j.polymertesting.2022.107687

[20] J. Preston, Polyimides – a new class of thermally stable polymers. n. a. adrova, m. i. bessonov, l. a. laius, and a. p. rudakov, technomic publishing co., inc., stanford, calif., 1970. ix 200 pp. $26.50, Journal of Polymer Science Part B: Polymer Letters 9 (3) (1971) 230–231. doi:10.1002/pol.1971.110090315.
URL https://doi.org/10.1002/pol.1971.110090315

[21] S. Thomas, Handbook of engineering and speciality thermoplastics: Handbook of engineering and specialty thermoplastics, volume 3 polyethers and polyesters v. 3, Wiley-Scrivener, John Wiley & Sons, Chichester, England, 2011.

[22] Engineered materials handbook: Engineered materials handbook engineering plastics v. 2, ASM International, 1988.

[23] O. Kaynan, A. Yıldız, Y. E. Bozkurt, E. O. Yenigun, H. Cebeci, Electrically conductive high-performance thermoplastic filaments for fused filament fabrication, Composite Structures 237 (2020) 111930. doi:10.1016/j.compstruct.2020.111930.
URL https://doi.org/10.1016/j.compstruct.2020.111930

[24] S. Ghose, D. C. Working, J. W. Connell, J. G. Smith, K. A. Watson, D. M. Delozier, Y. P. Sun, Y. Lin, Thermal conductivity of UltemTM/carbon nanofiller blends, High Performance Polymers 18 (6) (2006) 961–977. doi:10.1177/0954008306069133.
URL https://doi.org/10.1177/0954008306069133

[25] O. Kaynan, A. Yildiz, Y. E. Bozkurt, E. O. Yenigun, H. Cebeci, Development of multifunctional CNTs reinforced PEI filaments for fused deposition modeling, in: AIAA Scitech 2019 Forum, American Institute of Aeronautics and Astronautics, 2019. doi:10.2514/6.2019-0406.
URL https://doi.org/10.2514/6.2019-0406

[26] I. V. Gofman, E. M. Ivan'kova, I. V. Abalov, V. E. Smirnova, E. N. Popova, O. Orell, J. Vuorinen, V. E. Yudin, Effect of nanoparticles of various types as

fillers on mechanical properties of block samples of a heat-resistant polyimide material: A comparative analysis, Polymer Science Series A 58 (1) (2016) 87–94. doi:10.1134/s0965545x16010028.
URL https://doi.org/10.1134/s0965545x16010028

[27] M. Liu, S. Wang, L. Jiang, Nature-inspired superwettability systems, Nature Reviews Materials 2 (7) (Jun. 2017). doi:10.1038/natrevmats.2017.36.
URL https://doi.org/10.1038/natrevmats.2017.36

[28] T. Osborn, E. Zhou, R. Gerzeski, D. Mollenhauer, G. Tandon, T. Whitney, E. Iarve, Experimental and theoretical evaluation of stiffness properties of fused deposition modeling parts, 2015, cited by: 6.

[29] E. Spišák, I. Gajdoš, J. Slota, Optimization of FDM prototypes mechanical properties with path generation strategy, Applied Mechanics and Materials 474 (2014) 273–278. doi:10.4028/www.scientific.net/amm.474.273.
URL https://doi.org/10.4028%2Fwww.scientific.net%2Famm.474.273

[30] K. C. Chuang, J. E. Grady, R. D. Draper, E.-S. E. Shin, C. Patterson, T. D. Santelle, Additive manufacturing and characterization of ultem polymers and composites, 2015, p. 448 – 463, cited by: 32.

[31] A. S. El-Gizawy, J. Cardona, B. Graybill, An integrated approach for characterization of properties and mesostructure of fused deposition modeling ultem 9085 products, 2010, cited by: 7.

[32] G. Taylor, X. Wang, K. Motaparti, S. Meng, M. Leu, K. Chandrashekhara, Modeling and characterization of fused deposition modeling tooling for autoclave process, 2015, p. 2348 – 2358, cited by: 0.

[33] S. M.-K. Bakmaev, I. S. Vorontsov, D. A. Demskiy, A. F. Makarov, Investigations into applicability of additive techniques for fabrication of aerodynamically stabilized aerostat system, Vol. 11, 2016, p. 8050 – 8055, cited by: 0.

[34] A. Bagsik, S. Josupeit, V. Schoeppner, E. Klemp, Mechanical analysis of lightweight constructions manufactured with fused deposition modeling, in: AIP Conference Proceedings, American Institute of Physics, 2014. doi:10.1063/1.4873874.
URL https://doi.org/10.1063%2F1.4873874

[35] R. K. Chen, L. Chen, B. L. Tai, Y. Wang, A. J. Shih, J. Wensman, Additive manufacturing of personalized ankle-foot orthosis, Vol. 42, 2014, p. 381 – 389, cited by: 17.

[36] Y. Zhang, Y. C. Yeoh, G. Zheng, S. K. Moon, Characterization of mechanical properties of ultem® 9085 using fdm, Vol. 2018-May, 2018, p. 451 – 457, cited by: 4.

[37] K. P. Motaparti, G. Taylor, M. C. Leu, K. Chandrashekhara, J. Castle, M. Matlack, Experimental investigation of effects of build parameters on flexural properties in fused deposition modelling parts, Virtual and Physical Prototyping 12 (3) (2017) 207–220. doi:10.1080/17452759.2017.1314117.
URL https://doi.org/10.1080%2F17452759.2017.1314117

[38] A. W. Gebisa, H. G. Lemu, Effect of process parameters on compressive properties of ULTEM 9085 produced by FDM process, in: Volume 2: Advanced Manufacturing, American Society of Mechanical Engineers, 2018. doi:10.1115/imece2018-87523.
URL https://doi.org/10.1115%2Fimece2018-87523

[39] M. Fischer, V. Schöppner, Fatigue behavior of FDM parts manufactured with ultem 9085, JOM 69 (3) (2016) 563–568. doi:10.1007/s11837-016-2197-2.
URL https://doi.org/10.1007%2Fs11837-016-2197-2

[40] N. Moazami, H. Baid, S. Dormohammadi, C. Godines, F. Abdi, G. P. Tandon, Prediction and validation of thermal mechanical properties of 3d printed ultem 1010, Vol. 2018-May, 2018, cited by: 0.

[41] I. Blanco, G. Cicala, G. Ognibene, M. Rapisarda, A. Recca, Thermal properties of polyetherimide/polycarbonate blends for advanced applications, Polymer Degradation and Stability 154 (2018) 234–238. doi:10.1016/j.polymdegradstab.2018.06.011.
URL https://doi.org/10.1016%2Fj.polymdegradstab.2018.06.011

[42] M. Fischer, V. Schöppner, Effects of a mass finishing process on parts produced from ultem 9085 by fused deposition modeling, Vol. 3, 2014, p. 2331 – 2336, cited by: 0.

[43] G. Gómez-Gras, M. A. Pérez, J. Fábregas-Moreno, G. Reyes-Pozo, Experimental study on the accuracy and surface quality of printed versus machined holes in PEI ultem 9085 FDM specimens, Rapid Prototyping Journal 27 (11) (2021) 1–12. doi:10.1108/rpj-12-2019-0306.
URL https://doi.org/10.1108%2Frpj-12-2019-0306

[44] F. Auricchio, A. Bacigalupo, L. Gambarotta, M. Lepidi, S. Morganti, F. Vadalà, A novel layered topology of auxetic materials based on the tetrachiral honeycomb microstructure, Materials & Design 179 (2019) 107883. doi:10.1016/j.matdes.2019.107883.
URL https://doi.org/10.1016/j.matdes.2019.107883

[45] M. Li, J. Jiang, B. Hu, W. Zhai, Fused deposition modeling of hierarchical porous polyetherimide assisted by an in-situ CO2 foaming technology, Composites Science and Technology 200 (2020) 108454. doi:10.1016/j.compscitech.2020.108454.
URL https://doi.org/10.1016%2Fj.compscitech.2020.108454

[46] W. Zhai, B. Hu, M. Li, J. Jiang, M. Zhou, Dimensional accuracy control and compressive property of microcellular polyetherimide honeycomb foams manufactured by an in situ foaming fused deposition modeling technology, Advanced Engineering Materials 23 (7) (2021) 2001449. doi:10.1002/adem.202001449.
URL https://doi.org/10.1002%2Fadem.202001449

[47] S. Mora, N. M. Pugno, D. Misseroni, 3d printed architected lattice structures by material jetting, Materials Today (Jun. 2022). doi:10.1016/j.mattod.2022.05.008.
URL https://doi.org/10.1016/j.mattod.2022.05.008

[48] N. K. Katiyar, G. Goel, S. Hawi, S. Goel, Nature-inspired materials: Emerging trends and prospects, NPG Asia Materials 13 (1) (Jul. 2021). doi:10.1038/s41427-021-00322-y.
URL https://doi.org/10.1038/s41427-021-00322-y

[49] M. Benedetti, A. du Plessis, R. Ritchie, M. Dallago, S. Razavi, F. Berto, Architected cellular materials: A review on their mechanical properties towards fatigue-tolerant design and fabrication, Materials Science and Engineering: R: Reports 144 (2021) 100606. doi:10.1016/j.mser.2021.100606.
URL https://doi.org/10.1016/j.mser.2021.100606

[50] A. E. Jakus, An introduction to 3d printing—past, present, and future promise, in: 3D Printing in Orthopaedic Surgery, Elsevier, 2019, pp. 1–15. doi:10.1016/b978-0-323-58118-9.00001-4.
URL https://doi.org/10.1016/b978-0-323-58118-9.00001-4

[51] G. Liu, X. Zhang, X. Chen, Y. He, L. Cheng, M. Huo, J. Yin, F. Hao, S. Chen, P. Wang, S. Yi, L. Wan, Z. Mao, Z. Chen, X. Wang, Z. Cao, J. Lu, Additive manufacturing of structural materials, Materials Science and Engineering: R: Reports (2021) 100596doi:10.1016/j.mser.2020.100596.
URL https://doi.org/10.1016/j.mser.2020.100596

[52] A. H. Schoen, Infinite periodic minimal surfaces without self-intersections, 1970.

[53] K. K. Saxena, R. Das, E. P. Calius, Three decades of auxetics research - materials with negative poisson's ratio: A review, Advanced Engineering Materials

18 (11) (2016) 1847–1870. doi:10.1002/adem.201600053.
URL https://doi.org/10.1002/adem.201600053

[54] Z. Wang, C. Luan, G. Liao, J. Liu, X. Yao, J. Fu, Progress in auxetic mechanical metamaterials: Structures, characteristics, manufacturing methods, and applications, Advanced Engineering Materials 22 (10) (2020) 2000312. doi:10.1002/adem.202000312.
URL https://doi.org/10.1002/adem.202000312

[55] W. Wu, W. Hu, G. Qian, H. Liao, X. Xu, F. Berto, Mechanical design and multifunctional applications of chiral mechanical metamaterials: A review, Materials & Design 180 (2019) 107950. doi:10.1016/j.matdes.2019.107950.
URL https://doi.org/10.1016/j.matdes.2019.107950

[56] J. Zhang, G. Lu, Z. You, Large deformation and energy absorption of additively manufactured auxetic materials and structures: A review, Composites Part B: Engineering 201 (2020) 108340. doi:10.1016/j.compositesb.2020.108340.
URL https://doi.org/10.1016/j.compositesb.2020.108340

[57] M. Lei, W. Hong, Z. Zhao, C. Hamel, M. Chen, H. Lu, H. J. Qi, 3d printing of auxetic metamaterials with digitally reprogrammable shape, ACS Applied Materials & Interfaces 11 (25) (2019) 22768–22776. doi:10.1021/acsami.9b06081.
URL https://doi.org/10.1021/acsami.9b06081

[58] S. Duan, L. Xi, W. Wen, D. Fang, A novel design method for 3d positive and negative poisson's ratio material based on tension-twist coupling effects, Composite Structures 236 (2020) 111899. doi:10.1016/j.compstruct.2020.111899.
URL https://doi.org/10.1016/j.compstruct.2020.111899

[59] H. Wang, S.-H. Xiao, C. Zhang, Novel planar auxetic metamaterial perforated with orthogonally aligned oval-shaped holes and machine learning solutions, Advanced Engineering Materials 23 (7) (2021) 2100102. doi:10.1002/adem.202100102.
URL https://doi.org/10.1002%2Fadem.202100102

[60] C. Luo, C. Z. Han, X. Y. Zhang, X. G. Zhang, X. Ren, Y. M. Xie, Design, manufacturing and applications of auxetic tubular structures: A review, Thin-Walled Structures 163 (2021) 107682. doi:10.1016/j.tws.2021.107682.
URL https://doi.org/10.1016/j.tws.2021.107682

[61] A. Forés-Garriga, G. Gómez-Gras, M. A. Pérez, Mechanical performance of additively manufactured lightweight cellular solids: Influence of cell pattern

and relative density on the printing time and compression behavior, Materials & Design 215 (2022) 110474. doi:10.1016/j.matdes.2022.110474.
URL https://doi.org/10.1016/j.matdes.2022.110474

[62] R. Zaldivar, D. Witkin, T. McLouth, D. Patel, K. Schmitt, J. Nokes, Influence of processing and orientation print effects on the mechanical and thermal behavior of 3d-printed ULTEM® 9085 material, Additive Manufacturing 13 (2017) 71–80. doi:10.1016/j.addma.2016.11.007.
URL https://doi.org/10.1016/j.addma.2016.11.007

[63] D. Bhate, J. van Soest, J. Reeher, D. Patel, D. Gibson, J. Gerbasi, M. Finfrock, A validated methodology for predicting the mechanical behavior of ultem-9085 honeycomb structures manufactured by fused deposition modeling, 2016, pp. 2095–2106, publisher Copyright: © 2016 The Department of Energy's Kansas City National Security Campus is operated and managed by Honeywell Federal Manufacturing Technologies, LLC under contract number DE-NA0002839.; 27th Annual International Solid Freeform Fabrication Symposium - An Additive Manufacturing Conference, SFF 2016 ; Conference date: 08-08-2016 Through 10-08-2016.

[64] S. Morrish, M. Pedersen, K. Wong, I. Todd, R. Goodall, Size effects in compression in electron beam melted ti6al4v diamond structure lattices, Materials Letters 190 (2017) 138–142. doi:10.1016/j.matlet.2016.12.130.
URL https://doi.org/10.1016/j.matlet.2016.12.130

[65] The mechanics of two-dimensional cellular materials, Proceedings of the Royal Society of London. A. Mathematical and Physical Sciences 382 (1782) (1982) 25–42. doi:10.1098/rspa.1982.0087.
URL https://doi.org/10.1098/rspa.1982.0087

[66] The mechanics of three-dimensional cellular materials, Proceedings of the Royal Society of London. A. Mathematical and Physical Sciences 382 (1782) (1982) 43–59. doi:10.1098/rspa.1982.0088.
URL https://doi.org/10.1098/rspa.1982.0088

[67] M. Arif, H. Alhashmi, K. Varadarajan, J. H. Koo, A. Hart, S. Kumar, Multifunctional performance of carbon nanotubes and graphene nanoplatelets reinforced PEEK composites enabled via FFF additive manufacturing, Composites Part B: Engineering 184 (2020) 107625. doi:10.1016/j.compositesb.2019.107625.
URL https://doi.org/10.1016/j.compositesb.2019.107625

[68] M. Arif, S. Kumar, K. Varadarajan, W. Cantwell, Performance of biocompatible PEEK processed by fused deposition additive manufacturing, Materials &

Design 146 (2018) 249–259. doi:10.1016/j.matdes.2018.03.015.
URL https://doi.org/10.1016/j.matdes.2018.03.015

[69] Q. Sun, G. Rizvi, C. Bellehumeur, P. Gu, Effect of processing conditions on the bonding quality of FDM polymer filaments, Rapid Prototyping Journal 14 (2) (2008) 72–80. doi:10.1108/13552540810862028.
URL https://doi.org/10.1108/13552540810862028

[70] X. Gao, S. Qi, X. Kuang, Y. Su, J. Li, D. Wang, Fused filament fabrication of polymer materials: A review of interlayer bond, Additive Manufacturing 37 (2021) 101658. doi:10.1016/j.addma.2020.101658.
URL https://doi.org/10.1016/j.addma.2020.101658

[71] Q. M. Li, I. Magkiriadis, J. J. Harrigan, Compressive strain at the onset of densification of cellular solids, Journal of Cellular Plastics 42 (5) (2006) 371–392. doi:10.1177/0021955x06063519.
URL https://doi.org/10.1177%2F0021955x06063519

[72] S. Kumar, J. Ubaid, R. Abishera, A. Schiffer, V. S. Deshpande, Tunable energy absorption characteristics of architected honeycombs enabled via additive manufacturing, ACS Applied Materials & Interfaces 11 (45) (2019) 42549–42560. doi:10.1021/acsami.9b12880.
URL https://doi.org/10.1021%2Facsami.9b12880

[73] M. Utzeri, A. Bhagavatam, E. Mancini, G. Dinda, M. Sasso, G. Newaz, Quasi-static and dynamic behavior of inconel 625 obtained by laser metal deposition: Experimental characterization and constitutive modeling, Journal of Engineering Materials and Technology 143 (4) (may 2021). doi:10.1115/1.4051087.
URL https://doi.org/10.1115%2F1.4051087

[74] M. Utzeri, M. Sasso, G. Chiappini, S. Lenci, Nonlinear vibrations of a composite beam in large displacements: Analytical, numerical, and experimental approaches, Journal of Computational and Nonlinear Dynamics 16 (2) (nov 2020). doi:10.1115/1.4048913.
URL https://doi.org/10.1115%2F1.4048913

[75] M. Rossi, G. Chiappini, M. Sasso, Characterization of aluminum alloys using a 3d full field measurement, in: Application of Imaging Techniques to Mechanics of Materials and Structures, Volume 4, Springer New York, 2012, pp. 17–23. doi:10.1007/978-1-4419-9796-8_4.
URL https://doi.org/10.1007%2F978-1-4419-9796-8_4

[76] X.-T. Wang, B. Wang, X.-W. Li, L. Ma, Mechanical properties of 3d re-entrant auxetic cellular structures, International Journal of Mechanical Sciences 131-132 (2017) 396–407. doi:10.1016/j.ijmecsci.2017.05.048.
URL https://doi.org/10.1016/j.ijmecsci.2017.05.048

[77] Z. Zhao, C. Liu, L. Sun, H. Luo, J. Wang, Y. Li, Experimental and numerical study on the constrained bending-induced collapse of hexagonal honeycomb, Composite Structures 277 (2021) 114604. doi:10.1016/j.compstruct.2021.114604.
URL https://doi.org/10.1016/j.compstruct.2021.114604

[78] W. Cantwell, J. Morton, The impact resistance of composite materials: a review, Composites 22 (5) (1991) 347–362. doi:10.1016/0010-4361(91)90549-v.
URL https://doi.org/10.1016/0010-4361(91)90549-v

[79] S. Galehdari, H. Khodarahmi, Design and analysis of a graded honeycomb shock absorber for a helicopter seat during a crash condition, International Journal of Crashworthiness 21 (3) (2016) 231–241. doi:10.1080/13588265.2016.1165440.
URL https://doi.org/10.1080/13588265.2016.1165440

[80] S. Sharafi, M. Santare, J. Gerdes, S. Advani, A multiscale modeling approach of the fused filament fabrication process to predict the mechanical response of 3d printed parts, Additive Manufacturing 51 (2022) 102597. doi:10.1016/j.addma.2022.102597.
URL https://doi.org/10.1016%2Fj.addma.2022.102597

[81] A. Sabik, M. Rucka, A. Andrzejewska, E. Wojtczak, Tensile failure study of 3d printed PLA using DIC technique and FEM analysis, Mechanics of Materials 175 (2022) 104506. doi:10.1016/j.mechmat.2022.104506.
URL https://doi.org/10.1016%2Fj.mechmat.2022.104506

[82] Y. Zhao, Y. Chen, Y. Zhou, Novel mechanical models of tensile strength and elastic property of FDM AM PLA materials: Experimental and theoretical analyses, Materials & Design 181 (2019) 108089. doi:10.1016/j.matdes.2019.108089.
URL https://doi.org/10.1016%2Fj.matdes.2019.108089

[83] H. Xin, W. Sun, J. Fish, A SURROGATE MODELING APPROACH FOR ADDITIVE-MANUFACTURED MATERIALS, International Journal for Multiscale Computational Engineering 15 (6) (2017) 525–543. doi:10.1615/intjmultcompeng.2017024632.
URL https://doi.org/10.1615%2Fintjmultcompeng.2017024632

[84] E. Polyzos, S. Ravindranath, D. V. Hemelrijck, L. Pyl, Analytical and numerical modeling of voids in additively manufactured thermoplastic parts, Additive Manufacturing 48 (2021) 102356. doi:10.1016/j.addma.2021.102356.
URL https://doi.org/10.1016%2Fj.addma.2021.102356

[85] R. M. Christensen, Failure criteria for fiber composite materials, the astonishing sixty year search, definitive usable results, Composites Science and Technology 182 (2019) 107718. doi:10.1016/j.compscitech.2019.107718.
URL https://doi.org/10.1016%2Fj.compscitech.2019.107718

[86] A. Argon, Craze initiation in glassy polymers – revisited, Polymer 52 (10) (2011) 2319–2327. doi:10.1016/j.polymer.2011.03.019.
URL https://doi.org/10.1016%2Fj.polymer.2011.03.019

[87] A. Argon, R. Cohen, Toughenability of polymers, Polymer 44 (19) (2003) 6013–6032. doi:10.1016/s0032-3861(03)00546-9.
URL https://doi.org/10.1016/s0032-3861(03)00546-9

[88] B. Gearing, L. Anand, On modeling the deformation and fracture response of glassy polymers due to shear-yielding and crazing, International Journal of Solids and Structures 41 (11-12) (2004) 3125–3150. doi:10.1016/j.ijsolstr.2004.01.017.
URL https://doi.org/10.1016%2Fj.ijsolstr.2004.01.017

[89] C. Bucknall, New criterion for craze initiation, Polymer 48 (4) (2007) 1030–1041. doi:10.1016/j.polymer.2006.12.033.
URL https://doi.org/10.1016%2Fj.polymer.2006.12.033

[90] C. Bucknall, Role of surface chain mobility in crazing, Polymer 53 (21) (2012) 4778–4786. doi:10.1016/j.polymer.2012.08.034.
URL https://doi.org/10.1016%2Fj.polymer.2012.08.034

[91] D. C. Drucker, W. Prager, Soil mechanics and plastic analysis or limit design, Quarterly of Applied Mathematics 10 (2) (1952) 157–165. doi:10.1090/qam/48291.
URL https://doi.org/10.1090%2Fqam%2F48291

[92] L. R. Alejano, A. Bobet, Drucker–prager criterion, Rock Mechanics and Rock Engineering 45 (6) (2012) 995–999. doi:10.1007/s00603-012-0278-2.
URL https://doi.org/10.1007%2Fs00603-012-0278-2

[93] R. M. Ikeda, Shear yield and crazing stresses in selected glassy polymers, Journal of Applied Polymer Science 47 (4) (1993) 619–629. doi:10.1002/app.1993.070470406.
URL https://doi.org/10.1002%2Fapp.1993.070470406

[94] K. Chen, K. S. Schweizer, Theory of yielding, strain softening, and steady plastic flow in polymer glasses under constant strain rate deformation, Macromolecules 44 (10) (2011) 3988–4000. doi:10.1021/ma200436w.
URL https://doi.org/10.1021/ma200436w

[95] D. Xu, S. L. Craig, Strain hardening and strain softening of reversibly cross-linked supramolecular polymer networks, Macromolecules 44 (18) (2011) 7478–7488. doi:10.1021/ma201386t.
URL https://doi.org/10.1021/ma201386t

[96] W. Tang, D. Li, Y. Peng, P. Wu, Shear band development under simple shear and the intrinsicality of strain softening of amorphous glassy polymers, Polymer 255 (2022) 125115. doi:10.1016/j.polymer.2022.125115.
URL https://doi.org/10.1016/j.polymer.2022.125115

[97] L. Cheng, T. Guo, Void interaction and coalescence in polymeric materials, International Journal of Solids and Structures 44 (6) (2007) 1787–1808. doi:10.1016/j.ijsolstr.2006.08.007.
URL https://doi.org/10.1016/j.ijsolstr.2006.08.007

[98] E. Farotti, E. Mancini, A. Lattanzi, M. Utzeri, M. Sasso, Effect of temperature and strain rate on the formation of shear bands in polymers under quasi-static and dynamic compressive loadings: Proposed constitutive model and numerical validation, Polymer 245 (2022) 124690. doi:10.1016/j.polymer.2022.124690.
URL https://doi.org/10.1016/j.polymer.2022.124690

[99] N. Bonora, D. Gentile, A. Pirondi, G. Newaz, Ductile damage evolution under triaxial state of stress: theory and experiments, International Journal of Plasticity 21 (5) (2005) 981–1007. doi:10.1016/j.ijplas.2004.06.003.
URL https://doi.org/10.1016/j.ijplas.2004.06.003

[100] N. Bonora, G. Testa, A. Ruggiero, G. Iannitti, D. Gentile, Continuum damage mechanics modelling incorporating stress triaxiality effect on ductile damage initiation, Fatigue & Fracture of Engineering Materials & Structures 43 (8) (2020) 1755–1768. doi:10.1111/ffe.13220.
URL https://doi.org/10.1111/ffe.13220

[101] A. Mesbah, M. Elmeguenni, Z. Yan, F. Zaïri, N. Ding, J.-M. Gloaguen, How stress triaxiality affects cavitation damage in high-density polyethylene: Experiments and constitutive modeling, Polymer Testing 100 (2021) 107248. doi:10.1016/j.polymertesting.2021.107248.
URL https://doi.org/10.1016/j.polymertesting.2021.107248

[102] S. G. Rad, A. Zajkani, On the stress state-based coupled plasticity – ductile damage model for aluminum alloys considering the influence of high-rate impulsive preload, International Journal of Impact Engineering 146 (2020) 103715. doi:10.1016/j.ijimpeng.2020.103715.
URL https://doi.org/10.1016/j.ijimpeng.2020.103715

[103] Y. Li, X. Sun, S. Zhang, S. Han, A fractal crazing constitutive model of glassy polymers considering damage and toughening, Engineering Fracture Mechanics 267 (2022) 108354. doi:10.1016/j.engfracmech.2022.108354.
URL https://doi.org/10.1016/j.engfracmech.2022.108354

[104] D. Leguillon, É. Martin, M.-C. Lafarie-Frenot, Flexural vs. tensile strength in brittle materials, Comptes Rendus Mécanique 343 (4) (2015) 275–281. doi:10.1016/j.crme.2015.02.003.
URL https://doi.org/10.1016/j.crme.2015.02.003

[105] A. E. Magri, S. Vanaei, S. Vaudreuil, An overview on the influence of process parameters through the characteristic of 3d-printed PEEK and PEI parts, High Performance Polymers 33 (8) (2021) 862–880. doi:10.1177/09540083211009961.
URL https://doi.org/10.1177/09540083211009961

[106] S. Clark, T. Yap, M. Tehrani, Validation of a finite element model for fused filament fabrication additive manufacturing, in: Volume 2A: Advanced Manufacturing, American Society of Mechanical Engineers, 2021. doi:10.1115/imece2021-73803.
URL https://doi.org/10.1115/imece2021-73803

[107] P. WANG, B. ZOU, S. DING, L. LI, C. HUANG, Effects of FDM-3d printing parameters on mechanical properties and microstructure of CF/PEEK and GF/PEEK, Chinese Journal of Aeronautics 34 (9) (2021) 236–246. doi:10.1016/j.cja.2020.05.040.
URL https://doi.org/10.1016/j.cja.2020.05.040

[108] P. Wu, E. van der Giessen, Analysis of shear band propagation in amorphous glassy polymers, International Journal of Solids and Structures 31 (11) (1994) 1493–1517. doi:10.1016/0020-7683(94)90011-6.
URL https://doi.org/10.1016/0020-7683(94)90011-6

[109] R. Zhang, P. Bai, D. Lei, R. Xiao, Aging-dependent strain localization in amorphous glassy polymers: From necking to shear banding, International Journal of Solids and Structures 146 (2018) 203–213. doi:10.1016/j.ijsolstr.2018.03.030.
URL https://doi.org/10.1016/j.ijsolstr.2018.03.030

[110] P. W. Bridgman, Studies in Large Plastic Flow and Fracture, Harvard University Press, 1964. doi:10.4159/harvard.9780674731349.
URL https://doi.org/10.4159/harvard.9780674731349

[111] S. Tu, X. Ren, J. He, Z. Zhang, Stress–strain curves of metallic materials and post-necking strain hardening characterization: A review, Fatigue & Fracture

of Engineering Materials & Structures 43 (1) (2019) 3–19. doi:10.1111/ffe.13134.
URL https://doi.org/10.1111/ffe.13134

[112] D. Turner, Tensile strength elevation of brittle polymers by entanglements, Polymer 23 (4) (1982) 626–629. doi:10.1016/0032-3861(82)90106-9.
URL https://doi.org/10.1016/0032-3861(82)90106-9

[113] E. J. Kramer, Craze fibril formation and breakdown, Polymer Engineering and Science 24 (10) (1984) 761–769. doi:10.1002/pen.760241006.
URL https://doi.org/10.1002/pen.760241006

[114] A. M. Donald, E. J. Kramer, R. A. Bubeck, The entanglement network and craze micromechanics in glassy polymers, Journal of Polymer Science: Polymer Physics Edition 20 (7) (1982) 1129–1141. doi:10.1002/pol.1982.180200703.
URL https://doi.org/10.1002/pol.1982.180200703

[115] G. Curtzwiler, M. Early, D. Gottschalk, C. Konecki, R. Peterson, S. Wand, J. Rawlins, The world surface coatings is centerd around the glass transition tempratuer, but which one? part i, Jct Coatings Tech 11 (2014) 28.

[116] M. R. Khosravani, F. Berto, M. R. Ayatollahi, T. Reinicke, Characterization of 3d-printed PLA parts with different raster orientations and printing speeds, Scientific Reports 12 (1) (Jan. 2022). doi:10.1038/s41598-022-05005-4.
URL https://doi.org/10.1038/s41598-022-05005-4

[117] T. Yao, J. Ye, Z. Deng, K. Zhang, Y. Ma, H. Ouyang, Tensile failure strength and separation angle of FDM 3d printing PLA material: Experimental and theoretical analyses, Composites Part B: Engineering 188 (2020) 107894. doi:10.1016/j.compositesb.2020.107894.
URL https://doi.org/10.1016/j.compositesb.2020.107894

[118] O. Pierron, D. Koss, A. Motta, Tensile specimen geometry and the constitutive behavior of zircaloy-4, Journal of Nuclear Materials 312 (2-3) (2003) 257–261. doi:10.1016/s0022-3115(02)01554-4.
URL https://doi.org/10.1016/s0022-3115(02)01554-4

[119] M. Utzeri, E. Farotti, M. Coccia, E. Mancini, M. Sasso, High strain rate compression behaviour of 3d printed carbon-PA, Journal of Materials Research 36 (10) (2021) 2083–2093. doi:10.1557/s43578-021-00248-9.
URL https://doi.org/10.1557/s43578-021-00248-9

[120] J. Aboudi, S. M. Arnold, B. A. Bednarcyk, Micromechanics of composite materials: a generalized multiscale analysis approach, Butterworth-Heinemann, 2012.

[121] S. Bargmann, B. Klusemann, J. Markmann, J. E. Schnabel, K. Schneider, C. Soyarslan, J. Wilmers, Generation of 3d representative volume elements for heterogeneous materials: A review, Progress in Materials Science 96 (2018) 322–384. doi:10.1016/j.pmatsci.2018.02.003.
URL https://doi.org/10.1016/j.pmatsci.2018.02.003

[122] Y. Sun, Q. Li, Dynamic compressive behaviour of cellular materials: A review of phenomenon, mechanism and modelling, International Journal of Impact Engineering 112 (2018) 74–115. doi:10.1016/j.ijimpeng.2017.10.006.
URL https://doi.org/10.1016/j.ijimpeng.2017.10.006

[123] S. Pal, S. Maiti, G. Subhash, Effect of microscopic deformation mechanisms on the dynamic response of soft cellular materials, Mechanics of Materials 42 (2) (2010) 118–133. doi:10.1016/j.mechmat.2009.11.014.
URL https://doi.org/10.1016/j.mechmat.2009.11.014

[124] W. Ronan, V. S. Deshpande, N. A. Fleck, The tensile ductility of cellular solids: The role of imperfections, International Journal of Solids and Structures 102-103 (2016) 200–213. doi:10.1016/j.ijsolstr.2016.10.004.
URL https://doi.org/10.1016/j.ijsolstr.2016.10.004

[125] C. McIlroy, P. D. Olmsted, Deformation of an amorphous polymer during the fused-filament-fabrication method for additive manufacturing, Journal of Rheology 61 (2) (2017) 379–397. doi:10.1122/1.4976839.
URL https://doi.org/10.1122/1.4976839

[126] C. McIlroy, P. Olmsted, Disentanglement effects on welding behaviour of polymer melts during the fused-filament-fabrication method for additive manufacturing, Polymer 123 (2017) 376–391. doi:10.1016/j.polymer.2017.06.051.
URL https://doi.org/10.1016/j.polymer.2017.06.051

[127] M. Matveev, A. Long, Numerical modelling for predicting failure in textile composites, in: Numerical Modelling of Failure in Advanced Composite Materials, Elsevier, 2015, pp. 435–455. doi:10.1016/b978-0-08-100332-9.00016-5.
URL https://doi.org/10.1016/b978-0-08-100332-9.00016-5

[128] S. Hong, D. Liu, On the relationship between impact energy and delamination area, Experimental Mechanics 29 (2) (1989) 115–120. doi:10.1007/bf02321362.
URL https://doi.org/10.1007/bf02321362

[129] J. Cugnoni, R. Amacher, S. Kohler, J. Brunner, E. Kramer, C. Dransfeld, W. Smith, K. Scobbie, L. Sorensen, J. Botsis, Towards aerospace grade thin-ply composites: Effect of ply thickness, fibre, matrix and interlayer toughening

on strength and damage tolerance, Composites Science and Technology 168 (2018) 467–477. doi:10.1016/j.compscitech.2018.08.037.
URL https://doi.org/10.1016/j.compscitech.2018.08.037

[130] H.-T. Chen, A. J. Taylor, N. Yu, A review of metasurfaces: physics and applications, Reports on Progress in Physics 79 (7) (2016) 076401. doi:10.1088/0034-4885/79/7/076401.
URL https://doi.org/10.1088/0034-4885/79/7/076401

[131] M. Kadic, G. W. Milton, M. van Hecke, M. Wegener, 3d metamaterials, Nature Reviews Physics 1 (3) (2019) 198–210. doi:10.1038/s42254-018-0018-y.
URL https://doi.org/10.1038/s42254-018-0018-y

[132] D. Harutyunyan, G. W. Milton, R. V. Craster, High-frequency homogenization for travelling waves in periodic media, Proceedings of the Royal Society A: Mathematical, Physical and Engineering Sciences 472 (2191) (2016) 20160066. doi:10.1098/rspa.2016.0066.
URL https://doi.org/10.1098/rspa.2016.0066

[133] V. G. Veselago, Electrodynamics of media with simultaneously negative electric permittivity and magnetic permeability, in: Advances in Electromagnetics of Complex Media and Metamaterials, Springer Netherlands, 2002, pp. 83–97. doi:10.1007/978-94-007-1067-2_5.
URL https://doi.org/10.1007/978-94-007-1067-2_5

[134] T. Koschny, M. Kafesaki, E. N. Economou, C. M. Soukoulis, Effective medium theory of left-handed materials, Physical Review Letters 93 (10) (Sep. 2004). doi:10.1103/physrevlett.93.107402.
URL https://doi.org/10.1103/physrevlett.93.107402

[135] M. Kadic, T. Bückmann, R. Schittny, M. Wegener, Metamaterials beyond electromagnetism, Reports on Progress in Physics 76 (12) (2013) 126501. doi:10.1088/0034-4885/76/12/126501.
URL https://doi.org/10.1088/0034-4885/76/12/126501

[136] J. Qu, M. Kadic, M. Wegener, Poroelastic metamaterials with negative effective static compressibility, Applied Physics Letters 110 (17) (2017) 171901. doi:10.1063/1.4981783.
URL https://doi.org/10.1063/1.4981783

[137] S. Hassanpour, G. R. Heppler, Theory of micropolar gyroelastic continua, Acta Mechanica 227 (5) (2016) 1469–1491. doi:10.1007/s00707-016-1573-x.
URL https://doi.org/10.1007/s00707-016-1573-x

[138] A. Panteghini, R. Lagioia, A micropolar isotropic plasticity formulation for non-associated flow rule and softening featuring multiple classical yield criteria,

International Journal for Numerical and Analytical Methods in Geomechanics 46 (4) (2021) 674–696. doi:10.1002/nag.3316.
URL https://doi.org/10.1002/nag.3316

[139] B. Lemkalli, M. Kadic, Y. E. Badri, S. Guenneau, A. Bouzid, Y. Achaoui, Mapping of elastic properties of twisting metamaterials onto micropolar continuum using static calculations (2022). doi:10.48550/ARXIV.2209.15126.
URL https://arxiv.org/abs/2209.15126

[140] L. Dolin, On the possibility of comparison of three-dimensional electromagnetic systems with nonuniform anisotropic filling, Izv. Vyssh. Uchebn. Zaved. Radiofiz. 4 (1961) 964–967.

[141] P. Alitalo, S. Tretyakov, Electromagnetic cloaking with metamaterials, Materials Today 12 (3) (2009) 22–29. doi:10.1016/s1369-7021(09)70072-0.
URL https://doi.org/10.1016/s1369-7021(09)70072-0

[142] G. W. Milton, M. Briane, J. R. Willis, On cloaking for elasticity and physical equations with a transformation invariant form, New Journal of Physics 8 (10) (2006) 248–248. doi:10.1088/1367-2630/8/10/248.
URL https://doi.org/10.1088/1367-2630/8/10/248

[143] D. E. Quadrelli, R. Craster, M. Kadic, F. Braghin, Elastic wave near-cloaking, Extreme Mechanics Letters 44 (2021) 101262. doi:10.1016/j.eml.2021.101262.
URL https://doi.org/10.1016/j.eml.2021.101262

[144] D. Shin, Y. Urzhumov, Y. Jung, G. Kang, S. Baek, M. Choi, H. Park, K. Kim, D. R. Smith, Broadband electromagnetic cloaking with smart metamaterials, Nature Communications 3 (1) (Jan. 2012). doi:10.1038/ncomms2219.
URL https://doi.org/10.1038/ncomms2219

[145] C. Kern, M. Kadic, M. Wegener, Experimental evidence for sign reversal of the hall coefficient in three-dimensional metamaterials, Physical Review Letters 118 (1) (Jan. 2017). doi:10.1103/physrevlett.118.016601.
URL https://doi.org/10.1103/physrevlett.118.016601

[146] D. D. L. Chung, A critical review of piezoresistivity and its application in electrical-resistance-based strain sensing, Journal of Materials Science 55 (32) (2020) 15367–15396. doi:10.1007/s10853-020-05099-z.
URL https://doi.org/10.1007/s10853-020-05099-z

[147] C. fu Yang, L. jiang Qin, Graphical representation and explanation of the conductivity tensor of anisotropic media, Surveys in Geophysics 41 (2) (2020) 249–281. doi:10.1007/s10712-019-09581-5.
URL https://doi.org/10.1007/s10712-019-09581-5

[148] G. Chen, Y. Lin, Stress–strain–electrical resistance effects and associated state equations for uniaxial rock compression, International Journal of Rock Mechanics and Mining Sciences 41 (2) (2004) 223–236. doi:10.1016/s1365-1609(03)00092-3.
URL https://doi.org/10.1016/s1365-1609(03)00092-3

[149] I. A. Ventura, J. Zhou, G. Lubineau, Drastic modification of the piezoresistive behavior of polymer nanocomposites by using conductive polymer coatings, Composites Science and Technology 117 (2015) 342–350. doi:10.1016/j.compscitech.2015.07.007.
URL https://doi.org/10.1016/j.compscitech.2015.07.007

[150] X. Xi, D. Chung, Piezoresistivity and piezoelectricity discovered in aluminum, with relevance to structural self-sensing, Sensors and Actuators A: Physical 289 (2019) 144–156. doi:10.1016/j.sna.2019.02.013.
URL https://doi.org/10.1016/j.sna.2019.02.013

[151] M. J. Katz, Electrical conductivity in heavily doped n-type germanium: Temperature and stress dependence, Physical Review 140 (4A) (1965) A1323.

[152] R. Hill, The essential structure of constitutive laws for metal composites and polycrystals, Journal of the Mechanics and Physics of Solids 15 (2) (1967) 79–95. doi:10.1016/0022-5096(67)90018-x.
URL https://doi.org/10.1016/0022-5096(67)90018-x

[153] A. Mirabolghasemi, A. Akbarzadeh, D. Rodrigue, D. Therriault, Thermal conductivity of architected cellular metamaterials, Acta Materialia 174 (2019) 61–80. doi:10.1016/j.actamat.2019.04.061.
URL https://doi.org/10.1016/j.actamat.2019.04.061

[154] P. Jiang, X. Qian, X. Li, R. Yang, Three-dimensional anisotropic thermal conductivity tensor of single crystalline $\beta - ga_2o_3$, Applied Physics Letters 113 (23) (2018) 232105. doi:10.1063/1.5054573.
URL https://doi.org/10.1063/1.5054573

[155] I. Belova, C. Veyhl, T. Fiedler, G. Murch, Analysis of anisotropic behaviour of thermal conductivity in cellular metals, Scripta Materialia 65 (5) (2011) 436–439. doi:10.1016/j.scriptamat.2011.05.029.
URL https://doi.org/10.1016/j.scriptamat.2011.05.029

[156] J. Nordmann, M. Aßmus, H. Altenbach, Visualising elastic anisotropy: theoretical background and computational implementation, Continuum Mechanics and Thermodynamics 30 (4) (2018) 689–708. doi:10.1007/s00161-018-0635-9.
URL https://doi.org/10.1007/s00161-018-0635-9

[157] J.-M. Zhang, Y. Zhang, K.-W. Xu, V. Ji, Young's modulus surface and poisson's ratio curve for cubic metals, Journal of Physics and Chemistry of Solids 68 (4) (2007) 503–510. doi:10.1016/j.jpcs.2007.01.025.
URL https://doi.org/10.1016/j.jpcs.2007.01.025

[158] N. F. Hany, E. G. Hantouche, M. H. Harajli, Finite element modeling of FRP-confined concrete using modified concrete damaged plasticity, Engineering Structures 125 (2016) 1–14. doi:10.1016/j.engstruct.2016.06.047.
URL https://doi.org/10.1016/j.engstruct.2016.06.047

[159] H. Cheng, C. M. Paz, B. C. Pinheiro, S. F. Estefen, Experimentally based parameters applied to concrete damage plasticity model for strain hardening cementitious composite in sandwich pipes, Materials and Structures 53 (4) (Jul. 2020). doi:10.1617/s11527-020-01513-9.
URL https://doi.org/10.1617/s11527-020-01513-9

[160] C. Farahmandpour, S. Dartois, M. Quiertant, Y. Berthaud, H. Dumontet, A concrete damage–plasticity model for FRP confined columns, Materials and Structures 50 (2) (Mar. 2017). doi:10.1617/s11527-017-1016-8.
URL https://doi.org/10.1617/s11527-017-1016-8

[161] T. Ozbakkaloglu, A. Gholampour, J. C. Lim, Damage-plasticity model for FRP-confined normal-strength and high-strength concrete, Journal of Composites for Construction 20 (6) (Dec. 2016). doi:10.1061/(asce)cc.1943-5614.0000712.
URL https://doi.org/10.1061/(asce)cc.1943-5614.0000712

[162] P. Grassl, M. Jirásek, Damage-plastic model for concrete failure, International Journal of Solids and Structures 43 (22-23) (2006) 7166–7196. doi:10.1016/j.ijsolstr.2006.06.032.
URL https://doi.org/10.1016/j.ijsolstr.2006.06.032